



University of
Massachusetts
Amherst

Improved Load Rating Procedures for Deteriorated Steel Beam Ends with Deteriorated Stiffeners

Item Type	Technical Report
Authors	Tzortzinis, Georgios;Breña, Sergio F.;Gerasimidis, Simos
Download date	2026-06-11 19:38:47
Link to Item	https://hdl.handle.net/20.500.14394/55003



September 2021

Report No. 21-024

Charles D. Baker
Governor

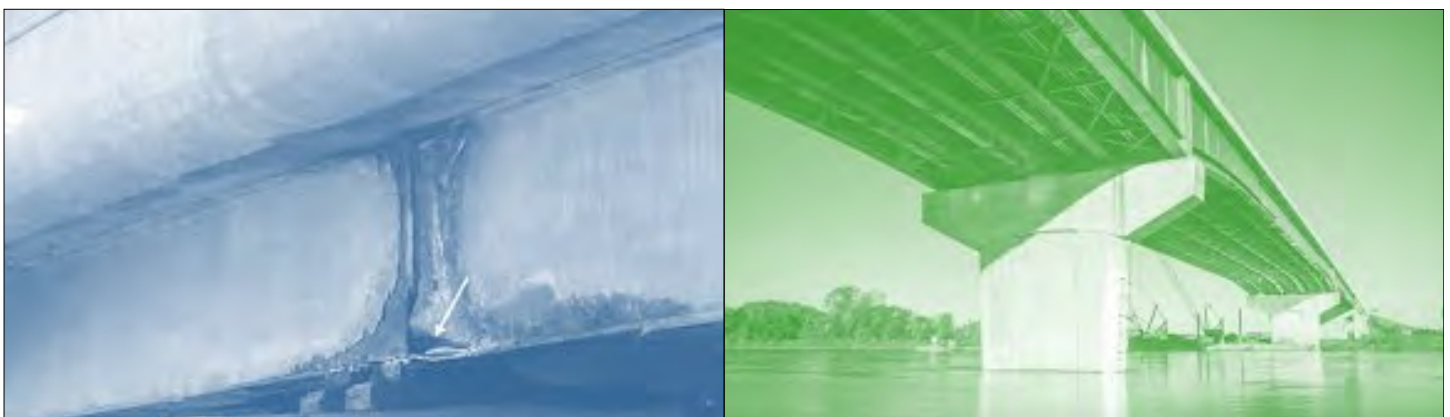
Karyn E. Polito
Lieutenant Governor

Jamey Tesler
MassDOT Secretary & CEO

Improved Load Rating Procedures for Deteriorated Steel Beam Ends with Deteriorated Stiffeners

Principal Investigator (s)
Georgios Tzortzinis, Graduate Researcher
Dr. Sergio F. Breña
Dr. Simos Gerasimidis

University of Massachusetts Amherst



Research and Technology Transfer Section
MassDOT Office of Transportation Planning



U.S. Department of Transportation
Federal Highway Administration

Technical Report Document Page

1. Report No. 21-024	2. Government Accession No. n/a	3. Recipient's Catalog No. n/a	
4. Title and Subtitle Improved Load Rating Procedures for Deteriorated Steel Beam Ends with Deteriorated Stiffeners		5. Report Date September 2021	
		6. Performing Organization Code n/a	
7. Author(s) Georgios Tzortzinis, Simos Gerasimidis, Sergio F. Breña,		8. Performing Organization Report No. 21-024	
9. Performing Organization Name and Address University of Massachusetts Amherst UMass Transportation Center 130 Natural Resources Way Amherst, MA 01003		10. Work Unit No. (TRAIS) n/a	
		11. Contract or Grant No.	
12. Sponsoring Agency Name and Address Massachusetts Department of Transportation Office of Transportation Planning Ten Park Plaza, Suite 4150, Boston, MA 02116		13. Type of Report and Period Covered Final Report September 2021 [May 2019 - September 2021]	
		14. Sponsoring Agency Code n/a	
15. Supplementary Notes Project Champion – Matthew Weidele, MassDOT			
16. Abstract This study aims to provide evaluation policies for the bearing capacity assessment of plate girders with corroded ends. The developed methodology was organized in three phases that each employed real corrosion data. First, inspection reports of bridges with corrosion-induced damage were processed to quantify the shape and bounds of the most common corrosion patterns. Second, full-scale laboratory tests were performed on two specimens built on naturally corroded girders obtained from decommissioned bridges in the Commonwealth of Massachusetts. Third, experimentally acquired data were employed to validate a composite girder level finite element model able to capture the failure load and mode of plate girders with corroded ends. Subsequently, by combining the previously defined corrosion patterns with computational modelling, an extensive parametric analysis was conducted to define the parameters that have influencing impact on the residual bearing capacity. Finally, analytical prediction tools were developed based on a data set of approximately 1,000 scenarios.			
17. Key Word Corroded ends, bridges, load rating procedures, deteriorated steel beam ends, deteriorated stiffeners		18. Distribution Statement unrestricted	
19. Security Classif. (of this report) unclassified	20. Security Classif. (of this page) unclassified	21. No. of Pages 149	22. Price n/a

Form DOT F 1700.7 (8-72)

Reproduction of completed page authorized

This page left blank intentionally.

**Improved Load Rating Procedures for Deteriorated Steel Beam Ends
with Deteriorated Stiffeners**

Final Report

Prepared by:

Georgios Tzortzinis
Graduate Researcher

Simos Gerasimidis, Ph.D.
Principal Investigator

Sergio Breña, Ph.D.
Co-Principal Investigator

University of Massachusetts Amherst
130 Natural Resources Way, Amherst, MA 01003

Prepared For:

Massachusetts Department of Transportation
Office of Transportation Planning, Ten Park Plaza, Suite 4150
Boston, MA 02116

June 2021

This page left blank intentionally.

Disclaimer

The contents of this report reflect the views of the authors, who are responsible for the facts and the accuracy of the data presented herein. The contents do not necessarily reflect the official view or policies of the Massachusetts Department of Transportation or the Federal Highway Administration. This report does not constitute a standard, specification, or regulation.

This page left blank intentionally.

Executive Summary

This study of Improved Load Rating Procedures for Deteriorated Steel Beam Ends with Deteriorated Stiffeners was undertaken as part of the Massachusetts Department of Transportation (MassDOT) Research Program. This program is funded with Federal Highway Administration (FHWA) State Planning and Research (SPR) funds. Through this program, applied research is conducted on topics of importance to the Commonwealth of Massachusetts transportation agencies.

The national highway system consists of approximately 46,000 (1) structurally deficient bridges, with corrosion as a common cause for steel viaduct deterioration. This condition can be primarily attributed to malfunctioning deck expansion joints, which fail to prevent water or deicing mixtures from penetrating into the bearing area. The buildup of this runoff triggers a corrosive process that significantly varies in topology and intensity, leading in many cases to severe section loss that affects the residual bearing capacity of the beam and, consequently, of the whole bridge. This research focuses on simple span girders with plate girders and uses real corrosion data to assess the current bridge manual procedures.

The research work had three phases:

- I. Gathering data and assessing the current condition of steel bridges (Sections 2 and 5 of this report).
- II. Experimental testing of naturally corroded beam ends (Sections 3 and 6 of this report).
- III. Computational parametric analysis and new proposed procedures for the bridge manual (Sections 4, 7, and 8 of this report).

The organization of this report is as follows:

- Sections 2 to 4 describe the methodology of this study.
- Sections 5 to 8 present the results.
- Section 8 includes the implementation of the research findings and the proposed new procedures to better predict the capacity of corroded girders.

Section 2 presents the study on the current deterioration condition of steel bridges with plate girders through MassDOT inspection reports of viaducts that have experienced beam end corrosion. Real corrosion data on thickness loss, corroded area size, and location are collected from the reports. Using this data, Section 5 includes the post-processing of 210 corroded beam ends described in the available inspection reports. The outcome of this analysis is the identification of the most common corrosion topologies.

Over the years, a significant amount of research has been carried out to determine the remaining capacity of corroded plate girders. Researchers have followed both experimental and computational approaches. However, to date, no study that the research team is aware of has looked at beams with natural corrosion. In addition, most of these studies intentionally

focused on the panel shear failure by accounting for strong bearing stiffeners. However, this assumption contradicts data illustrated in inspection reports and inspectors' observation findings from the Commonwealth of Massachusetts, which indicate that usually stiffeners undergo severe section loss. To address these limitations, the researchers performed full-scale laboratory tests on specimens built on actual girders obtained from decommissioned bridges. In Section 3 of this report, the beam selection process, the design of the testing rig, the instrumentation configuration, and the detailed descriptions of each specimen are presented. Following the tests, all the measured data and the failure modes are included in Section 6.

Based on the experimental results derived by the authors and the literature, a high-fidelity numerical finite element model was developed and calibrated, capable of predicting the capacity of composite plate girders with corroded ends. The simulation methodology and the details about the computational modeling are explained in Section 4. Combining the corrosion patterns identified in the first phase of the project with numerical modeling, an extensive parametric analysis was performed under the assumption of uniform section loss along the corroded area. In Section 7, the bounds of the corrosion topology that significantly affect the residual strength of deteriorated girders are identified.

Finally, in Section 8, the current analytical expressions that were evaluated and modified for three different general corrosion patterns are presented. The new proposed equations are included in this section.

Table of Contents

Technical Report Document Page.....	i
Disclaimer	v
Executive Summary	vii
Table of Contents	ix
List of Tables.....	xi
List of Figures	xiii
List of Acronyms.....	xvii
1.0 Introduction	1
1.1 Background Information.....	1
1.2 Literature Review.....	2
1.3 Research Goals.....	3
2.0 Methodology for Categorization of Corrosion Topologies	5
2.1 Data Collection	5
2.1.1 Format of Data.....	5
2.1.2 Amount of Data	5
2.2 Definition and Quantification of the Phenomenon	7
2.2.1 Beam End Configuration	7
2.2.2 General Categorization of Corrosion and Hole Patterns.....	9
2.2.3 Summary Spreadsheet Implementation	21
3.0 Experimental Work Methodology	25
3.1 Experimental Preparation.....	25
3.1.1 Beam Selection and Shipment to UMass Testing Facilities	25
3.1.2 Specimens Fabrication.....	27
3.1.3 Design of Experimental Configuration.....	28
3.1.4 Instrumentation Configuration.....	28
3.2 Specimens Geometry	29
3.2.1 Specimen A.....	29
3.2.2 Specimen B.....	32
4.0 Analytical Work Methodology.....	37
4.1 Computational Model Validation.....	37
4.1.1 Mechanical Model	37
4.1.2 Finite Element Procedures	40
4.2 Composite Action	41
4.3 Parametric Analysis Setup	42
4.3.1 Corrosion Scenarios.....	42
4.3.2 Beam Geometries.....	44
4.3.3 Material Properties.....	45
4.3.4 Boundary Conditions	45
4.3.5 Loading Conditions.....	46
4.3.6 Geometric Imperfection	47
4.3.7 Programming Implementation	48
4.3.8 Definition of Failure	48
5.0 Post-Processing of Corrosion Data.....	51
5.1 General Metrics for C1 Configuration	51

5.2 General Metrics for C2 Configuration	52
5.3 General Metrics for Beam Geometry	54
5.4 Final Corrosion Patterns.....	54
6.0 Experimental Results.....	61
6.1 Specimen A.....	61
6.2 Specimen B.....	64
7.0 Analytical Results.....	71
7.1 Computational Model Validation.....	71
7.2 Composite Action Validation.....	73
7.3 Geometric Imperfection Amplitude.....	73
7.4 Stiffener Corrosion Topology Effect	75
7.4.1 Stiffener Section Loss.....	75
7.4.2 Stiffener Corrosion Height Effect.....	75
7.5 Web Corrosion Topology Effect.....	76
7.5.1 Section Loss Effect.....	76
7.5.2 Web Corrosion Length Effect.....	77
7.5.3 Web Corrosion Height Effect	77
7.6 Failure Modes	78
8.0 Implementation and Technology Transfer	79
8.1 Evaluation of Current Procedures	79
8.1.1 Description of Current MassDOT Procedures.....	79
8.1.2 Comparison between Experimental and Current Predicted Capacities.....	80
8.1.3 Comparison between Numerically Obtained and Current Predicted Capacities	82
8.2 Proposed Procedures	84
8.2.1 Equation Formulation	84
8.2.2 Corrosion Input	85
8.2.3 Equation Fitting	86
8.3. Evaluation of Proposed Procedures	87
8.3.1 Comparison between Experimental and New Predicted Capacities	87
8.3.2 Analytical Provisions and 3D Scanning.	88
8.3.3 Comparison between Numerically Obtained and New Predicted Capacities	89
9.0 Conclusions	91
9.1. Phase I: Most Common Corrosion Topologies—Data Collection.....	91
9.2. Phase II: Experimental Testing	92
9.3. Phase III: Computational Results—Parametric Analysis.....	93
9.4. New Procedures: Final Outcome	94
10.0 Limitations and Future Work	95
11.0 References	97
12.0 Appendix	99
12.1 Appendix A: Detailed Data and Processing Graphs for Beam Ends with One Bearing Stiffener.	99
12.2 Appendix B: Detailed Data and Processing Graphs for Beam Ends with Two Bearing Stiffeners	116

List of Tables

Table 2.1: Classification of available inspection reports based on general properties	6
Table 2.2: Web corrosion pattern W1 for C1 configuration.....	9
Table 2.3: Web corrosion pattern W2 for C1 configuration.....	10
Table 2.4: Web corrosion pattern W3 for C1 configuration.....	10
Table 2.5: Web corrosion pattern W4 for C1 configuration.....	11
Table 2.6: Web corrosion W5 for C1 configuration.....	11
Table 2.7: Web hole pattern H1a for C1 configuration.....	12
Table 2.8: Web hole pattern H1b for C1 configuration.....	12
Table 2.9: Web hole pattern H2 for C1 configuration.....	13
Table 2.10: Web hole pattern H3 for C1 configuration.....	13
Table 2.11: Web hole pattern H4 for C1 configuration.....	14
Table 2.12: Web corrosion pattern W1 for C2 configuration.....	15
Table 2.13: Web corrosion pattern W2 for C2 configuration.....	15
Table 2.14: Web corrosion pattern W3 for C2 configuration.....	16
Table 2.15: Web corrosion pattern W4 for C2 configuration.....	16
Table 2.16: Web corrosion pattern W5 for C2 configuration.....	17
Table 2.17: Web hole pattern H1 for C2 configuration.....	17
Table 2.18: Web hole pattern H2 for C2 configuration.....	18
Table 2.19: Web hole pattern H3 for C2 configuration.....	18
Table 2.20: Web hole pattern H4 for C2 configuration.....	19
Table 2.21: Web hole pattern H5 for C2 configuration.....	19
Table 2.22: Stiffener corrosion pattern.....	20
Table 2.23: Stiffener hole pattern HB for C1 and C2 configurations.....	20
Table 2.24: Stiffener hole pattern HT for C1 and C2 configurations.....	21
Table 4.1: Metrics of examined scenarios.....	44
Table 5.1: General metrics for web corrosion of beams with unique bearing stiffener (C1 configuration)	51
Table 5.2: General metrics for web corrosion of beams with two bearing stiffeners (C2 configuration)	53
Table 5.3: General metrics for stiffener corrosion of beams in compliance with C2 configuration	53
Table 5.4: Analysis of final corrosion topologies for cases with unique bearing stiffener per web face	55
Table 5.5: Analysis of final corrosion topologies for cases with two bearing stiffeners per web face	57
Table 5.6: Analysis of final corrosion topologies for stiffeners	59
Table 8.1: Parameters used for capacity calculation of Specimen A	81
Table 8.2: Comparison between experimental and predicted capacity for Specimen A	81
Table 8.3: Parameters used for capacity estimation of Specimen B.....	82
Table 8.4: Comparison between experimental and predicted capacity for Specimen B	82
Table 8.5: Analytical description of examined corrosion patterns	84
Table 8.6: Design specifications of three employed geometries	84
Table 8.7: Parameters emerging nonlinear regression for Eq. 8.6.....	86
Table 8.8: Comparison between experimental and analytical prediction predictions for Specimen A	88
Table 8.9: Comparison between experimental and analytical prediction predictions for Specimen B	88
Table 12.1: Dimension of most common deterioration scenarios for W1 web corrosion pattern and associated holes	101
Table 12.2: Dimension of most common deterioration scenarios for W2 web corrosion pattern and associated holes	103

Table 12.3: Dimension of most common deterioration scenarios for W3 web corrosion pattern and associated holes	105
Table 12.4: Dimension of most common deterioration scenarios for W4 web corrosion pattern and associated holes	108
Table 12.5: Dimension of the most common deterioration scenarios for W5 web corrosion pattern and the associated holes.....	112
Table 12.6: Dimension of the most common deterioration scenarios for stiffener corrosion and holes for beam ends with C1 configuration.	114
Table 12.7: Dimension of most common deterioration scenarios for W1 web corrosion.....	116
Table 12.8: Dimension of most common deterioration scenarios for W2 web corrosion pattern.....	118
Table 12.9: Dimension of most common deterioration scenarios for W3 web corrosion pattern.....	120
Table 12.10: Dimension of most common deterioration scenarios for W4 web corrosion pattern....	121
Table 12.11: Dimensions of most common deterioration scenarios for W5 web corrosion pattern ..	122
Table 12.12: Dimensions of most common web hole scenarios	125
Table 12.13: Dimensions of most common stiffener corrosion and hole scenarios	131

List of Figures

Figure 2.1: Distribution of inspection reports per district	6
Figure 2.2: a) Corrosion height and b) length distribution of unstiffened deteriorated ends	7
Figure 2.3: Beam end configurations with one bearing stiffener	7
Figure 2.4: Beam end configurations with two bearing stiffeners.....	8
Figure 2.5: Two bearing configurations considered in study	8
Figure 2.6: Bridge identification and general information at top of spreadsheet	22
Figure 2.7: Summary spreadsheet with designated shadowed areas A–F	23
Figure 3.1: a) Hole through the deck and b) map cracking with heavy efflorescence at O-03-009 bridge (adopted from O03009-0TW-MUN-NBI).....	26
Figure 3.2: Delivery, unloading, and storage of first set of corroded beams.....	26
Figure 3.3: As-received condition for Specimens A and B	27
Figure 3.4: Experimental rig.....	28
Figure 3.5: Side and front view of instrumentation configuration	29
Figure 3.6: Fabrication drawings of Specimen A.....	30
Figure 3.7: Corroded end of Specimen A.....	30
Figure 3.8: a) Contour maps depicting remaining thickness of Specimen A; and b) initial web imperfection for same girder	31
Figure 3.9: Specimen A experimental configuration and dimensions.....	31
Figure 3.10: Instrumentation configuration of Specimen A.....	32
Figure 3.11: Fabrication drawings of Specimen B.....	32
Figure 3.12: Corroded end of Specimen B.....	33
Figure 3.13: Contour maps of remaining thickness along tested end of Specimen B.....	34
Figure 3.14: Specimen B experimental configuration and dimensions.....	34
Figure 3.15: Instrumentation configuration at tested end of Specimen B.....	35
Figure 4.1: Section loss simulation by partitioning web region and assigning thickness levels derived by post-processing point cloud data.....	38
Figure 4.2: a) Measured stress-strain properties of specimen for finite element simulation obtained from (14); b) stress-strain properties for welded parts, according to data provided by manufacturer	38
Figure 4.3: a) Front view of Specimen A; b) initial geometric imperfection as imported to FEM.....	40
Figure 4.4: Developed FEM to simulate experimental procedure of Specimen A.....	41
Figure 4.5: Geometry of POS2 specimen tested by (21).....	42
Figure 4.6: FEM developed to simulate experimental procedure of POS2 specimen.....	42
Figure 4.7: Shape and location of examined deterioration topologies	43
Figure 4.8: Year of construction distribution for bridges studied	44
Figure 4.9: a) Expansion and b) fixed bearing types commonly found supporting corroded plate girders in Massachusetts	46
Figure 4.10: Geometry and FEM for girder configurations used for parametric analysis.....	47
Figure 4.11: Excel sheet describing geometry of tested scenarios	48
Figure 4.12: Set of data extracted and plotted from each group of analyses: a) maximum Von Mises stress magnitude; b) maximum positive and c) negative lateral displacement for every computational step; and d) bearing load at last load increment of each model	49
Figure 5.1: Web corrosion in correlation with a) web holes and b) stiffener condition for C1 configuration.....	52
Figure 5.2: Web corrosion in correlation with a) web holes and b) stiffeners condition for C2 configuration.....	53

Figure 5.3: 16 final corrosion patterns for beam ends with one bearing stiffener, including corrosion and hole patterns for web and stiffeners (shaded areas illustrate corrosion domains).....	56
Figure 5.4: Seven final web corrosion patterns for beam ends with two bearing stiffeners (shaded areas illustrate corrosion domains under assumption of uniform section loss)	57
Figure 5.5: Five final web hole patterns for beam ends with two bearing stiffeners.....	58
Figure 5.6: Final stiffener corrosion pattern and two hole patterns for beams in compliance with C2 configuration; 14 and 15 are holes located at stiffener’s bottom and top, respectively.....	58
Figure 5.7: Comparison of damage cases with one and two bearing stiffeners per web face reveals similar corrosion patterns between configurations (displayed cases include information for web and stiffeners)	59
Figure 6.1: a) Applied load: vertical displacement plot for Specimen A; b) reaction force developed at crossbeam area was calculated from summation of loads captured by east and west load cells .	61
Figure 6.2: Side-by-side images showing side view of web and profile view of beam during experiment (A and B correspond to Fig. 6.1a).....	63
Figure 6.3: Beam’s end lateral displacement profile as recorded from outer (blue) and inner (red) column of potentiometers, for two different loads, 0.9 and 1.0 F_u	64
Figure 6.4: a) Applied load vs. vertical displacement plot for Specimen B; b) total applied load was calculated as difference between reaction force at intact end and summation of two load cells installed at bottom of each rod (west and east side)	65
Figure 6.5: Side-by-side images showing side view of web and profile view of beam during experiment (A and B correspond to Fig. 6.4a).....	67
Figure 6.6: a) Measured web lateral deflections recorded close (red) and far (blue) for partial stiffener for 0.9 and 1 F_u , where F_u denotes maximum applied load; b) remaining thickness profile along web of Specimen B.....	68
Figure 6.7: Both experiments terminated due to inclination of load spread beam, located between hydraulic jacks and bridge bearing.....	69
Figure 7.1: Comparison of experimental and numerical results a) at tested end and b) crossbeam area for Specimen A	72
Figure 7.2: Experimental and numerical a) front and b) side view of Specimen A, at peak load.....	72
Figure 7.3: Comparison between experimental and numerical results for experiment conducted by Mans in composite girder	73
Figure 7.4: Capacity of beam ends with W1 corrosion pattern and imperfection amplitude in range of 0.1 to 2.0 t_{web}	74
Figure 7.5: Effect of stiffener section loss related to a) W1; b) W2; and c) W3 patterns (relationship between bearing capacity and stiffeners’ thickness could be idealized as linear)	75
Figure 7.6: Effect of stiffener corrosion height related to a) W1; b) W2; and c) W3 patterns (stiffeners’ condition at bottom 10% was critical for remaining capacity).....	76
Figure 7.7: Effect of web section loss for scenarios related to a) W1; b) W2; and c) W3 patterns. (In some cases, stiffeners’ contribution minimized aftermath of web section loss; dark- and light-brown shades represent minimum and maximum bounds of examined scenarios).....	76
Figure 7.8: Effect of corrosion length for scenarios related to a) W2; and b-c) W3 patterns. Corrosion length had no effect to bearing capacity when exceeding bearing length by more than 10% of the depth. Dark- and light-brown shades represent minimum and maximum bounds of examined scenarios.	77
Figure 7.9: Effect of corrosion height for scenarios related to a) W1; b) W2; and c) W3 patterns. Corrosion height had no effect to bearing capacity when higher than 10% of depth; dark- and light-brown shades represent minimum and maximum bounds of examined scenarios.....	78
Figure 8.1: Domain for calculation of A_g , according to current provisions	80
Figure 8.2: Contour maps depicting remaining thickness of Specimens a) A and b) B.....	81
Figure 8.3: Beam end with corrosion scenario projected on bottom of web.....	83

Figure 8.4: Comparison between predicted and computationally obtained capacities for current procedures, and a) W1; b) W2; and c) W3 general corrosion patterns (line represents perfect prediction; estimations lying above line overestimate actual strength)	83
Figure 8.5: Parameters for capacity calculation according to proposed equations.....	86
Figure 8.6: For training set, comparison between predicted and computationally obtained capacities for a) W1; b) W2; and c) W3 general corrosion patterns (line represents perfect prediction, while blue and red points depict estimation according to proposed and current provisions)	87
Figure 8.7: Comparison between predicted failure loads and numerical results (blue, red, and black denote 30%, 50%, and 70% stiffener section loss, respectively).....	89
Figure 12.1: Corrosion height distribution for W1 pattern.....	99
Figure 12.2: Web thickness loss distribution for W1 cases with a) deterioration up to 20% of web depth, and b) full height corrosion.....	99
Figure 12.3: a) Length and b) height of W1 web corrosion pattern for beams with one stiffener per web face.....	100
Figure 12.4: a) Hole length; b) height; c) distance from the bottom flange; and d) nomenclature of H4 pattern	100
Figure 12.5: Distribution of deterioration characteristics for W2 corrosion scenario for beams with unique stiffener above bearing.....	102
Figure 12.6: a) Length and b) height of H2 holes associated with W2 web corrosion pattern for beams with unique stiffener above bearing.....	103
Figure 12.7: Distribution of deterioration characteristics for W3 corrosion scenario for beams with unique stiffener above bearing.....	104
Figure 12.8: a) Length and b) height of H2 holes associated with W3 web corrosion pattern for beams with unique stiffener above bearing.....	105
Figure 12.9: Corrosion height and length distribution of W4 corrosion pattern for beams with unique stiffener above bearing	106
Figure 12.10: Thickness loss distribution of W4 corrosion pattern for beams with one bearing stiffener	106
Figure 12.11: a) Hole length and b) height of H1 holes reported with W4 corrosion pattern, for beams with one bearing stiffener	107
Figure 12.12: a) Hole length and b) height of H2 holes reported with tW4 corrosion pattern, for beams with one bearing stiffener	107
Figure 12.13: Distribution of W5 deterioration characteristics for beams with unique stiffener above bearing	109
Figure 12.14: Recorded dimensions of H1 holes associated with W5 web corrosion pattern for beams with unique bearing stiffener	110
Figure 12.15: Recorded dimensions of H2 holes associated with W5 web corrosion pattern for beams with unique bearing stiffener	110
Figure 12.16: Recorded dimensions of H3 holes associated with the W5 web corrosion pattern for beams with a unique bearing stiffener.	110
Figure 12.17: Recorded dimensions of H4 holes associated with W5 web corrosion pattern for beams with unique bearing stiffener	111
Figure 12.18: a) Corrosion height and b) section loss of stiffeners for beams with one bearing stiffener.....	114
Figure 12.19: Hole height and length of corroded stiffeners for beams with one bearing.	114
Figure 12.20: a) Corrosion height and b) section loss distribution of W1 corrosion pattern for beams with two bearing stiffeners per web face.....	116
Figure 12.21: a) Corrosion height; b) length; and c) section loss of W2 corrosion pattern for beams with two bearing stiffeners	117
Figure 12.22: Corrosion height of W1 pattern when $CL \neq 0$, for beams with two bearing stiffeners	118

Figure 12.23: a) Corrosion height; b) length; and c) section loss of W3 corrosion pattern for beams with two bearing stiffeners	119
Figure 12.24: Distribution of deterioration characteristics for W4 corrosion scenario for beams with two bearing stiffeners	120
Figure 12.25: Distribution of deterioration characteristics for W5 corrosion scenario for beams with two bearing stiffeners	121
Figure 12.26: a) Hole height and b) length distribution of H1 pattern for beams with two bearing stiffeners	122
Figure 12.27: a) Hole height; b) length; and c) distance from bottom flange for H4 pattern.....	123
Figure 12.28: a) Hole height and b) length distribution of H3 pattern for beams with two bearing stiffeners	123
Figure 12.29: a) Hole height and b) length distribution of H4 pattern for beams with two bearing stiffeners	124
Figure 12.30: a) Hole length and b) height distribution of H4 pattern for beams with two bearing stiffeners	124
Figure 12.31: Corrosion height of a) S1 and b) S2 for beams with W1 web corrosion pattern	126
Figure 12.32: Corrosion height of S2 for beams with W3 web corrosion pattern.....	126
Figure 12.33: Corrosion height of a) S1 and b) S2 for beams with W3 web corrosion pattern	126
Figure 12.34: Corrosion height of a) S1 and b) S2 for beams with W4 web corrosion pattern	127
Figure 12.35: Corrosion height of a) S1 and b) S2 for beams with W5 web corrosion pattern	127
Figure 12.36: Corrosion height of a) S1 and b) S2 for beams without available web corrosion data	127
Figure 12.37: Corrosion height of a) S1 and b) S2 for all beams.....	128
Figure 12.38: Thickness loss distribution of a) S1 and b) S2 for whole sample	128
Figure 12.39: Dimensions of holes located at S1 bottom.....	129
Figure 12.40: Dimensions of holes located at S2 bottom.....	129
Figure 12.41: Dimensions of holes located at top part of stiffeners.....	130

List of Acronyms

Acronym	Expansion
α	Distance between Bearing Stiffeners
B _L	Bearing Length
c	Distance between Bearing Stiffener and Web Edge
C _H	Corrosion Height
C _L	Corrosion Length
d _w	Web Depth
FEM	Finite Element Model
HH	Hole Height
HL	Hole Length
N	Bearing Length
SC	Stiffener Corrosion Height
SHH	Stiffener Hole Height
SHL	Stiffener Hole Length
t _{wloss}	Web Thickness Loss
t _{sloss}	Stiffener Thickness Loss
t _{web}	Intact Web Thickness
t _{loss}	Intact Stiffener Thickness
t _w	Remaining Web Thickness
t _{ave}	Average Remaining Thickness

This page left blank intentionally.

1.0 Introduction

1.1 Background Information

Infrastructure is the backbone of the United States' prosperity, affecting every aspect of life, from access to drinking water to electricity distribution. For the first time in 20 years (1), the overall grading of the United States' infrastructure has improved from fair to good, with some elements still exhibiting significant deficiencies in condition and functionality. In that same report, among the many aspects of the problem, the criticality of the existing condition and the gap between the total needs and the estimated funding are highlighted. It is worth noting that the continued underinvestment in the infrastructure has resulted in a funding gap that approaches \$2.6 trillion.

The overall tendency of improved ratings for infrastructure can also be observed in regard to highway bridges, thanks to concentrated efforts by the involved agencies. The total number of deficient bridges was reduced from over 50,000 to 46,154 in four years; however, the average age of bridges has been increased to 44 years, and the estimated bridge repair needs to \$125 billion (1). A bridge can be characterised as structurally deficient if at least one of its components has a condition rating of poor or worse. The critical components are the deck, superstructure, and substructure or culvert. For steel bridges, corrosion is considered among the main aspects of structural deficiency affecting the load-bearing component and is mainly attributed to malfunctioning deck expansion joints.

Joints are permanently exposed to natural and human-originated deterioration factors speeding up their aging process. As a result, joints fail to prevent water or deicing mixtures from penetrating into the bearing area, where the beams are subjected to patch loading. The leaking water contains high concentrations of chemicals employed seasonally to winterize the road above. Deterioration of the steel is most often initiated by the buildup of this runoff triggering a corrosive process in the bottom flange and the components above it. When this condition is sustained, it can ultimately result in severe thickness loss, directly affecting the girder load-bearing capacity and, consequently, the capacity of the bridge.

To ensure public safety, authorities perform periodic bridge inspections, during which point thickness measurements are obtained in an effort to quantify the uneven and highly stochastic section loss. According to the Massachusetts Dept. of Transportation's (MassDOT) *Bridge Inspection Handbook* (2) the load-live carrying capacity of bridges is evaluated on a decade basis unless concern occurs due to the critical conditions of an asset. In that case, the inspectors can warrant a load rating request, and the obtained thickness measurements are combined with analytical tools to estimate the remaining bearing capacity of corroded girders.

This research attempts to evaluate the current provisions based on real corrosion data and, ultimately, to provide new closed-form equations for more accurate capacity estimations.

1.2 Literature Review

A pioneering study on the effect of corrosion to the bearing strength of steel bridges was conducted by Kayser et al. (3), who numerically examined the effect of section loss along unstiffened girders. Van de Lindt et al. (4) developed guidelines for deteriorated steel beam ends. Initially, damage simulations of various sizes and shapes were performed using the finite element method (FEM). Experimental work was conducted on beams 3 feet in length, with artificial web and flange thickness reduction above the bearing, also validating the FEM model. Ultimately, a deterioration factor was proposed as a simplified approach for calculating capacity reduction of deteriorated girders.

Since then, researchers have studied the beam end corrosion problem of plate girders both experimentally and numerically. Even though the work of Sugimoto et al. (5) focuses on railway bridges, it is worth noting that experimental testing was conducted on both decommissioned riveted plate girders and girders with artificial section loss. Eventually, they proposed analytical expressions describing a linear relationship between the shear strength and thickness loss ratios. Kim et al. (6) experimentally explored the shear behavior of corroded web panels, concluding that deterioration results in larger failure regions. From the same research group, Ahn et al. (7) conducted experiments representing web panels with pitting and through-thickness corrosion damage, reporting their significant impact on the shear buckling behavior when they extend to a critical corrosion damage level in the diagonal tension field. In a previous work (8) focusing on both computational and experimental research, a reduction factor to estimate the residual shear strength of plate girders with web damage was proposed. A study by Khurram et al. (9) explored the effect of local corrosion damage along the bearing stiffeners and the end panel, both experimentally and computationally, indicating that the minimum thickness within any damage height may be used to simulate the corrosion damage in a computational analysis.

In an exclusively computational work, Ahn et al. (10) concluded that the damage shape (triangular or rectangular) affected the plate girder's capacity only when it intersected with the tension field of the web panel. Usukura et al. (11) employed the FEM in a sensitivity analysis to explore the capacity and the collapse mechanism of plate girders with corroded ends. Liu et al. (12) investigated the impact of corrosion height and thickness reduction of steel girders with stiffeners. Finally, Yamaguchi et al. (13) highlighted the effect of the web corrosion pattern on the shear capacity of edge panels.

It is worth noting that the majority of the previously mentioned research studies intentionally focused on the panel shear failure by accounting for strong bearing stiffeners without corrosion.

Data acquired by the authors from inspection reports and inspectors' observations in Massachusetts, however, indicated that stiffeners most often undergo severe section loss due to corrosion. Another point of concern emerges from the fact that, except for the work of Sugimoto et al. (5) on railway bridges, the available studies experimentally studied the corrosion effect assuming a uniform reduction of thickness in girder web and, sometimes, the stiffeners. However, given the corrosion topological nonuniformity in the field, this approach

might not be able to capture failure mechanisms related to the variability of the corrosion phenomenon.

1.3 Research Goals

This research work aimed to address the previously mentioned limitations and constitutes part of a wider effort by the project team toward a comprehensive protocol for steel bridge inspection and evaluation. In previous studies (*14,15,16,17*), the team tested naturally corroded specimens and proposed new equations for capacity assessment of steel bridges, while in a complementary study, the team explored the use of 3D laser scanning for mapping of the remaining section along corroded specimens. In Phases I–III of this study, the previously developed methodologies were combined to explore the mechanics of plate girders with corroded ends. The immediate research objectives were as follows.

- **The identification and quantification of the most common corrosion topologies.** During the first step of this work, the current deterioration condition of bridges with plate girders was studied through MassDOT inspection reports of viaducts that had experienced beam end corrosion. Deterioration data on thickness loss, corroded area size, and location were collected and analyzed for 210 corroded ends. The data were used to define the upper bounds and the range of variability for the parameters that describe the most common corrosion topologies in the Commonwealth of Massachusetts.
- **To investigate the failure mechanism of corroded stiffened girders.** Two specimens were tested based on naturally corroded rolled girders obtained from decommissioned bridges in the Commonwealth of Massachusetts. The first specimen was designed to resemble plate girders, while the second one explored the mechanics of rolled girders with partial stiffening plates as part of diaphragms connections.
- **The calibration of a high-fidelity composite girder-level finite element model.** The experimentally obtained data from the fully stiffened girder, as well as data obtained from the literature, were used to develop a finite element model that accounts for material and geometric nonlinearities, using the commercial software ABAQUS.
- **To define the parameters that significantly affect capacity reduction.** The previously developed finite element model was combined with the identified corrosion patterns to perform an extensive parametric analysis aimed to investigate the geometric bound of a region whose condition substantially affects the residual bearing capacity of plate girders.
- **To provide new sets of equations for more accurate capacity assessment.** Combining conclusions derived from the previously conducted parametric analysis with a data set of more than 1,000 scenarios, new procedures were trained and validated for the capacity assessment of plate girders with end corrosion.

This page left blank intentionally.

2.0 Methodology for Categorization of Corrosion Topologies

This section includes the methodology for Phase I of the project. The goal of this phase was to identify the most common shapes and locations for steel beam end deterioration. To accomplish this, the authors reviewed inspection reports for various bridges and present here the data collection process, the tools built to process the data, and the preliminary filtering of the data. The post-processing of the data is described in Section 5.

2.1 Data Collection

The data collection process was based on the inspection report documents provided by the six MassDOT Highway Districts. The conducted research focused on bridges with poor superstructure condition.

2.1.1 Format of Data

In the Commonwealth of Massachusetts, the Department of Transportation (MassDOT) is the driving force for assessing the condition of steel bridges. In its efforts to ensure safety and maintain the infrastructure of the state, MassDOT engineers perform periodic bridge inspections that conform to the requirements of the Code of Federal Regulations (18). MassDOT has introduced and is currently using a variety of standard inspection report forms (2) that fulfill the requirements of the National Bridge Inspection Standards. These reports provide extensive information for the overall condition of the structure (e.g., deck, superstructure, substructure, and culvert) in the form of figures, text, photos, and sketches gathered by inspection engineers.

The data collection was based on the inspection report documents provided by the six MassDOT Highway Districts. A detailed description of the inspection reports, as well as of the challenges faced to extract data from the reports, was reported by the researchers in the final published report of the previous project (14).

2.1.2 Amount of Data

The project team was provided with 216 reports for 168 different bridges. The available reports per district varied from 2 to 118, as shown in Fig. 2.1.

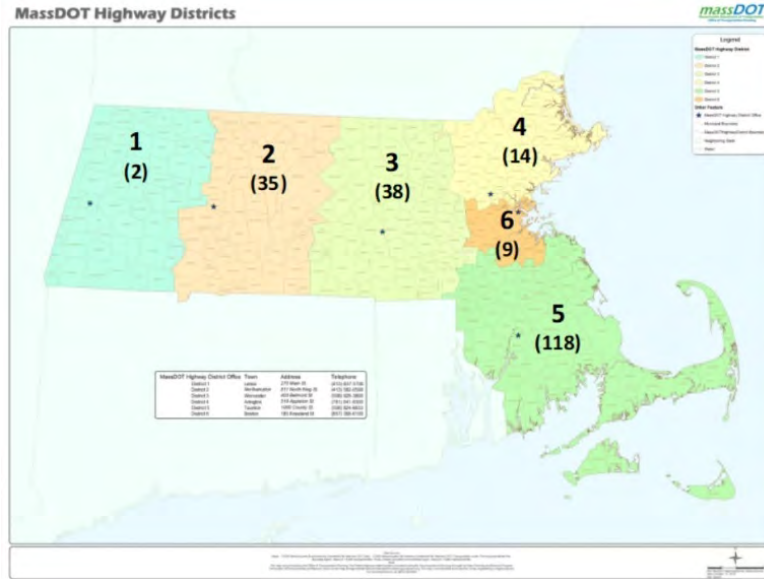


Figure 2.1: Distribution of inspection reports per district

Table 2.1 presents the classification of the available reports based on their general properties. The first column of Table 1 includes the different districts of MassDOT, while the second column includes the total number of inspection reports received from each district. This information is the same as that shown in the map in Fig. 2.1.

The third column of Table 2.1 identifies the number of reports provided for bridges with unstiffened beam ends. The fourth column includes reports that involved other types of bridges, such as floor beam systems or concrete jack arches hidden by stay-in-plane (SIP) forms, which are outside of the current research scope. A total of 33 reports described the same bridges (regardless of type) at different time intervals. Finally, 30 of the available inspection reports were describing viaducts with stiffened ends (15% of total), and, consequently, these reports constituted the database for data acquisition.

Table 2.1: Classification of available inspection reports based on general properties

District #	All	Unstiffened	Other bridge types	Reports showing deterioration over time	Stiffened
District 1	2	2	0	0	0
District 2	35	29	5	0	1
District 3	38	20	2	12	4
District 4	14	6	0	8	0
District 5	118	73	8	13	24
District 6	9	0	8	0	1
Total	216	130	23	33	30

The data included in the 30 reports allowed the project team to study in detail 210 corroded beam ends. This number is lower compared to the 93 reports and the 808 beam ends that the researchers studied to explore the corrosion topologies of the unstiffened beam ends. Fig. 2.2 presents the corrosion height (CH_1) and length (CL_1) distribution normalized to web depth

(d_w) for an orthogonal-shaped corrosion topology. Blue denotes the distribution based on the data from the full sample (808 beam ends), while red denotes the distribution for the first quarter of them. It can be concluded that even with 25% of the data sample, it is possible to capture satisfactorily the main trends. It should be also noted that the computational power during the upcoming parametric analysis is expected to cover a wide range of cases.

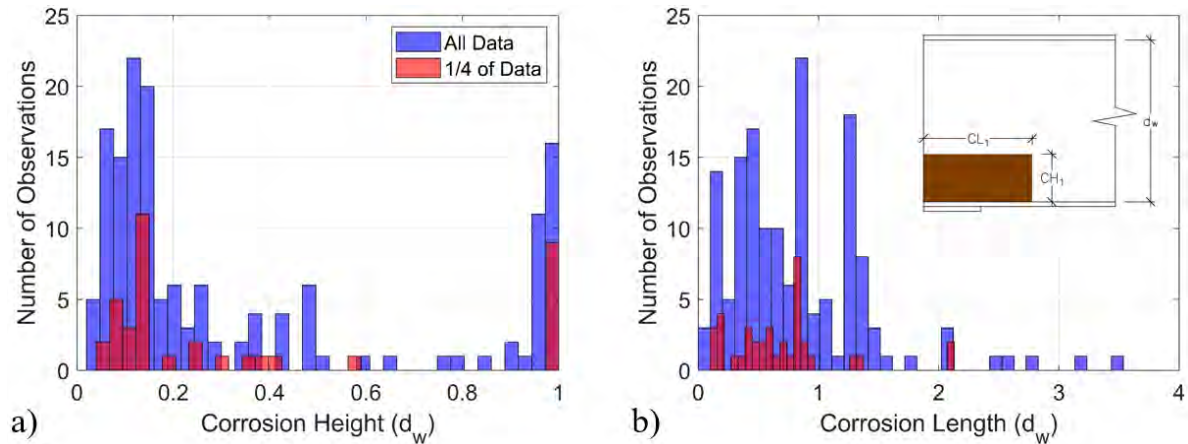
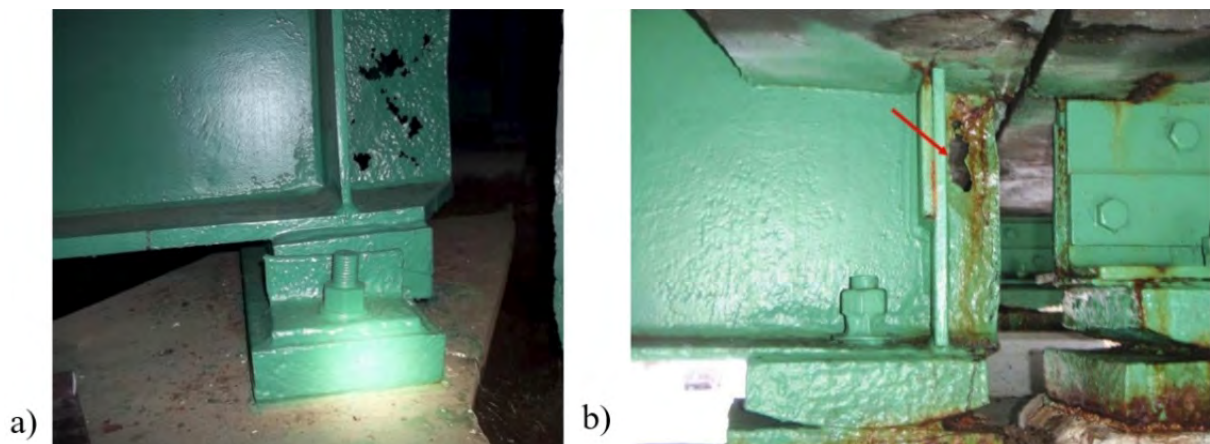


Figure 2.2: a) Corrosion height and b) length distribution of unstiffened deteriorated ends

2.2 Definition and Quantification of the Phenomenon

2.2.1 Beam End Configuration

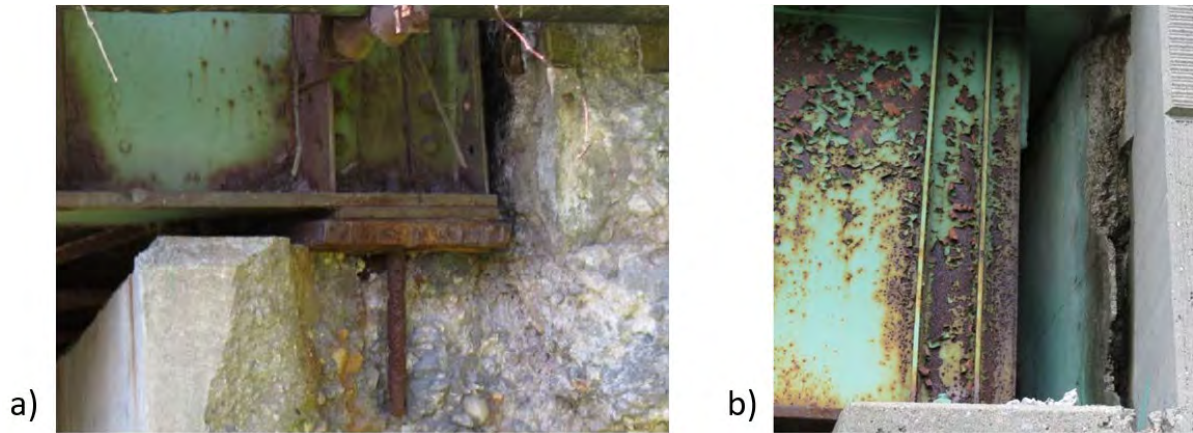
A preliminary look at the received data revealed a variability of the beam configuration at the support area, regarding the number of stiffeners at each web face and their location. In particular, one (Fig. 2.3) or two (Fig. 2.4) bearing stiffeners were found welded at each web face above the support.



Sources: Adopted from a) W46011-3YK-DOT-NBI (District 5, Town of Wrentham); b) W30026-3WB-DOT-NBI (District 5, Town of Westport).

Figure 2.3: Beam end configurations with one bearing stiffener

In case where two stiffeners were employed (Fig. 2.4), an additional source of variability emerged in terms of their location with respect to the bearing. Two techniques were detected: first, the distance between the adjacent stiffeners matched the bearing length (Fig. 2.4a); and second, the stiffeners lay within the bearing area (Fig. 2.4b). Finally, for beam ends with one bearing stiffener, there were reported cases where partial bearing stiffeners had been welded to the end diaphragm connection plate as a repairing technique to provide an alternative load path to corroded ends (Fig 2.3b).



Sources: Adopted from a) W44063-1LA-DOT-NBI (District 3, City of Worcester); b) B06022-2AR-DOT-NBI (District 3, Town of Bellingham).

Figure 2.4: Beam end configurations with two bearing stiffeners

Beam ends falling into the last configuration (with the partial stiffeners) did not meet the research goals of the current work and thus were not studied. In addition, the relative distance between the bearing stiffeners did not seem to affect the corrosion topologies; consequently, these two cases were merged, and a parameter “ α ” was introduced to describe the position of the bearing stiffeners with respect to the bearing length “ N ”. Fig. 2.5 summarizes the two final configurations that were considered for the next stages of this work. Configuration C1 describes beam ends with a unique bearing stiffener along each web face, while C2 describes a case where the number of stiffeners increased to two.

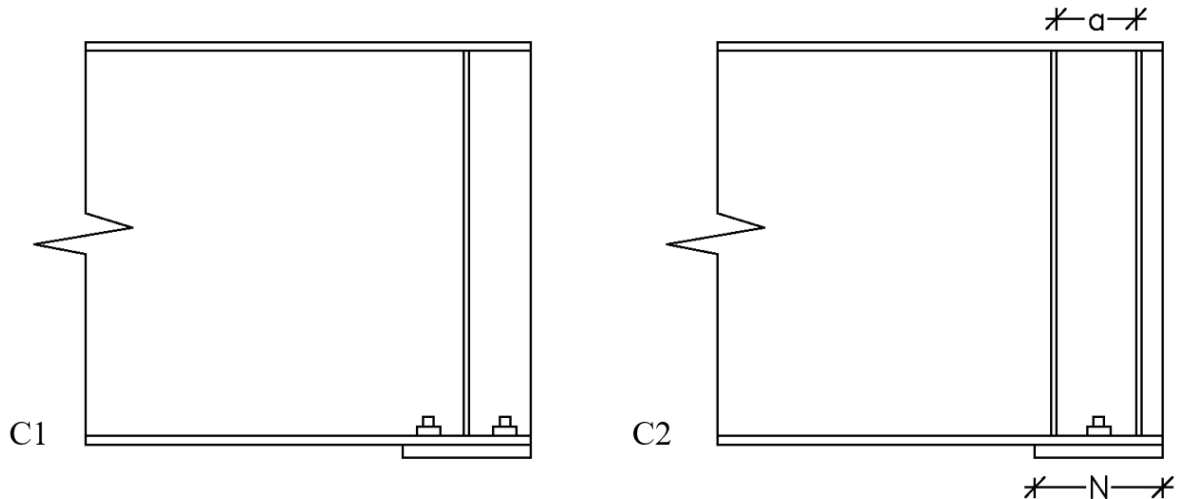


Figure 2.5: Two bearing configurations considered in study

2.2.2 General Categorization of Corrosion and Hole Patterns

The first stage of post-processing involved the development of general patterns for section loss and patterns of holes based on the first observations of all the data for the 210 beam ends. This approach allowed the researchers to group and study cases with common characteristics. The categorization advanced based on the C1 and C2 discretization and also included stiffeners deterioration. A general remark is that stiffeners divided the above support web area to two (C1) or three (C2) independent domains. This geometric characteristic potentially restrained the water flow path from the leaking joints, resulting in many cases to corroded areas with distinct bounds set by stiffeners.

Web Corrosion Patterns for C1 Configuration

Based on the observations of the inspection reports, five web corrosion patterns, which were the most common ones, were defined. Thickness loss was considered uniform along the whole corroded area (Tables 2.2–2.6).

Table 2.2: Web corrosion pattern W1 for C1 configuration

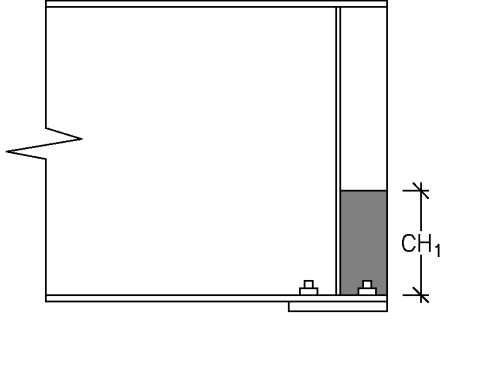
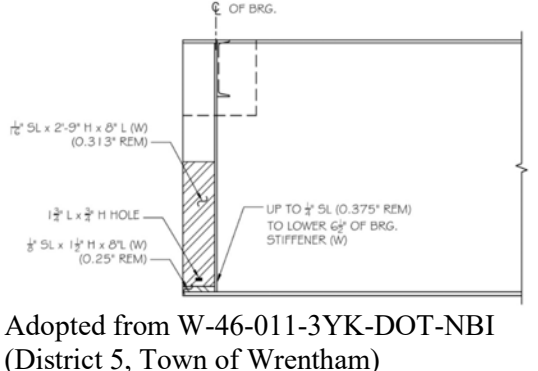
Pattern	Pattern shape	Example from an inspection report
W1		 <p>Adopted from W-46-011-3YK-DOT-NBI (District 5, Town of Wrentham)</p>
<p>Short description: Corrosion height (CH_1) is the unique geometric characteristic of W1 pattern, set to describe a damage area that covers the full length between the stiffener and the beam end. The sketch on the right shows a typical case of W1.</p>		

Table 2.3: Web corrosion pattern W2 for C1 configuration

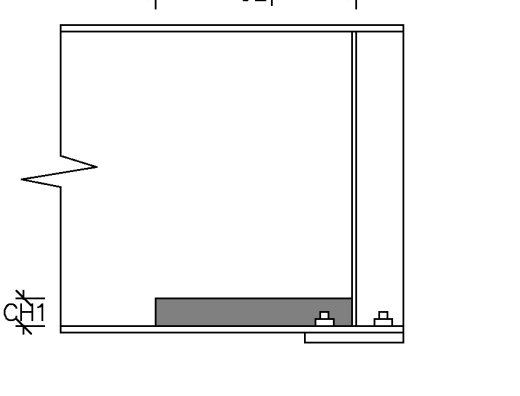

Pattern	Pattern shape	Example from an inspection report
W2		 <p data-bbox="928 634 1398 695">Adopted from N-06-020-3U1-DOT-NBI (District 5, City of New Bedford)</p>
<p>Short description: Corrosion height (CH_1) and length (CL_1) are the two geometric characteristics of W2 pattern. The damaged area is located at the web bottom and expands along the longitudinal axis of the beam. The photograph on the right shows a typical case of W2.</p>		

Table 2.4: Web corrosion pattern W3 for C1 configuration

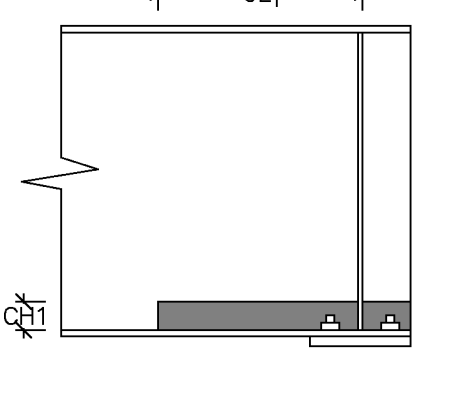

Pattern	Pattern shape	Example from an inspection report
W3		 <p data-bbox="868 1312 1414 1367">Adopted from M-05-006-47X-DOT-NBI (District 5, Town of Marion)</p>
<p>Short description: The W3 corrosion pattern for C1 configuration is a combination of W1 and W2. The damaged area is equally high along the two sides of the bearing stiffener. The photograph on the right shows a typical case of W3.</p>		

Table 2.5: Web corrosion pattern W4 for C1 configuration

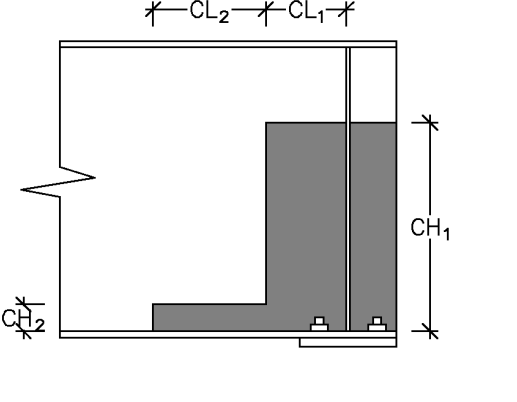

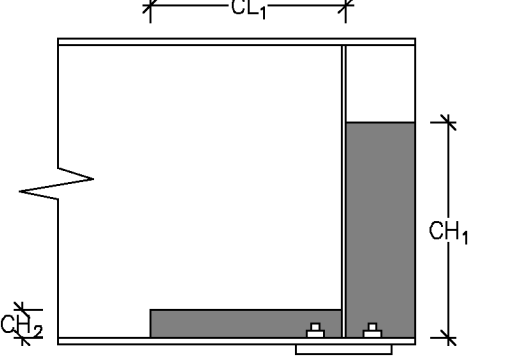

Pattern	Pattern shape	Example from an inspection report
W4	 <p>The diagram shows a cross-section of a web with a bearing stiffener. Two corrosion regions are shown: a larger one on the right with height CH_1 and length CL_1, and a smaller one on the left with height CH_2 and length CL_2. The corrosion extends along both sides of the stiffener.</p>	 <p>Adapted from F-07-045-4PH-DOT-NBI (District 3, City of Framingham)</p> <p>Short description: Two corrosion heights (CH_1, CH_2) and two corrosion lengths (CL_1, CL_2) have been introduced to describe the W4 deterioration scenario, where the damaged area with varying deterioration height extends along both sides of the bearing stiffener. The photograph on the right shows a typical case of W4.</p>

Table 2.6: Web corrosion W5 for C1 configuration

Pattern	Pattern shape	Example from an inspection report
W5	 <p>The diagram shows a cross-section of a web with a bearing stiffener. Two corrosion regions are shown: a larger one on the right with height CH_1 and a smaller one on the left with height CH_2. A single corrosion length CL_1 is indicated for the entire length of the stiffener. The area between the stiffener and the outer web edge is considered corroded along the whole length.</p>	 <p>Adapted from M-05-006-47X-DOT-NBI (District 5, Town of Marion)</p> <p>Short description: Two corrosion heights (CH_1, CH_2) and a corrosion length (CL_1) have been introduced to describe the W5 deterioration scenario. The damaged extends along both sides of the bearing stiffener, with different height at each domain. The area between the stiffener and the outer web edge is considered corroded along the whole length. The photograph on the right shows a typical case of W5.</p>

Web Hole Patterns for C1 Configuration

Based on observations of the inspection reports, five web hole patterns were developed to describe the most common cases (Tables 2.7–2.11).

Table 2.7: Web hole pattern H1a for C1 configuration

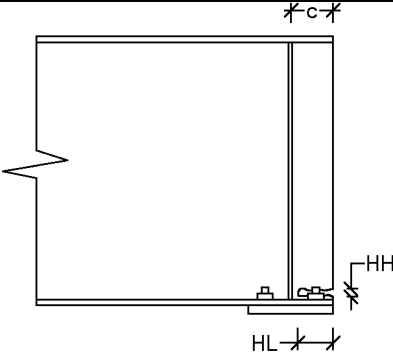

Pattern	Hole shape	Example from an inspection report
H1a		 <p>Adopted from M-05-006-47X-DOT-NBI (District 5, Town of Marion)</p>
	<p>Short description: H1a is a case where a hole appears at the lower part of the web; it initiates at the web edge and extends longitudinally at the domain behind the bearing stiffener. HH is the height of the hole, and HL is the length of the hole. HH is expressed normalized to web depth (d_w) and HL normalized to c, where c is defined in the sketch on the left. The photograph on the right shows a typical case of H1a.</p>	

Table 2.8: Web hole pattern H1b for C1 configuration

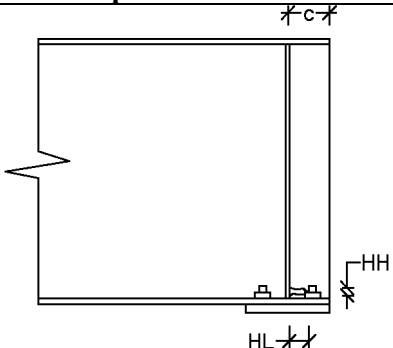
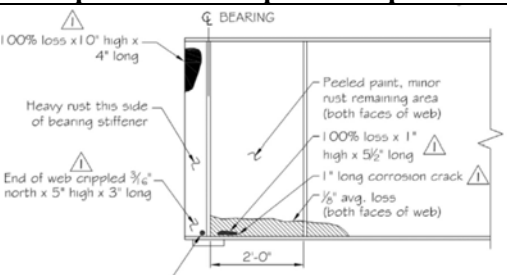
Pattern	Hole shape	Example from an inspection report
H1b		 <p>Adopted from N-06-020-3U0-DOT-NBI (District 5, City of New Bedford)</p>
	<p>Short description: H1b is differentiated by H1a on the hole starting edge. The hole begins at the intersection of the stiffener and the hole. The sketch on the right includes a case of H1b.</p>	

Table 2.9: Web hole pattern H2 for C1 configuration

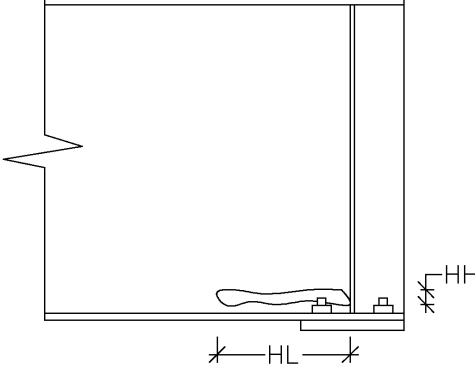

Pattern	Hole shape	Example from an inspection report
H2		 <p data-bbox="894 604 1377 661">Adopted from N-06-020-3U0-DOT-NBI (District 5, City of New Bedford)</p>
<p>Short description: H2 is a case where the hole appears just in front of the bearing stiffener and expands along the longitudinal beam axis. HH is the height of the hole, and HL is the length of the hole. Both parameters are expressed normalized to web depth (d_w). The photograph on the right shows a typical case of H2.</p>		

Table 2.10: Web hole pattern H3 for C1 configuration

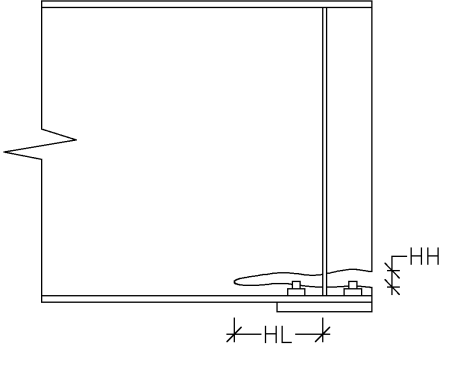

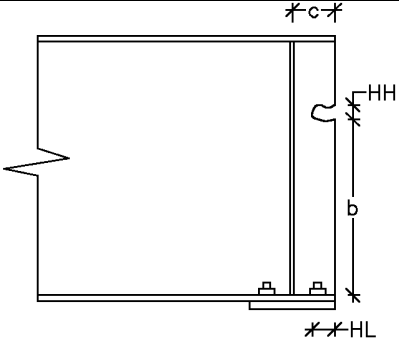

Pattern	Hole shape	Example from an inspection report
H3		 <p data-bbox="894 1287 1393 1346">Adopted from W-29-057-4QE-DOT-NBI (District 6, Town of Weston)</p>
<p>Short description: H3 is a case where a hole appears at the bottom of the beam. The hole initiates from the outer web edge and expands with similar height beyond the bearing stiffener. HH is the height of the hole, and HL is the length of the hole beyond the stiffener. Both parameters are expressed with respect to the web depth (d_w). The photograph on the right shows a typical case of H3.</p>		

Table 2.11: Web hole pattern H4 for C1 configuration

Pattern	Hole shape	Example from an inspection report
H4		 <p data-bbox="894 611 1382 674">Adopted from W-29-057-4QE-DOT-NBI (District 6, Town of Weston)</p>
<p>Short description: H4 is similar to H1a case, but it is differentiated in terms of location. Parameter b is employed to describe the hole location in respect to the web bottom and is expressed as a percentage of web depth (d_w). HH is the height of the hole, and HL is the length of the hole. HH and HL are expressed with respect to the web depth (d_w) and c respectively. The photograph on the right shows a typical case of H4.</p>		

At this point, it must be mentioned that each web corrosion pattern can be combined only with hole patterns that appear within the corresponding deterioration domain (e.g., W2 cannot be combined with the H1a or H1b hole scenarios). In addition, more than one hole can be present at a corroded beam end. Thus, the researchers defined the following combinations based on inspection report observations: H1 + H2, H1 + H4, and H3 + H4.

A general observation emerging from the inspection reports was that due to the established documentation techniques and the similarities that the deterioration patterns appeared to have, it was often hard to distinguish H1a from H1b and W3 from W5. To partially overcome this issue, data relevant to H1a and H1b were recorded in respect to a unified hole pattern H1, which accounted for HH and HL , regardless of the initiation point of the hole (web edge or stiffener). During the numerical investigation (Task 2), the effect of holes according to H1a and H1b patterns was investigated.

Web Corrosion Patterns for C2 configuration

Based on the observations of the inspection reports, five web corrosion patterns representing the most common ones were defined (Tables 2.12–2.16).

Table 2.12: Web corrosion pattern W1 for C2 configuration

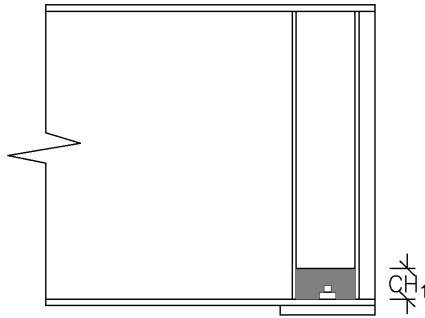

Pattern	Pattern shape	Example from an inspection report
W1		 <p>Adopted from S-35-013-3YB-DOT-NBI (District 5, Town of Swansea)</p>
<p>Short description: Corrosion height (CH_1) is the unique parameter of W1 pattern, which describes web section loss along the whole length of the domain between the bearing stiffeners. The photograph on the right shows a typical case of W1.</p>		

Table 2.12: Web corrosion pattern W2 for C2 configuration

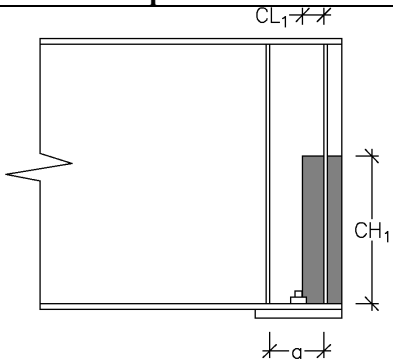
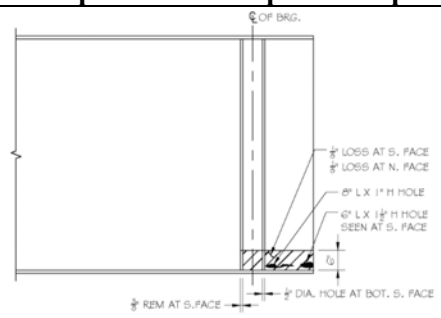
Pattern	Pattern shape	Example from an inspection report
W2		 <p>Adopted from F-02-071-3MJ-DOT-NBI (District 5, Town of Fall River)</p>
<p>Short description: W2 describes a damage area which covers the whole length of the domain between the outer stiffener and the web edge, and can also expand along the area between the two bearing stiffeners (with length α). The corroded area has uniform height CH_1, while the value of CL_1 can be in the range between 0 and α. The sketch on the right shows a typical case of W2.</p>		

Table 2.13: Web corrosion pattern W3 for C2 configuration

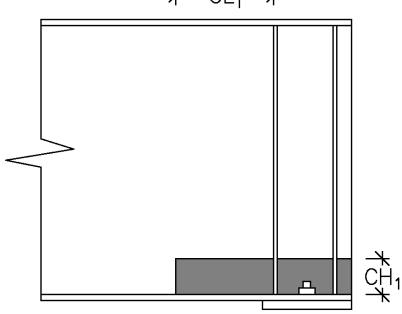
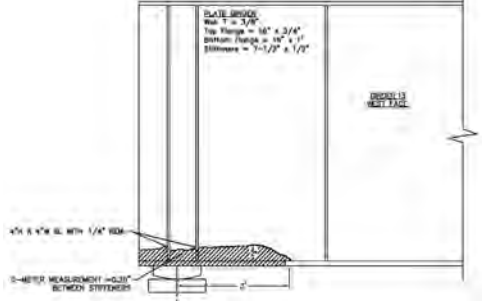
Pattern	Pattern shape	Example from an inspection report
W3		 <p>Adopted from F-02-082-3XK-DOT-NBI (District 5, Town of Fall River)</p>
<p>Short description: Corrosion height (CH_1) and length (CL_1) are the two geometric characteristics employed to describe the W3 pattern, where the damaged area initiates from the outer web edge and expands with uniform height beyond the two bearing stiffeners. The sketch on the right shows a typical case of W3.</p>		

Table 2.14: Web corrosion pattern W4 for C2 configuration

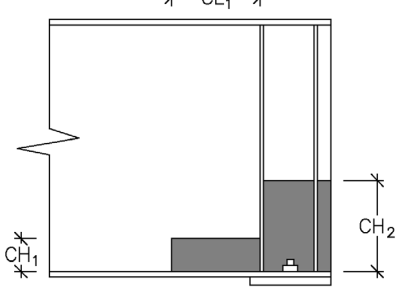

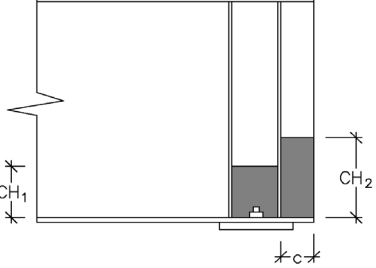
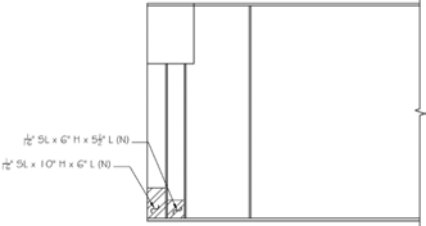
Pattern	Pattern shape	Example from an inspection report
W4		 <p>Adopted from W-46-011-3YK-DOT-NBI (District 5, Town of Wrentham)</p>
<p>Short description: Two corrosion heights (CH_1, CH_2) and a corrosion length (CL_1) have been introduced to describe the W4 deterioration scenario, where the damaged area with varying deterioration height, initiates from the outer web edge and expands beyond the two bearing stiffeners. The photograph on the right shows a typical case of W4.</p>		

Table 2.15: Web corrosion pattern W5 for C2 configuration

Pattern	Pattern shape	Example from an inspection report
W5		 <p>Adopted from W-46-008-3VL-DOT-NBI (District 5, Town of Wrentham)</p>
<p>Short description: Two different corrosion heights (CH_1, CH_2) are the two geometric characteristics employed to describe the W5 pattern, where the damaged area initiates from the outer web edge and covers the full length of the domain between the two bearing stiffeners. The corrosion height differs before and after the outer bearing stiffener. The sketch on the right shows a typical case of W5.</p>		

Hole patterns for C2 configuration

Based on observations of the inspection reports, five web hole patterns were developed to describe the most common cases (Tables 2.17–2.21).

Table 2.16: Web hole pattern H1 for C2 configuration

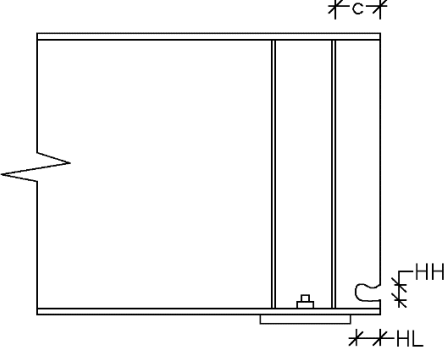

Pattern	Hole shape	Example from an inspection report
H1		 <p>Adopted from W-46-008-3VL-DOT-NBI (District 5, Town of Wrentham)</p>
<p>Short description: H1 is a case where a hole appears at the lower part of the web. It initiates either at the web edge or the outer stiffener and extends longitudinally at the domain between the stiffener and the web edge. HH is the height of the hole, and HL is the length of the hole. HH is normalized with respect to web depth (d_w) and HL with respect to c. The photograph on the right shows a typical case of H1.</p>		

Table 2.17: Web hole pattern H2 for C2 configuration

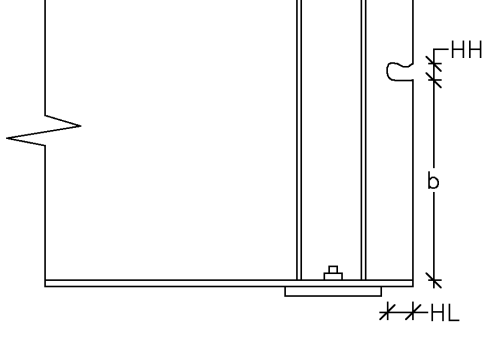

Pattern	Hole shape	Example from an inspection report
H2		 <p data-bbox="901 604 1404 661">Adopted from W-46-008-3VL-DOT-NBI (District 5, Town of Wrentham)</p>
<p>Short description: H2 is similar to an H1 case, but it is differentiated in terms of location. Parameter b is employed to describe the hole location from the web bottom and is expressed with respect to web depth (d_w). HH is the height of the hole, and HL is the length of the hole. HH and HL are expressed with respect to d_w and c respectively. The photograph on the right shows a typical case of H2.</p>		

Table 2.18: Web hole pattern H3 for C2 configuration

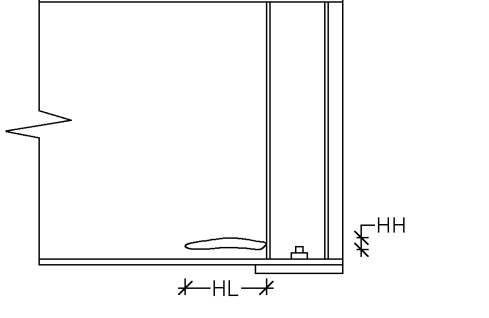

Pattern	Hole shape	Example from an inspection report
H3		 <p data-bbox="901 1276 1404 1333">Adopted from W-44-063-1LA-DOT-NBI (District 5, City of Worcester)</p>
<p>Short description: H3 is a case where the hole appears in front of the inner bearing stiffener and expands along the longitudinal beam axis. HH is the height of the hole, and HL is the length of the hole. Both parameters are expressed with respect to the web depth (d_w). The photograph on the right shows a typical case of H3.</p>		

Table 2.19: Web hole pattern H4 for C2 configuration

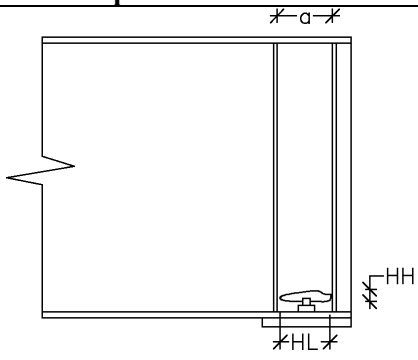

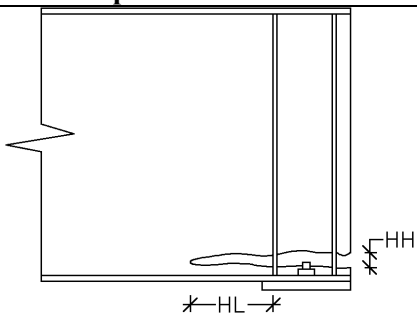

Pattern	Hole shape	Example from an inspection report
H4		 <p>Adopted from F-02-071-3MJ-DOT-NBI (District 5, Town of Fall River)</p>
<p>Short description: H4 pattern describes a hole at the lower part of the web, located between the bearing stiffeners. HH is the height of the hole, and HL its length. HH is expressed with respect to web depth (d_w), and HL is normalized to α, where α is the distance between the stiffeners. The photograph on the right shows a typical case of H4.</p>		

Table 2.20: Web hole pattern H5 for C2 configuration

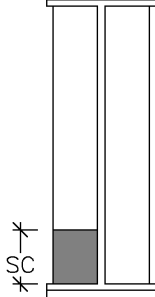

Pattern	Hole shape	Example from an inspection report
H5		 <p>Adopted from B-06-022-2AR-DOT-NBI (District 3, Town of Bellingham)</p>
<p>Short description: H3 is a case where a hole appears at the bottom of the beam. The hole initiates from the outer web edge and expands with similar height beyond the bearing stiffeners. HH is the height of the hole, and HL is the length of the hole beyond the inner bearing. Both parameters are expressed with respect to the web depth (d_w). The photograph on the right shows a typical case of H3.</p>		

Similar to the C1 configuration, more than one hole can be present at a corroded beam end. Thus, the researchers defined the following combinations based on inspection reports observations: H1 + H2 and H3 + H4.

Stiffener corrosion and holes

Regarding stiffeners nomenclature at C2 configuration, the stiffener at the side toward the span is referred to as “S1,” and the one near the backwall or centerline of pier is referred to as “S2.” The stiffener corrosion pattern assumed that the deterioration extends to its full width.

Table 2.21: Stiffener corrosion pattern

Pattern	Hole shape	Example from an inspection report
N/A		 <p>Adopted from B-06-043-487-DOT-NBI (District 3, Town of Wareham)</p>
<p>Short description: SC is the unique parameter employed to describe the corrosion height along its surface. The photograph on the right shows a typical case of stiffener corrosion.</p>		

Similar to the web corrosion, the thickness loss was considered uniform for the whole area. The corrosion height (SC) was taken from the inspection reports, and in case no information was provided, no corrosion along the stiffeners was considered. In cases where corrosion was documented exclusively or additionally at the top of the stiffener, SC was set equal to the web depth (d_w). Based on inspection report observations, holes could be found both at top and bottom part of the stiffeners. This behavior was captured by defining two-hole patterns for stiffener deterioration, presented in Tables 2.23 and 2.24.

Table 2.22: Stiffener hole pattern HB for C1 and C2 configurations

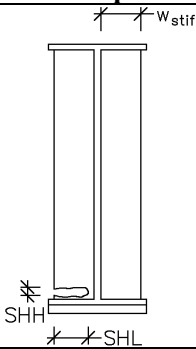

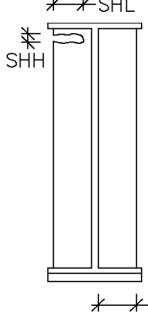
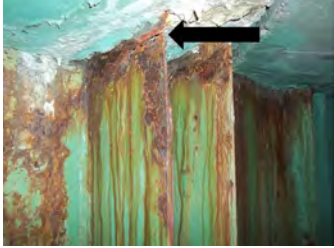
Pattern	Hole shape	Example from an inspection report
HB		 <p>Adopted from W-44-063-1LA-DOT-NBI (District 5, City of Worcester)</p>
<p>Short description: HB is a case where a hole appears at the lower part of the stiffener. HH is the height of the hole, and HL is the length of the hole. HH is expressed with respect to web depth (d_w) and HL normalized to stiffener width (w_{stif}). The photograph on the right shows a typical case of HB.</p>		

Table 2.23: Stiffener hole pattern HT for C1 and C2 configurations

Pattern	Hole shape	Example from an inspection report
HT		 <p data-bbox="899 527 1377 590">Adopted from S-35-013-3YB-DOT-NBI (District 5, Town of Swansea)</p>
<p>Short description: HT is a case where a hole appears at the top part of the stiffener. HH is the height of the hole, and HL is the length of the hole. HH is normalized to web depth (d_w) and HL to stiffener width (w_{stif}). The photograph on the right shows a typical case of HT.</p>		

2.2.3 Summary Spreadsheet Implementation

During the previous stage, the most common topologies were identified and parameters that allowed to describe their characteristics (dimension and section loss) were also introduced. The ultimate goal of this work was to explore the bounds of these parameters by retrieving data from the inspection reports. The goal of this stage was to provide a summary sheet that would standardize the data acquisition methodology, facilitating the whole process. The sheet was oriented to summarize the important information for a beam end by transforming and quantifying information provided in sketches, photos, or text description to a format in compliance with the previously defined patterns.

A summary sheet developed by the researchers in a previous research work (14), targeted to explore the corrosion characteristics of unstiffened beam ends, constituted the base for the current task. The existing sheet was modified to account for both the newly defined beam end configurations (C1, C2) as well as stiffener corrosion data. On the other hand, information relevant to flange corrosion was excluded from the updated sheet version, as the upcoming numerical analysis focuses on web and stiffener deterioration. Thus, this decision aimed to increase the efficiency and the productivity during the data acquisition phase.

The organization of the sheet remained the same, with its top including the basic identification information of the viaduct with data for the name, area, and year of construction (Fig. 2.6). Below that part, each corroded beam was described by a separate column. By describing each corroded beam with a column, each unique beam end case was taken into account.

	A	B	C	D	E	F	G	H	I
1	Identification	columns:	5	Sup. Conc	5				
2	Bridge:	N-06-037 3NF	Area:	New Bedford	Construction:	1969	Steel:		
3	Beam ID (Insp. report):	Beam 7	Beam 8	Beam 12 W1	B12 EF				
4	Beam configuration	C1	C1	C1	C2				
5	a(N)				100%				
6	c(N)	150%	150%	150%	150%				
7	Beam type	Welded	Welded	Welded	Welded	same_end			
8	Web cor. Type:	W5	W5	W5	W5	0			

Figure 2.6: Bridge identification and general information at top of spreadsheet

The first part of each column (Part A, lines 4–7 in Fig. 2.7) provides information regarding the beam end configuration and the beam type. Then, in Part B (lines 8–17), the web corrosion shape is described using one of the five general corrosion patterns defined for each one of the two configurations (C1, C2). Based on the chosen deterioration pattern, the corresponding dimensions were normalized to the scalar parameters defined in each case. For instance, for a beam end with two bearing stiffeners, CL1 is expressed with respect to the web depth (d_w) for the W2 pattern, while the W4 pattern is expressed with respect to α , which denotes the distance between the stiffeners. The section loss is also recorded.

	A	B	C	D	E	F	G	H	I
1	Identification		columns:	3	Sup. Conc	5			
2	Bridge:	N-06-037 3NF	Assess	New Bedfo	Construction:		1969	Steel:	
3	Beam ID (Insp. report):		Beam 7	Beam 8	Beam 12 W	B12 EF			
4	Beam configuration		C1	C1	C1	C2			
5	a(N)		A			100%			
6	c(N)		150%	150%	150%	150%			
7	Beam type		Welded	Welded	Welded	Welded	same_end		
8	Web cor. Type:		W5	W5	W5	W5	0		
9	CL1(dw):		20%	36%	20%				
10	CL2(dw):								
11	CL3(a):								
12	CH1(dw):		B	100%	100%	16%			
13	CH2(dw):		4%	1%	1%	100%			
14	CH3(dw):								
15	Max thickness loss (no holes)		75%	75%	75%	75%			
16	Min. thickness loss:		0%	0%	0%	0%			
17	Signs of buckling:		No	No	No	No			
18	Web Hole pattern:		H1	No	No	H3	H4		
19	HL(%o or d):		C			80%	30%		
20	HH(%dw):		3.0%			1%	4%		
21	b(dw)								
22	Stiffeners Corrossion		D	Yes	Yes	Yes	Both	S2	
23	SC1		16%	3%	3%	0%			
24	SC2					0%	0%		
25	Thickness loss Stif. 1		80%	70%	70%	0%			
26	Thickness loss Stif. 2					0%	0%		
27	Stiffener hole 1:		E	Yes	No	No	Yes		
28	SHL1		43%			100%			
29	SHH1		7%			12%			
30	Stiffener hole 2:					Yes	Yes		
31	SHL2					100%	100%		
32	SHH2					12%	4%		
33	Support type:								
34	Bearing length (%dw):		14.00%	14.00%	14.00%	14.00%			
35	B(dw)		0%	0%	0%	0%			
36	Bearing corrosion:		No	No	No	No			
37	Bearing deformation:		No	No	No	No			
38	Previous repairs:		No	No	No	No			

Figure 2.7: Summary spreadsheet with designated shadowed areas A–F

In Part C (lines 18–21, Fig. 2.7), if a web hole existed, it was classified according to the hole patterns for each configuration. In case its dimensions could be retrieved, they were recorded following the same approach previously described for the corrosion topology dimensions.

Having described the web conditions, Parts D and E are dedicated to stiffener corrosion. In detail, if deterioration was reported for C2 configuration, the cell in line 22, Fig. 2.7, was set to “S1,” “S2,” or “Both,” to describe corrosion at the inner, the outer, or both bearing

stiffeners, respectively. For C1 configuration with a unique stiffener, the option “Yes” stated deterioration existence, and data were recorded at cells dedicated to the inner stiffener (S1). The same procedure was followed to report stiffener holes at S1 (lines 27–29, Fig. 2.7) and at S2 (lines 302, Fig. 2.7). Finally, in Part F, the condition and metrics of the bearing were described, if any information was available.

The way that the summary sheet has been set up limits the web hole input to one pattern per column, as well as to corrosion data for up to two stiffeners. In order to account for web hole combinations (e.g., H1+H2) or for additional stiffeners corrosion data (from the other web face), the adjacent column was utilized and the beam end was set as “same_end.”

3.0 Experimental Work Methodology

This section addresses two longstanding gaps in the existing literature of the aging bridges field. First, there was a lack of experiments that accounted for corroded stiffeners. Most studies intentionally focused on the panel shear failure by accounting for strong bearing stiffeners without corrosion. However, findings emerging from the observation of inspection reports (Sections 2 and 5 in this report) indicated that stiffeners most often undergo severe section loss due to corrosion. The second gap arises from the way that researchers simulated the corrosion-induced damage. Except for the work of (5) on railway bridges, most of the available studies experimentally resembled the corrosion effect by uniformly reducing the thickness along the girders' components. However, given the nonuniformity of corrosion in the field, this approach might not be able to capture failure mechanisms related to the variability at the intense of the corrosion phenomenon.

In this study, field corroded specimens were tested in the laboratory to study the effect of section loss on a fully and a partially stiffened girder. The beam selection process, design, testing rig, and instrumentation configuration are described in this section. The mechanical model of each beam, in terms of geometry, corrosion topology, boundary, and loading conditions, is also described.

3.1 Experimental Preparation

3.1.1 Beam Selection and Shipment to UMass Testing Facilities

The researchers were oriented toward using naturally deteriorated specimens; however, the materialization period of the current study was not aligned with a bridge rehabilitation project in the Commonwealth of Massachusetts employing plate girders. Consequently, naturally deteriorated rolled girders were used, and stiffeners were welded prior to testing.

At the time this research began, a bridge rehabilitation project was in progress in the Commonwealth of Massachusetts. Specifically, a three-span bridge (O-03-009) in the town of Orange was under demolition. The structure, which carried Holtshire Road over Millers River, was built in 1937, and its design contained continuous 24CB120 unstiffened rolled girders. The two piers divided the total length into three equal spans of 60 ft., 8 in. long each. The bridge was eventually deconstructed due to the critical condition of the deck, which contained a number of large holes throughout its surface (Fig. 3.1a). According to the inspection reports, the deck underside had widespread leakages, which potentially led to widespread surface rust in the girders (Fig. 3.1b).

Before transporting the beams, it was decided the best practice would be to cut the beams in half. The advantage of this was twofold. First, it provided ease of transport. Second, it would allow both segments to be in compliance with laboratory length restrictions. In total, 11 segments were shipped to the Brack Structural Testing Laboratory at the University of Massachusetts, Amherst.



Figure 3.1: a) Hole through the deck and b) map cracking with heavy efflorescence at O-03-009 bridge (adopted from O03009-0TW-MUN-NBI)

Delivery 1

On January 9, 2020, four beam segments were delivered to the Brack Structural Testing Laboratory at the University of Massachusetts. The research team coordinated with UMass Construction Services to unload and place the beams into the backyard of the laboratory (Fig. 3.2).

Delivery 2

On January 14, 2020, seven additional beam segments from the Orange bridge were delivered.



Figure 3.2: Delivery, unloading, and storage of first set of corroded beams

3.1.2 Specimens Fabrication

Based on the conditions of the delivered beams, the evaluation of their testable quality was performed. All the decommissioned girders had exhibited corrosion damage, characterized by localized areas of moderate section loss above the supports. Finally, out of the 11 beam segments, 2 were considered that had experienced enough section loss to be considered promising for results that would be representative of the load-carrying capacities of damaged beams. The relatively good condition and the absence of corrosion-induced holes in the girders was reflected by the superstructure rating that had been classified as “fair condition” at the last available inspection report, prior to demolition.

To avoid failure loads that could exceed the available load capacity of the testing rig, the researchers were oriented toward fully stiffening the girder that visual observation indicated as the most damaged one. Consequently, partial stiffeners were welded to the second specimen. Fig. 3.3 depicts the as-received condition of the girders for the fully (Fig. 3.3a) and the partially (Fig. 3.3b) stiffened specimens, hereafter referred to as Specimens A and B, respectively. In both cases, the riveted plates located above the support were removed before welding.

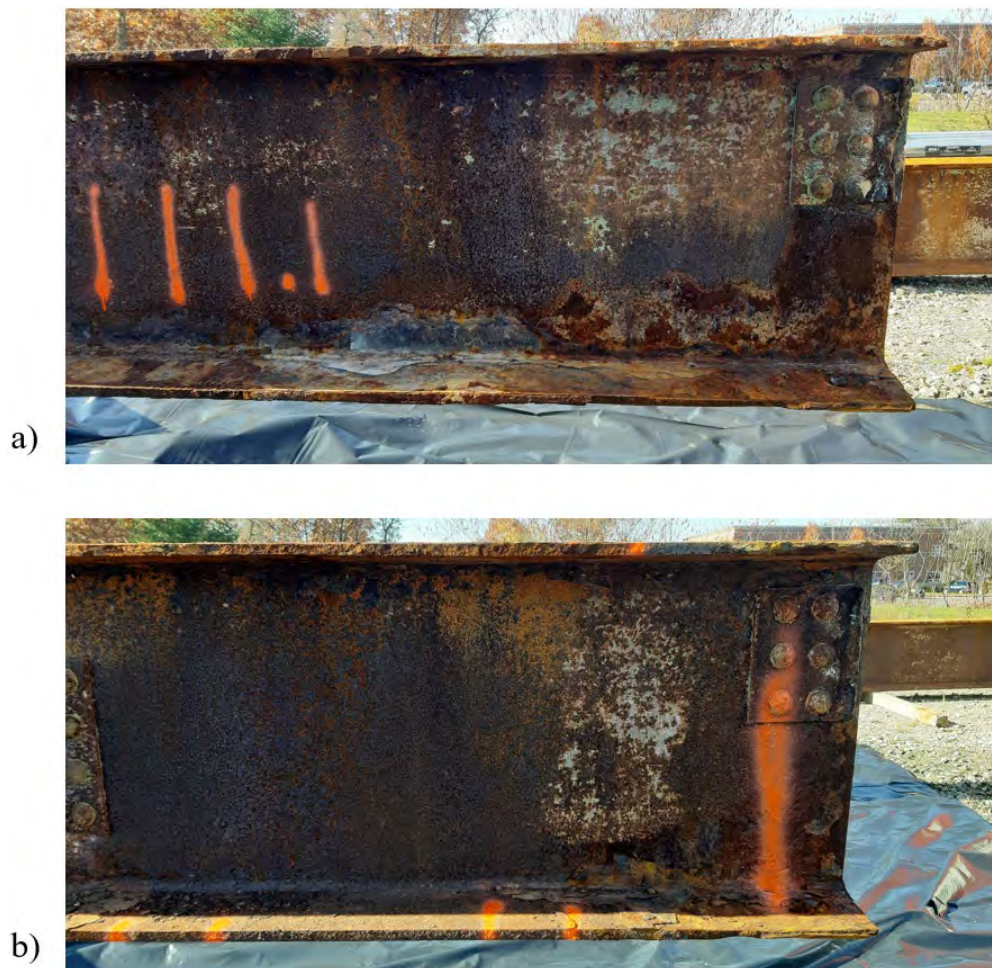


Figure 3.3: As-received condition for Specimens A and B

The resulting expenses were fully covered by MassDOT, while the weldability test, the surface cleaning, and the plate welding took place between November 2, 2020, and December 4, 2020.

The fabrication drawings for each specimen are presented in Section 3.2.

3.1.3 Design of Experimental Configuration

The laboratory setup was designed to generate high shear near the corroded end. The girder was tested under a simply supported condition (Fig. 3.4). An expansion bridge bearing obtained from another demolished bridge, provided by Gill Engineering, was placed below the corroded end. This 7-inch-long bearing consisted of two curved plates accommodating rotational and translational displacements. The far end of the beam was supported on a 12-inch-long rectangular steel plate. The top flange was laterally supported to prevent lateral-torsional buckling from becoming the governing failure mode; in total, four pairs of lateral braces were placed along the length of the specimen.

Loading was applied using two 200 kips hydraulic jacks with top cups able to accommodate rotations along 360°, located under the bearing of the tested end of the specimen. The jacks applied an upward vertical force, simulating the reaction at the tested end. The force from each jack acted on a spreader beam that supported the bridge bearing on its top flange. A crossbeam anchored to the laboratory strong floor by means of 1.8-inch threaded rods was used to hold the specimen down on a section located approximately 4 feet from the loaded end. The hold-down beam was fabricated using two separate W sections, welded together to allow passage of a threaded rod that was anchored to the strong floor. For the purpose of this study, the beam end closer to the applied load was referred to as the *tested end*, while the other end was referred to as the *far end*.

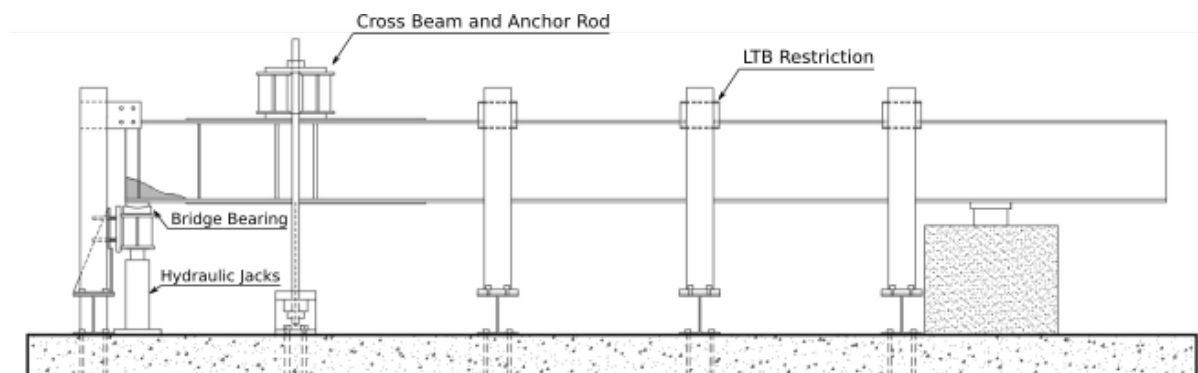


Figure 3.4: Experimental rig

3.1.4 Instrumentation Configuration

All specimens were instrumented to record loads and deformations (Fig. 3.5). In order to measure the applied load, two 200 kips load cells, manufactured by Omega, were placed at the anchorage point of the threaded rods. A third compression load cell, with 100 kips capacity, was installed beneath the intact end to record the bearing reaction force. A TJE

pressure transducer, by Honeywell, was installed to monitor pressure of the hydraulic fluid in the hose, downstream of the hydraulic pump.

Ten displacement potentiometers were used to record vertical and lateral deflections. Two spring-type potentiometers by Celesco were used to measure the maximum vertical beam deflection close to the load application area, as well as below the crossbeam. These potentiometers had a 10-inch measuring capacity and were attached on hooks installed at the bottom flange. Eight Novotechnik rod-type potentiometers were used to measure the out-of-plane displacements at the corroded end. These potentiometers were installed on a frame, forming an arrangement of two columns and four rows. This configuration was chosen in order to record two different sets of out-of-plane displacements taken over the height of the web. The two columns of instruments were placed at the inner side of the bearing stiffeners for both specimens. The rod-type potentiometers had a measuring capacity of 4 inches.

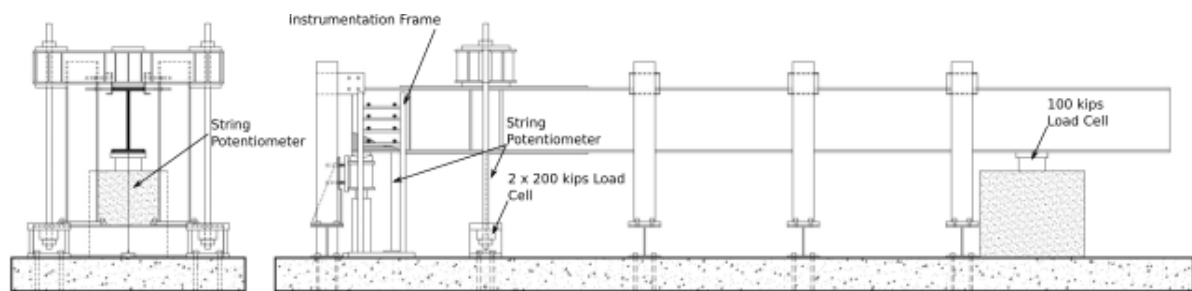


Figure 3.5: Side and front view of instrumentation configuration

A list of instrumentation equipment used in the experiment is as follows.

- Horizontal Potentiometer: 6 x TR-0100 by Novotechnik
- Vertical Potentiometer: 2 x PT-101-10A by Celesco
- Load cells: 2 x LC8400 by Omega Engineering Inc.
- Pressure Transducer: TJE by Honeywell

3.2 Specimens Geometry

3.2.1 Specimen A

Specimen A was designed to study the failure mechanism of beams with stiffened ends based on a 299-inch-long rolled 24CB120 with moderate to locally severe end corrosion. A detailed study of the available inspection reports indicated that a typical failure of girders with corroded ends included large out-of-plane displacements developed at the web and stiffeners above the support. To prevent flexural strength from governing the failure mode during the test, two 0.5-inch-thick cover plates were welded to the top and bottom flanges along up to 89 inches from the beam end. Moreover, to resemble a deteriorated stiffened beam end, stiffeners with varying dimensions were welded along the specimen, introducing two web panels above the corroded support (Fig. 3.6).

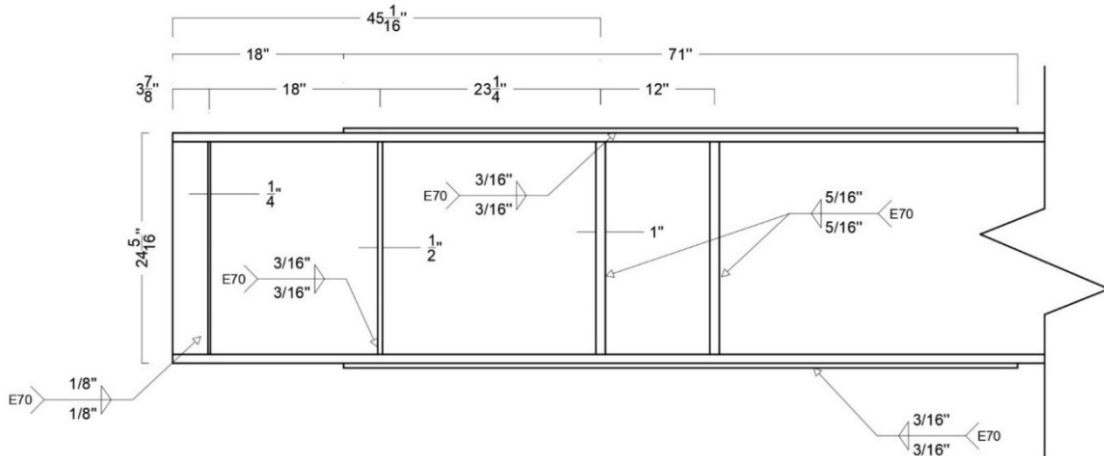


Figure 3.6: Fabrication drawings of Specimen A

To account for the reduced thickness of a corroded end, the bearing stiffener thickness was set equal to 0.25 inches, while the thickness of the adjacent pair was increased to 0.5 inches, corresponding to the dimensions of an intact stiffener. Finally, to avoid yielding due to the high anticipated reaction force at the crossbeam location, two pairs of 1.0-inch-thick stiffeners were provided to locally strengthen the girder.

A photograph of the actual specimen is presented in Fig. 3.7. Observation of the same figure revealed perforations resulting from the removal of the riveted plates along the web. Additional perforations were found at the bottom flange, where anchor rods were passing through to restrict the girder in in-service conditions. Their existence prevented the bearing stiffeners from transferring load to the bottom flange along their whole width.



Figure 3.7: Corroded end of Specimen A

To quantify the remaining material along the deteriorated beam end, the team scanned the beams using a Riegl VZ-2000 laser scanner. Scans were performed from both sides of the specimen, and the acquired point clouds were registered to one unique coordinate system making use of reflective targets placed in the laboratory and on the specimen surface. Following a methodology previously developed by the authors (17), contour maps capturing the remaining material along the web were created and are shown in Fig. 3.8a. A diagonal area with extensive section loss extended above the bearing, which later propagated in parallel to the bottom flange, while initial web deviation was observed at the outer part of the web, with a maximum magnitude of 0.5 inch (Fig. 3.8b).

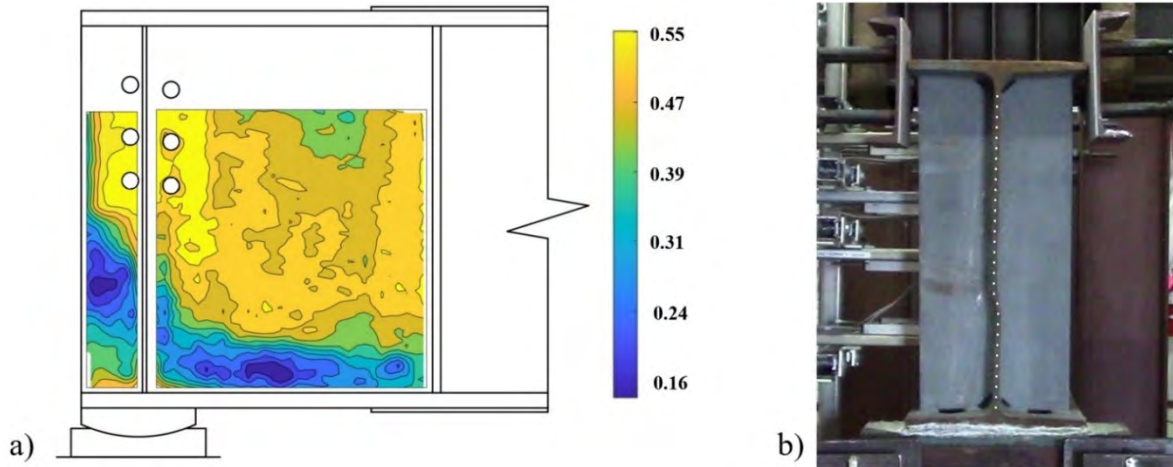


Figure 3.8: a) Contour maps depicting remaining thickness of Specimen A; and b) initial web imperfection for same girder

The exact experimental configuration is illustrated in Fig. 3.9, and the instrumentation configuration in Fig. 3.10.

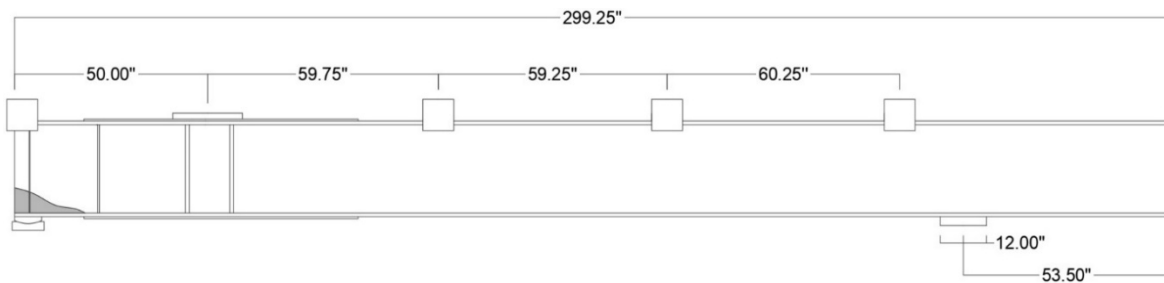


Figure 3.9: Specimen A experimental configuration and dimensions

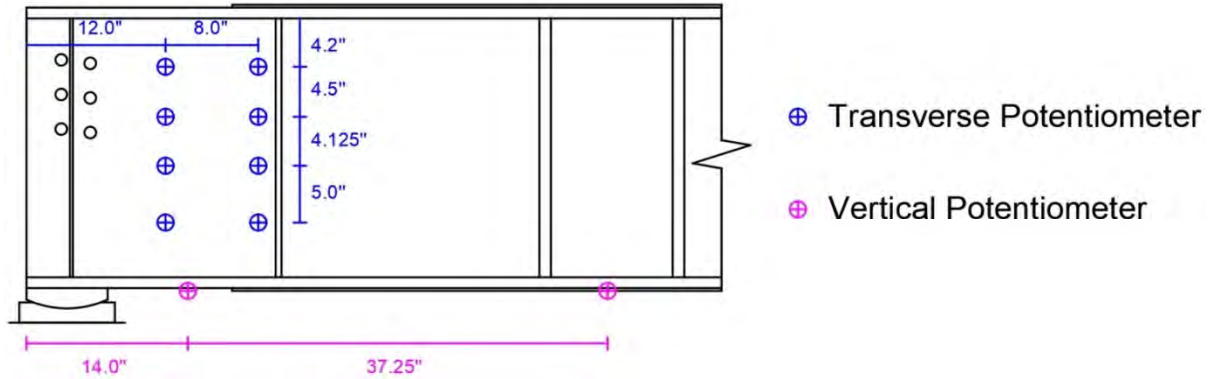


Figure 3.10: Instrumentation configuration of Specimen A

3.2.2 Specimen B

Specimen B was a 301-inch-long rolled 24CB120 with moderate end corrosion, and it was designed to study the failure mechanism of partially stiffened beams. This configuration is commonly found on rolled girders to support steel or concrete diaphragms, and consists of plates that do not transfer load through the top or bottom flange. To resemble in-service partially stiffened girders, a 0.5 in. by 5 in. plate was welded along each web face. In addition, to avoid flexural related failure modes, a set of 0.5-inch-thick cover plates was added along the flanges, increasing the moment capacity close to the crossbeam area. Below the same location, two sets of 1-inch-thick stiffeners were also welded. The exact fabrication drawings are presented in Fig. 3.11.

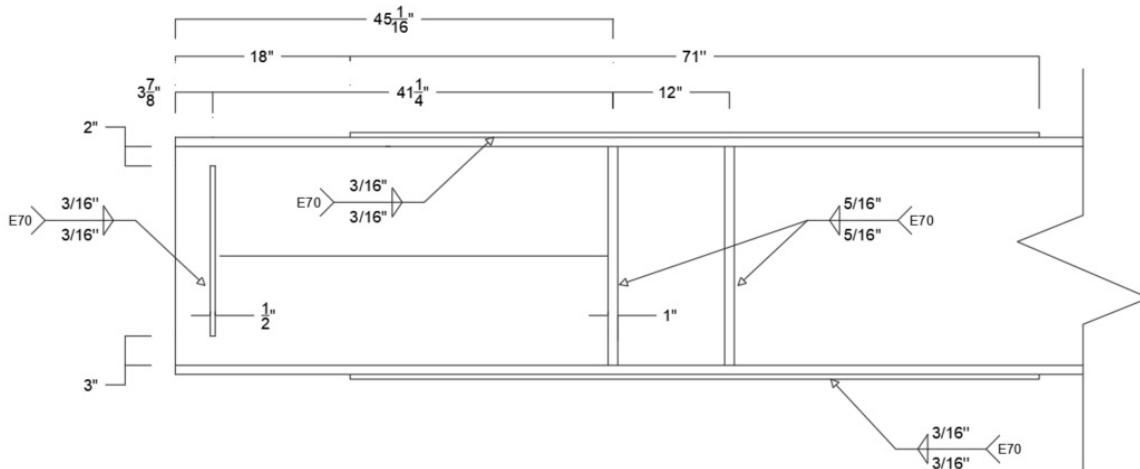


Figure 3.11: Fabrication drawings of Specimen B

A photograph of the actual specimen is presented in Fig. 3.12. Observation of the same figure revealed perforations along both sides of the partial stiffener, resulting from the removal of the riveted plate depicted in Fig. 3.3b. Regarding the support conditions, in order to promote a uniform loading, grout was used to fill the gap between the flange and the support.



Figure 3.12: Corroded end of Specimen B

To quantify the remaining material along Specimen B, the Riegl VZ-2000 laser scanner was used and scans were performed capturing both web faces. After registering the obtained point cloud data to a unique coordinate system, contour maps depicting the remaining material along the tested end were developed and are presented in Fig. 3.13. Overall, the observed corrosion topology is very similar to the deterioration condition of Specimen B, strengthening the findings from (14) that beams belonging to the same bridge exhibit similar corrosion-induced damage, governed by the in-service configuration of the support area.

For the two specimens examined in the framework of this study (Fig. 3.8 and 3.13), the existence of the riveted plates above the supports prevented the water flow from deteriorating the web below (yellow areas surrounding the upper part of the bearing stiffeners). Furthermore, for both cases, section loss with progressively reduced height was observed directly below this region, which eventually propagated in parallel to the bottom flange. For Specimen B, the region with the minimum remaining thickness (around 50% of the intact web thickness) was located approximately 4 inches beyond the bearing. Finally, visual observation as well as post-processing of the point cloud data did not reveal significant web deviation from straightness.

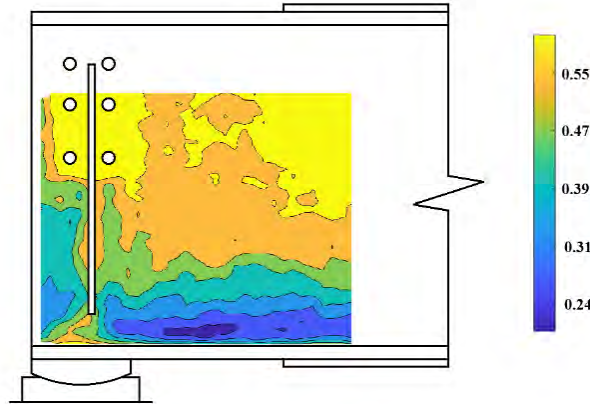


Figure 3.13: Contour maps of remaining thickness along tested end of Specimen B

The exact experimental and instrumentation configurations are illustrated in Figs. 3.14 and 3.15, respectively.

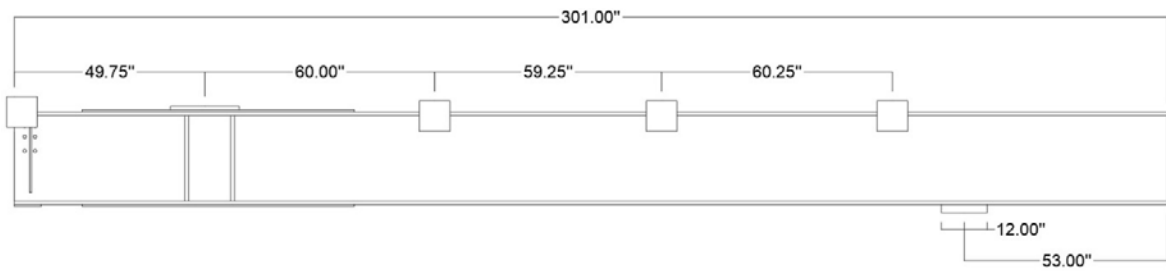


Figure 3.14: Specimen B experimental configuration and dimensions

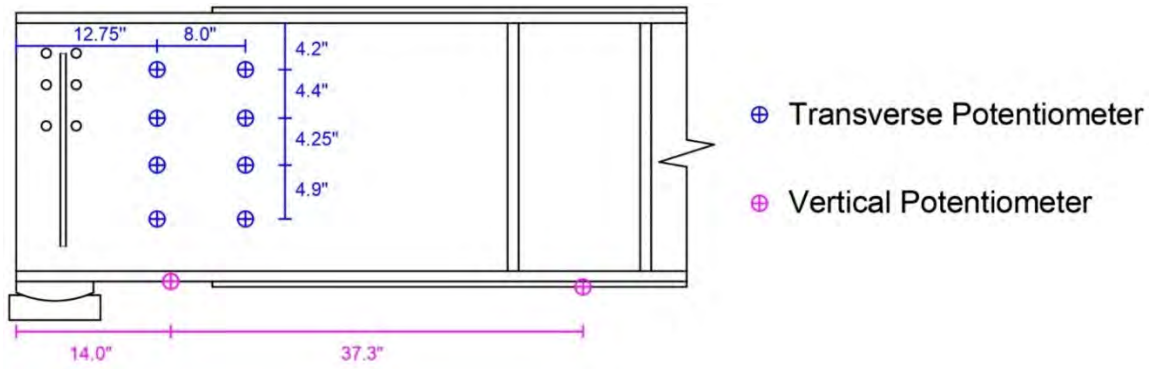


Figure 3.15: Instrumentation configuration at tested end of Specimen B

This page left blank intentionally.

4.0 Analytical Work Methodology

The goal of this phase was to develop a high-fidelity numerical model capable of predicting the bearing capacity of composite plate girders. Combining the corrosion patterns with numerical modeling, an extensive parametric analysis was performed.

4.1 Computational Model Validation

The presented numerical model was being developed simultaneously with the evolution of the experimental work. By comparison of the numerical and experimental output obtained from Specimen A, the model was considered to fulfill the requirements for accuracy and efficiency. In this section, the modeling assumptions regarding the mechanical problem formulation in terms of its geometry, boundary, loading conditions, material properties, and geometric imperfections are described in detail. Particular attention is paid to the procedure followed to represent the natural nonuniform thickness reduction profile.

4.1.1 Mechanical Model

Beam Geometry

Specimen A was simulated. Its geometry and defining features were described in Section 3.

Section Loss

The project team employed a methodology previously developed by the authors (17) to enable the integration of point cloud data into a three-dimensional geometrical model discretized with finite elements. The team utilized the thickness determined using 3D laser scanning to capture the corrosion characteristics of the specimen in the finite elements model (FEM). In detail, 10 levels of remaining material thickness between the minimum and the maximum recordings were derived (Fig. 3.8a), and a MATLAB script was employed to extract the coordinates of the points that constituted the contour lines. Subsequently, a script in Python was used to partition the web face of the simulated geometry by connecting the points on these lines. Having defined the deterioration boundaries, each of the 10 thickness values determined using 3D laser scanning was assigned to the corresponding areas.

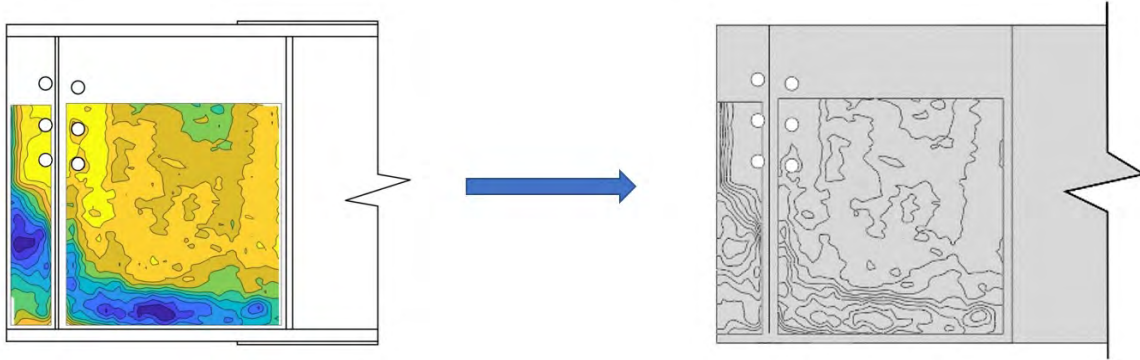


Figure 4.1: Section loss simulation by partitioning web region and assigning thickness levels derived by post-processing point cloud data

Material Properties

The material properties for the specimen were derived through tensile testing performed in a previous study by the researchers (14). Stress-strain curves (Fig. 4.2a) were obtained using coupons extracted from the web and the flanges. The discrepancy observed in the yield and ultimate stresses of the steel at the web and flange could be attributed to the residual stresses that commonly develop for this type of beam at the time of manufacturing. The stress-strain curves for the top and bottom flange were similar, as would be expected. For the stiffeners, a bilinear constitutive law with hardening based on experimental data provided by the supplier is presented in Fig. 4.2b.

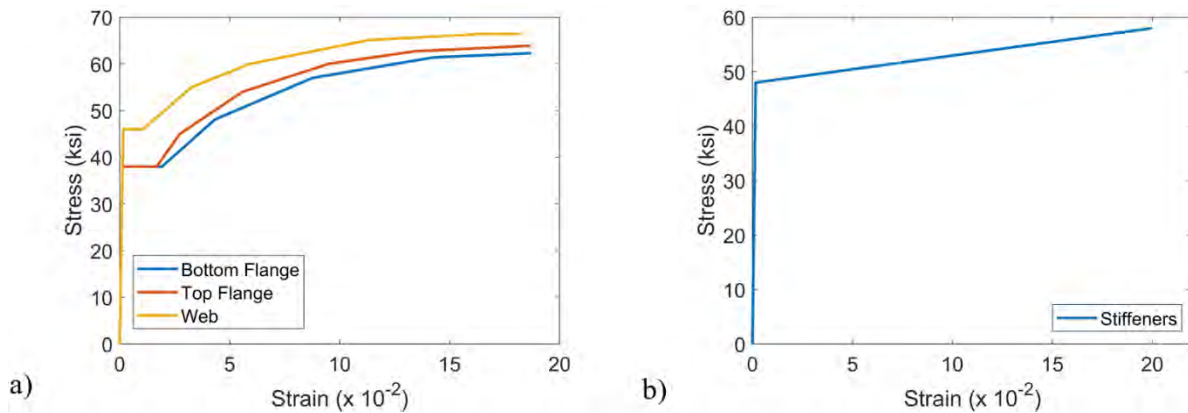


Figure 4.2: a) Measured stress-strain properties of specimen for finite element simulation obtained from (14); b) stress-strain properties for welded parts, according to data provided by manufacturer

Boundary and Loading Conditions

Both boundary and loading conditions simulated the exact experimental configuration. The bottom flange of the girder rested on two steel bearing plates, which are considered hinges. Similar to the experimental configuration, the load was applied to the plate below the tested end. The out-of-plane displacement was not allowed at the locations of the LTB restrictions.

The test setup configuration included a stiff crossbeam that held the specimen down by anchoring it to the strong floor using two large-diameter threaded rods. To capture the

flexibility of this restraint system, the experimentally measured displacements of the crossbeam were used to determine the stiffness of the hold-down system (135 kN/mm). Fig. 4.4 illustrates how the flexibility of the hold down system was introduced into the FEM. The stiffness determined for the hold-down system was taken into account by introducing a spring, with its bottom end tied to the top flange of the model.

Geometric Imperfection

Having described the exact dimensions, thickness reduction, material properties, boundary, and loading conditions, the last aspect of the mechanical problem formulation is the applied geometric imperfection.

For any plate or shell buckling problem, it is well known that the structure will suffer from geometric imperfections. Overlooking imperfections can be catastrophic when predicting the capacity of a structure. For the mechanical problem of the deteriorated steel beam ends, initial geometric imperfections were needed for the proper formulation of the problem. In many similar problems, scaled eigenmode shapes are commonly used as the initial geometric shapes of the shell or plate.

For intact beams, initial imperfections obtained during the rolled steel manufacturing process are negligible. However, corrosion does not symmetrically reduce the thickness along web sides, resulting in geometric nonlinearities that are able to trigger an instability. Thus, extreme thickness reduction usually results in instability phenomena, making deteriorated webs slender, buckling-prone members.

Imperfections were introduced in the model based on the eigenmode shapes. The model was initially solved using an eigenvalue buckling analysis algorithm. Then the eigenmode that better matched the web shape of the actual beam was introduced as an initial geometric imperfection for the quasi-static analysis, scaled to the measured maximum lateral displacement of the web.

For Specimen A, the maximum initial web lateral displacement was observed at mid-height and equalled 0.5 inches (Fig. 4.3a). The selected eigenmode managed to represent satisfactorily the initial out-of-plane web displacement, as shown in Fig. 4.3b.

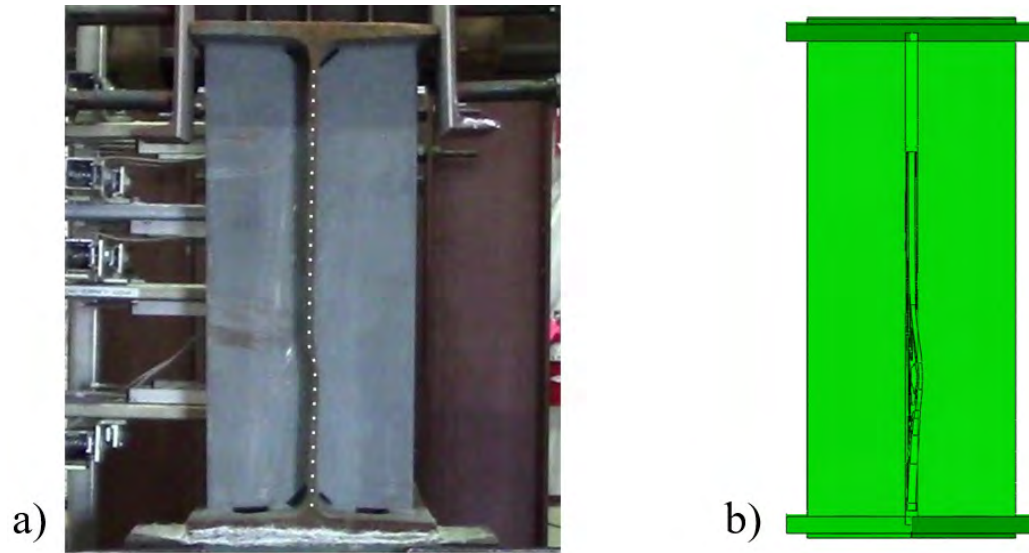


Figure 4.3: a) Front view of Specimen A; b) initial geometric imperfection as imported to FEM

4.1.2 Finite Element Procedures

The girder was simulated with a mid-surface shell model. Both the web and flange thicknesses were assigned to the corresponding shell elements. The remaining thickness was simulated by assigning a uniform reduced thickness at the elements located in the deteriorated area. Holes were simulated by removing elements.

The computational model was developed employing the general-purpose finite element software ABAQUS (19). Based on sensitivity studies presented in (14), the four-node linear element S4R was chosen to model the girder, using two different sizes depending on location. A dense mesh with element size 0.5 inch was used to discretize the corroded end. Moreover, to ensure computational efficiency, the element size was progressively increased up to 3 inches at midspan. At both bearings, rotation was allowed along the axis vertical to the web plane, by applying the tie constraint between the simulated bearing plates and reference points introduced to the center of rotation of each bearing. The interaction between the bottom flange and the bearing plates was idealized by introducing contact. The applied load was simulated as a concentrated force applied to the reference point below the tested end (Fig. 4.4).

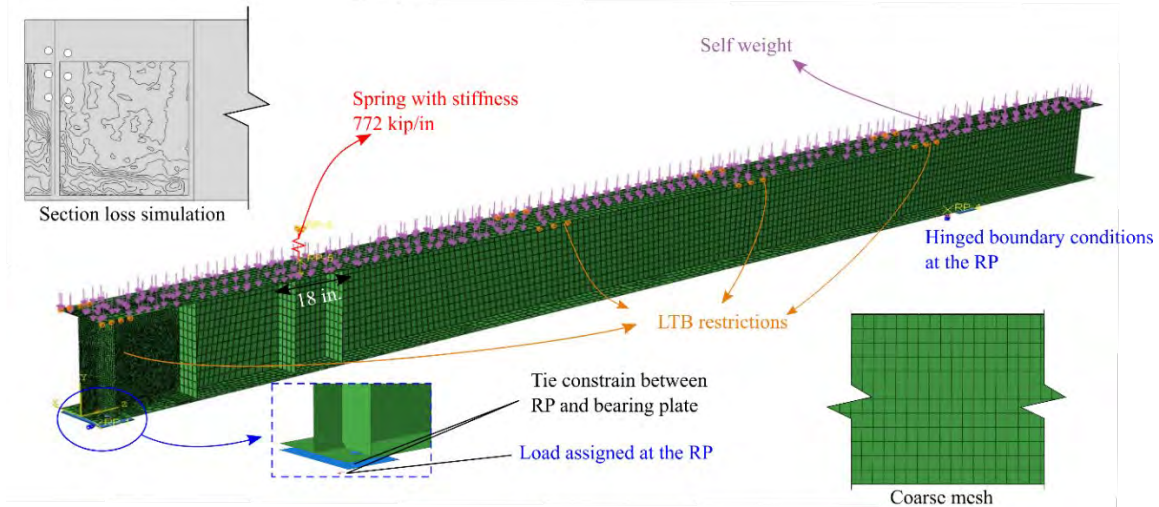


Figure 4.4: Developed FEM to simulate experimental procedure of Specimen A.

4.2 Composite Action

The ability of the developed FEM to capture the failure mode and load of stiffened girders with corroded ends provided confidence in its accuracy. However, to better capture in-service behavior of beams with corroded ends, a sensitivity analysis was conducted by including the effect of a composite concrete deck in the FEM. Construction drawings from the time of construction describe most bridges as being built compositely with the deck by including shear studs welded to the top flange and embedded in the concrete deck.

The composite behavior was incorporated in the FEM by introducing shear studs and a concrete deck simulated with a multipoint constraint (MPC) and shell elements with 7 Gauss quadrature integration points, respectively. Similar modeling assumptions have been validated by (20), who analyzed 3-point bending in two laboratory tests employing simply supported composite girders conducted by (21). Both studies were carried out until the crushing of the concrete slabs. Deck was modeled assuming linear-elastic material properties, because the loading conditions of the current study were intended to generate high shear close to the corroded support. Consequently, concrete failure related to the compression of the slab due to high moment was not expected to occur.

Under these assumptions, and to validate the efficiency of the computational model to capture the composite action of steel girders, Specimen POS2 (Fig. 4.5), tested by (21), was simulated (Fig. 4.6). The girder was constructed using 70 ksi steel, and 60 pairs of studs 0.75 inch in diameter and 4.5 inches high were used. The girder was tested as simply supported, with the load being applied at midspan. To prevent out-of-plane displacement, lateral braces were placed 3 feet to either side of the midspan.

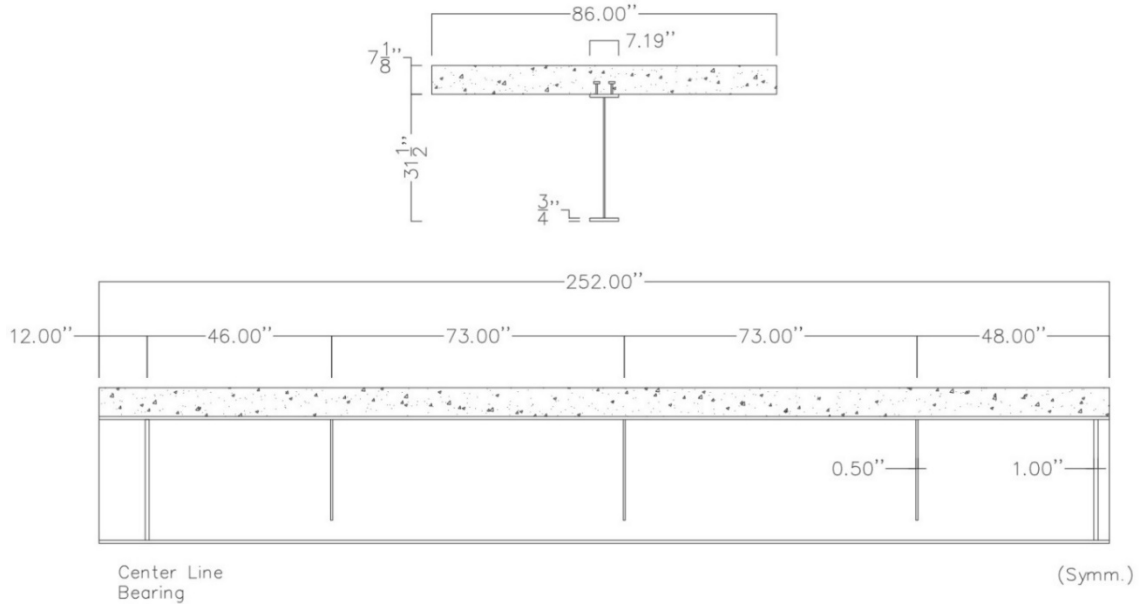


Figure 4.5: Geometry of POS2 specimen tested by (21)

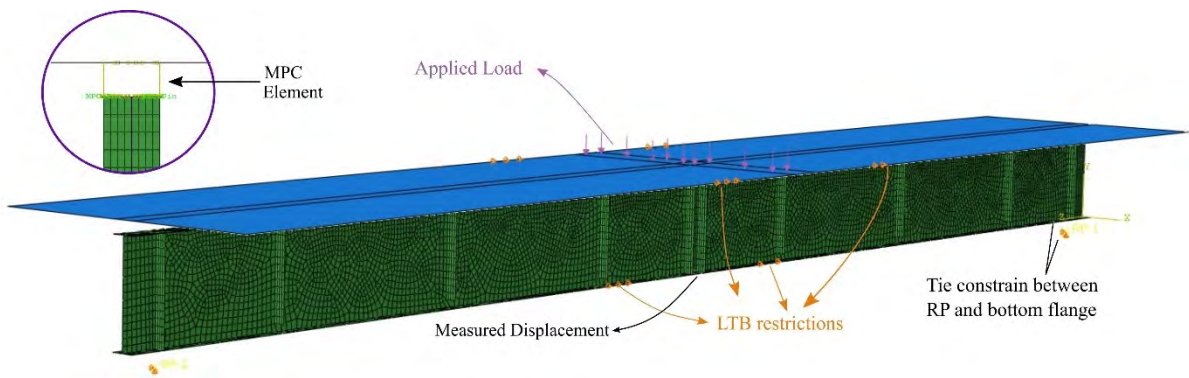


Figure 4.6: FEM developed to simulate experimental procedure of POS2 specimen

4.3 Parametric Analysis Setup

The researchers aimed to conduct computational parametric analyses to investigate the capacity and the collapse mechanism of plate girders with corroded ends. Different combinations of beams and corrosion topologies were used to develop an extensive series of computational models which, in turn, were analyzed to provide the failure mode of the deteriorated beam ends along with the failure load.

4.3.1 Corrosion Scenarios

During the first part of this research project, the most common beam end corrosion topologies were identified and quantified. Initially, based on inspection reports of bridges that had experienced this phenomenon, five general corrosion cases were created for girders

with a pair of bearing stiffeners, and 120 unique deteriorated beam ends were accurately described making use of these preliminary defined patterns. By post processing the recorded data, the final most common corrosion scenarios were quantified (see Sections 1 and 5).

In this study, the web corrosion patterns W1, W2, and W3, in combination with the stiffener corrosion pattern S1 in Fig. 4.7, were employed to study the deterioration effect to the bearing capacity of stiffened girders. The metrics of the examined scenarios are shown in Table 4.1. The examined web scenarios were selected because, according to the final corrosion shapes presented in Section 5, all other scenarios are subsets of the extreme geometrical bounds of the analyzed scenarios. Parametric analysis was initiated to study the effect of geometric imperfection and deterioration dimensions to capacity, under the assumption of uniform thickness reduction along the corroded area. The advantage of this assumption was twofold. First, it followed the current procedures for strength evaluation of corroded girders. Second, it correlated to the usually limited thickness measurements performed by MassDOT’s inspection engineers.

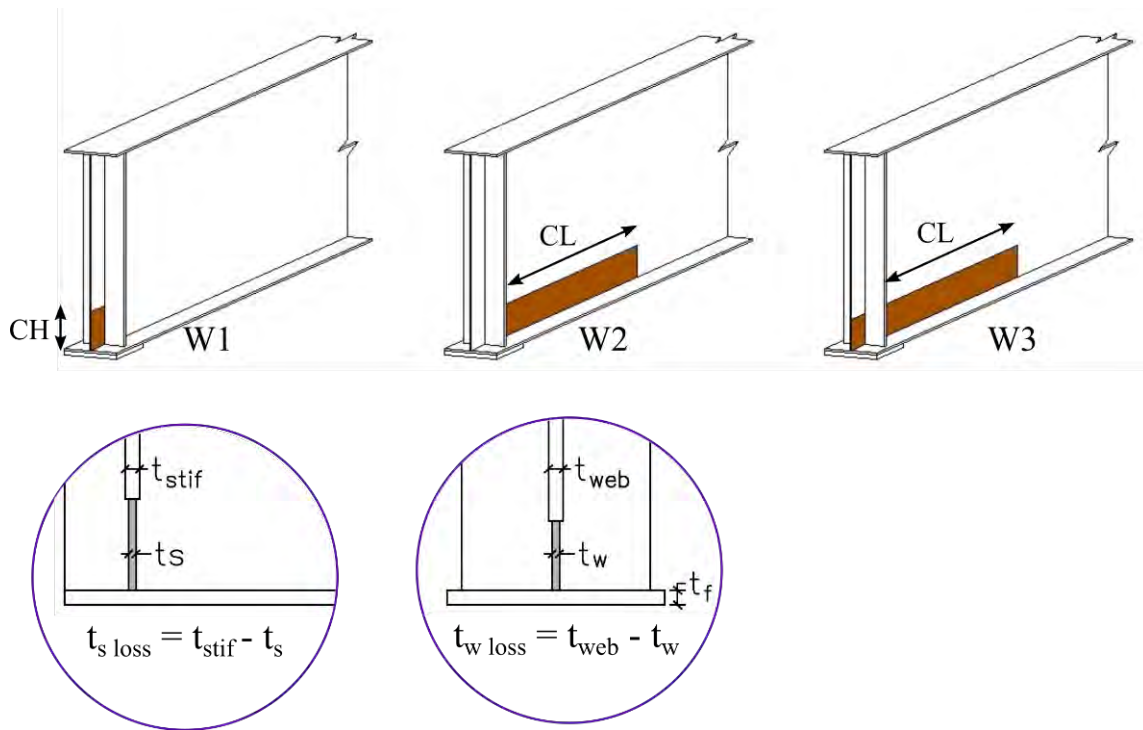


Figure 4.7: Shape and location of examined deterioration topologies

Table 4.1: Metrics of examined scenarios

Web						
No.	Patt.	C _H (d)	C _L (d)	t _{loss} /t _{web}	C _{HS}	t _{sloss} /t _{stif}
1	W1	0–20%	-	0–10%, 50–90%	-	-
2	W1	100%	-	30–80%	-	-
3	W2	0–20%	0-130%	20–80%	-	-
4	W3	0–16%	0-85%	40–80%	-	-
Stiffener						
5	S1	-	-	-	0–25%, 100%	10–90%

4.3.2 Beam Geometries

By careful observation of the construction drawings provided by MassDOT, it was observed that most of the examined bridges were built between 1960 and 1970 (Fig. 4.8). The bridge design standards that were active at that time (22) dictated that the first two stiffener spaces at the ends of the beams were placed at intervals twice as dense as the spacing of the panels at the remaining length, and no wider than half of the depth. The stiffener characteristics, the cover plate, and the web and flange dimensions were mined from construction drawings of structurally deficient bridges in the Commonwealth of Massachusetts.

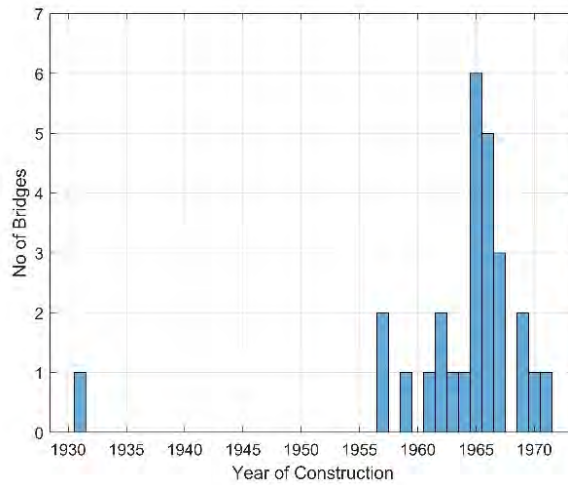


Figure 4.8: Year of construction distribution for bridges studied

In addition, according to the established technique at that time, the plate girders were typically composite. Consequently, an 86 in. x 8.5 in. concrete deck was explicitly included in the model, interacting with 32 pairs of uniformly shear studs along the top flange. The corrosion scenarios were projected on a girder spanning approximately 52 feet (labeled as Geometry I in Fig. 4.10).

4.3.3 Material Properties

The phenomenon of beam end corrosion is observed on structures that have been designed and constructed typically between 1930 and 1970 (Fig. 4.8). According to the available inspection reports and drawings, 36 ksi steel was mainly reported. Moreover, for the same era, (23) reported a mean yield stress of 38.1 ksi steel for the ASTM A36 steel, based on 80 tested coupons. Taken altogether, a bilinear elastoplastic constitutive model with hardening was used, with 36 and 58 ksi yield and ultimate stress, respectively. The material was modeled as isotropic, with Young Modulus equal to 29,000 ksi and a Poisson's ratio equal to 0.27.

For the concrete deck, a linear elastic material was assumed with Young Modulus equal to 3,800 ksi and a Poisson's ratio equal to 0.2.

4.3.4 Boundary Conditions

The research group aimed to study in detail all aspects of the computational framework needed to capture the complicated phenomenon of failure of deteriorated steel beam ends. This model would have to describe the actual behavior of single span plate girders. Thus, the boundary conditions would have to reflect the transitional and rotational restriction applied to the girder due to the slab and supports.

Even though the composite action was integrated in the model by explicitly including an 86-inch-wide concrete deck, the contribution of the whole structure was considered by restraining the out-of-plane displacements of the deck (perpendicular to the beam web and parallel to the width of the flange). In addition, its rotation along the beam's longitudinal axis was also constrained.

A critical aspect of the boundary conditions in the mechanical model studied here concerned the support conditions of the bottom flange of the beam on the bearing plate. In general, both the expansion and the fixed bearings of girders spanning 50 feet or greater are provided with a type of arrangement that allows accommodation of deflections (Fig. 4.9). To incorporate this characteristic in the mechanical model, the plate over which the girder was resting was explicitly included in the model, tied to a reference point introduced as follows. The interaction between the plate and the bottom flange was modeled with hard contact, while roller and pin boundary conditions were applied to the reference point to capture the behavior of the configurations (illustrated in Fig. 4.9a and b, respectively).



Figure 4.9: a) Expansion and b) fixed bearing types commonly found supporting corroded plate girders in Massachusetts

Preliminary analysis demonstrated that between the two bearing configurations, no variation was observed at the failure load of the corroded end. Consequently, roller boundary conditions were applied to the reference point below the end over which the corrosion scenarios were projected.

4.3.5 Loading Conditions

The type of loading was defined based on the load rating procedures in use by MassDOT. According to the draft MassDOT 2020 *Bridge Manual* (24), the rating factor is calculated based on the following equation:

$$LRFR \text{ Rating Factor} = \frac{R_{yield} - DL_{rxn}}{(L + I)_{rxn}} \quad (4.1)$$

Where I is the dynamic load allowance that is applied in addition to the static vehicle load, to account for its dynamic effects. $R_{n,yield}$ denotes the nominal web local yielding capacity, and its formulation is included in the draft MassDOT 2020 *Bridge Manual*, Chapter 7 (24).

Besides the dead load of the beam, the applied dead load (DL) considered the contribution of the deck that the beam was carrying, using tributary areas. Live loads were applied based on the HL-93 load check. The HL-93 consisted of a three-axle truck (HS20), or a design tandem plus the design lane load that was equal to 0.64 kip/ft. The shear loads of the beam in formula (4.1) were calculated using beam theory formulas. According to (24), substituting the corroded web factored resistance, equation (4.1) becomes:

$$R.F. = \frac{(\Phi_b = 1.0)(R_{n,yield}) - (1.25 \times V_{dead \text{ load}} + 1.5 \times V_{wear.surf.})}{1.75 \times g_s \times (V_{Lane \text{ Load}} + (1 + 0.33) \times \max(V_{HS20}, V_{Tandem}))} \quad (4.2)$$

The computation of the shear live load distribution factor (g_s) depends on whether the girder is interior or exterior in the bridge. For the current work, it was decided to follow the process for an interior girder in order to limit the dependence from the bridge geometry.

The physical meaning of the rating factor denotes the multiple of the factored live load in addition to the factored dead one, for how much the beam end is able to withstand prior failure. Based on that, the applied loads of the mechanical model and, later on, of the computational model were in accordance with the load rating procedures and were applied in multiple steps.

During Step 1, the unfactored dead load was applied as a uniform downward pressure on the concrete slab. At Step 2, the factored live loads were applied. The lane load was applied as a uniform downward pressure on the deck. The truck load tire contact areas covered the full flange width on the deck surface and 20 inches longitudinally (Fig. 4.10). In order to force the corroded beam to failure, the magnitude of multiple live loads was applied during Step 2.

The capacity of the beam end was measured by the reaction force at the bearing, when failure occurred.

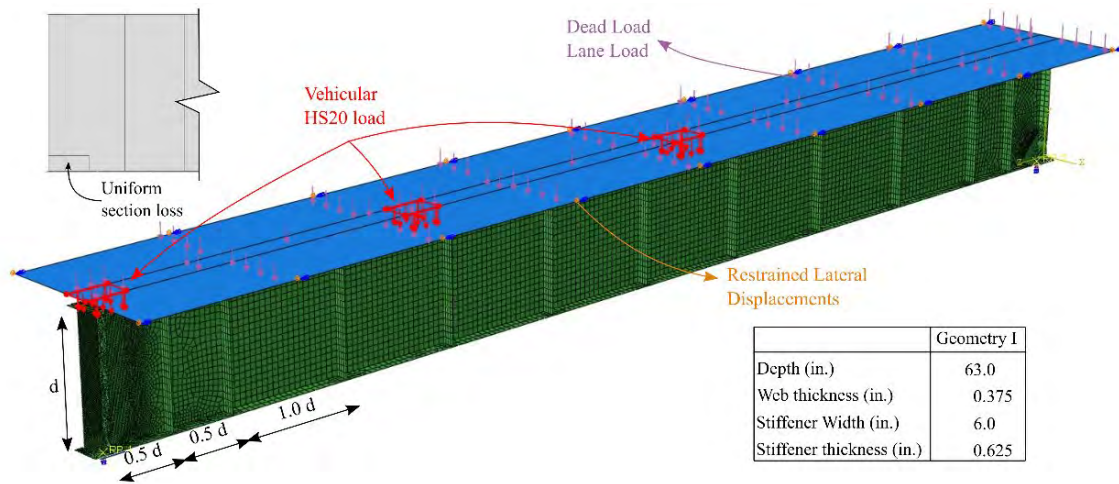


Figure 4.10: Geometry and FEM for girder configurations used for parametric analysis

4.3.6 Geometric Imperfection

For intact plate girders according to modern manufacturing and fabrication techniques, initial imperfections are minimal. However, the researchers had to account for two factors. First, the majority of examined beams were manufactured before 1970. Second, geometric nonlinearities could come from the nonsymmetric thickness reduction along the girder components.

For the problem studied here, geometric imperfections were accounted for in the form of scaled eigenmode shapes. The effect of the preloading imperfection amplitude was extensively examined by analysis performed in the range of 10% to 200% of the intact web thickness.

4.3.7 Programming Implementation

As explained extensively in previous sections of this report, each model was run initially using an eigenvalue buckling analysis solver, and the scaled eigenmode of the first positive eigenvalue was imported as a geometric imperfection for the quasi-static analysis. Based on this approach, the number of different models to be analyzed was substantially high. Each model described a different combination of beam type, load conditions, and corrosion topology.

Creating an Abaqus model from scratch, based on the procedure described in this report, could require more than one hour of work by an experienced user. Of course, some models can be produced by slightly modifying existing configurations, such as adjusting the remaining corrosion thickness parameter. However, the productivity could be remarkably increased with programming implementation. For this purpose, following a methodology initially designed and employed by the researchers in (14), an Excel sheet that described one tested scenario in each row was introduced (Fig. 4.11). The scenario parameters described in the Excel sheet concerned only the configuration of the geometry.

Geometry						Bearing		Web Corrosion				Stiffener Geom. & Corrosion				Slab		
name	Depth	Flange thick.	Webthick.	Flange length	Length	Bearing Length	Lo	Pattern	t web loss	CL1	CH1	Thickness	width	t loss	CHS	Width	thickness	Cover plate
plate	62.875	0.875	0.375	14.00	634.00	12.00	3.00	W2	0.20	0.4	0.05	0.625	6.00	0.20	0.2	86.000	8.5	0.875
plate	62.875	0.875	0.375	14.00	634.00	12.00	3.00	W2	0.30	0.4	0.05	0.625	6.00	0.20	0.2	86.000	8.5	0.875
plate	62.875	0.875	0.375	14.00	634.00	12.00	3.00	W2	0.40	0.4	0.05	0.625	6.00	0.20	0.2	86.000	8.5	0.875

Figure 4.11: Excel sheet describing geometry of tested scenarios

This Excel sheet constituted the input for the new developed Python script. The script operates through Abaqus and results in two files for each row (one for eigenvalue buckling analysis and one for quasi-static) that can be executed by the available Abaqus solvers. The loading conditions are described in the script. The dead load is user defined, in contrast to live loads. Due to the assumed span length that exceeded 50 feet, the HS20 design load was exclusively applied. The most sensitive procedure during building the model was the mesh generation. Much effort was put into creating a reliable combination of edge partition settings that resulted in a high-quality mesh independently of beam geometry and corrosion topology. To validate the outcome of the script, a mesh check was always performed.

4.3.8 Definition of Failure

The conducted experiments and the computationally analyzed scenarios revealed that there was actually a peak load beyond which the post-buckling behavior was characterized by a reduction of load. As will be presented in Section 7.1, the developed numerical model was able to accurately capture this maximum load before the termination of the analysis. Thus, for the parametric analysis, the bearing load at the last computational step was considered as the peak load and, consequently, the capacity of the corroded end.

In order to ensure the smooth operation of the developed methodology and that every analysis was terminated due to instability phenomena, supplementary scripts initially developed in the framework of (14) were modified to read the Abaqus output file, and additionally to bearing load, data relevant to the maximum out-of-plane displacement and Von Mises stresses were automatically extracted.

An example is given in Fig. 4.12, where multiple conclusions could be drawn for a plate girder combined with the W3 corrosion scenario. The damage condition was characterized with web and stiffener corrosion height equal to 10% and 20% of the depth, respectively. Results are presented for 80% stiffener loss and web thickness reduction in the range of 20% to 80% of intact web thickness. For cases with increased web loss, buckling occurred shortly after the web yielding initiation at the support area. Out-of-plane displacement along both sides of the web denoted the formulation of a full buckling wave, while the capacity was linearly reduced for increasing web section loss.

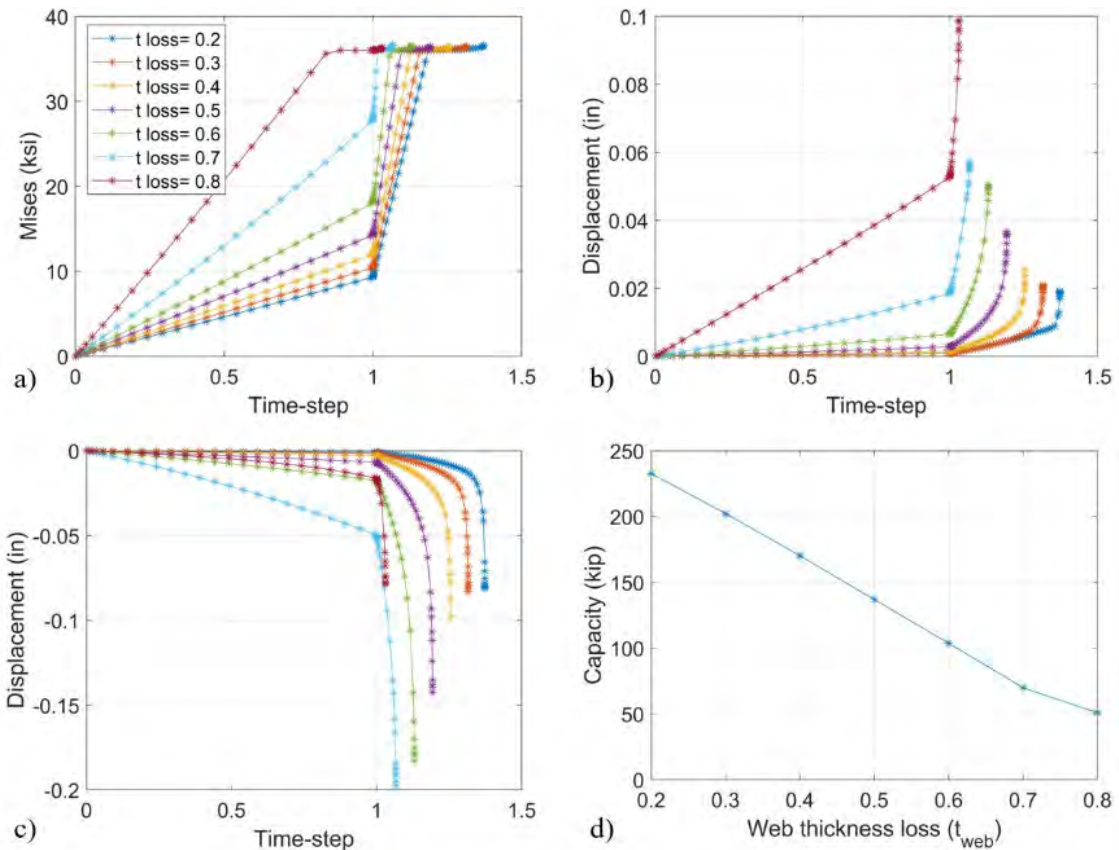


Figure 4.12: Set of data extracted and plotted from each group of analyses: a) maximum Von Mises stress magnitude; b) maximum positive and c) negative lateral displacement for every computational step; and d) bearing load at last load increment of each model

This page left blank intentionally.

5.0 Post-Processing of Corrosion Data

The summary sheet presented in Section 2.0 was implemented to summarize corrosion data from the available reports. A MATLAB script was developed to extract, manage, and process the recorded data. The script followed the structure of the summary sheet, as it initially distinguished beam ends with respect to C1 and C2 configurations, and afterward, it accounted for the corresponding web corrosion and hole patterns. It also satisfied all the different cases, such as web hole combinations and description for stiffeners at both faces of the web belonging to the same end. After having classified and saved all summarized data, it was possible to develop statistical information about the appearance of the phenomenon and ultimately identify common characteristics that would lead to the definition of the most prevalent geometries of the deterioration.

Following the procedure described previously, the characteristics of all 210 beam ends were recorded and analyzed. Out of the 210 cases, 120 and 70 recordings described beam ends with a unique (C1) and two bearing stiffeners (C2) at each face, respectively.

5.1 General Metrics for C1 Configuration

In total, 120 beam ends in compliance with the C1 configuration were studied. From this sample, 3 cases included only stiffener corrosion data. It is worth noting that out of the 117 remaining beam ends, only 30% (35 out of 117) were not reported with at least one web hole at the support area. Table 5.1 presents the population of each hole scenario (as a unique case or in hole combinations) in correlation with the corresponding web corrosion topology that was reported. W1 and W5 were the governing patterns, which describe 70% of the corroded ends. It can be also seen that H1 was the dominant hole scenario, with 60 appearances out of the 104 documented holes. On the other hand, the H3 pattern described only 9% of holes in the field, while the H4 did not exceed 13%. In Table 5.1, the cases shown in red were disregarded, as they were very few. In total, the remaining cases comprised 90% of all the scenarios found in inspection reports and were considered as an adequate threshold.

Table 5.1: General metrics for web corrosion of beams with unique bearing stiffener (C1 configuration)

Beams with one bearing stiffener									
	All	No Hole	H1	H2	H3	H4	H1+H2	H1+H4	H3+H4
W1	40	13	21	0	0	2	0	4	0
W2	20	12	0	8	0	0	0	0	0
W3	10	2	4	0	2	0	2	0	0
W4	5	1	1	0	0	0	3	0	0
W5	42	7	16	2	3	1	7	2	4
Total	117	35	42	10	5	3	12	6	4

Fig. 5.1 presents the number of deteriorated stiffeners in association with the corresponding web condition. The low density of cases with corroded stiffeners was unexpected,

considering that only 32 stiffeners were reported with deterioration signs, while based on the beam end configuration (C1), 240 bearing stiffeners were examined (one per web face) in total. However, more than half of the reported cases were combined with the presence of a hole. A possible interpretation of this behavior is that primarily severe stiffener corrosion was reported. Based on these observations and in order to overcome the low density of the available data, the stiffener corrosion was studied independently of the web condition.

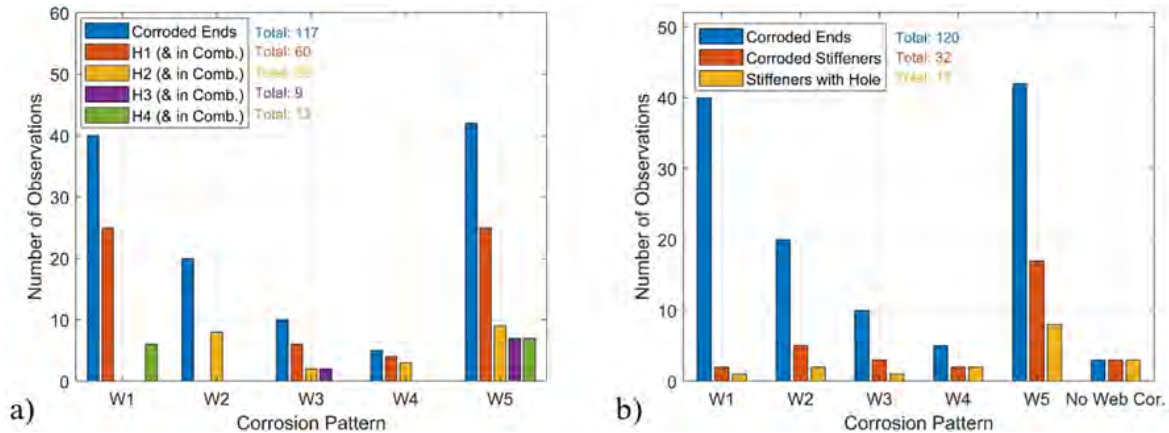


Figure 5.1: Web corrosion in correlation with a) web holes and b) stiffener condition for C1 configuration

5.2 General Metrics for C2 Configuration

Out of the 90 beam ends with two bearing stiffeners (C2), 19 of them exclusively reported stiffener corrosion data (Table 5.2). Out of the 71 remaining beam ends, 58% (41 out of 71) were not combined with web holes. Fig. 5.2a presents the population of each hole scenario (as a unique case or in hole combinations) in correlation with the corresponding web corrosion patterns that were associated with it. The smaller sample of beams with C2 configuration, in combination with the increased cases that excluded description of the web condition, resulted in fewer listed cases describing web holes. Consequently, in order to not further reduce the available sample, the web hole patterns were investigated independently of the web corrosion patterns.

Fig. 5.2b presents the number of deteriorated stiffeners in association with the corresponding corrosion patterns describing the web condition. It is worth noting that the sample size of corroded stiffeners was significantly larger than the one for the beams with the C1 configuration.

Table 5.2: General metrics for web corrosion of beams with two bearing stiffeners (C2 configuration)

Beams with two bearing stiffeners									
	Frequency	No Hole	H1	H2	H3	H4	H5	H1+H2	H3+H4
W1	19	17	0	0	0	2	0	0	0
W2	17	6	6	3	0	1	0	1	0
W3	14	11	1	0	2	0	0	0	0
W4	12	4	2	1	0	2	2	1	0
W5	9	3	2	2	0	1	0	0	1
Total	71	41	11	6	2	6	2	2	1

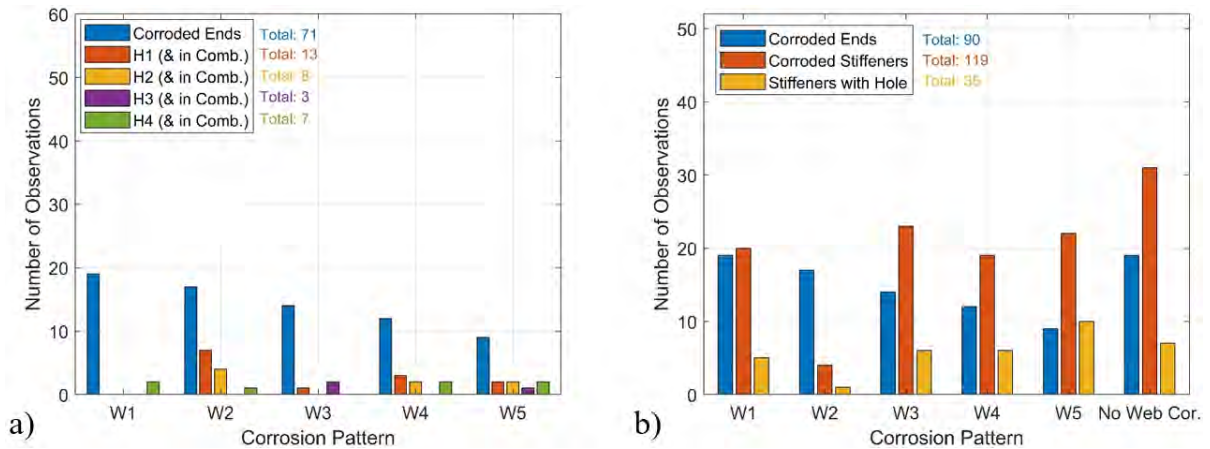


Figure 5.2: Web corrosion in correlation with a) web holes and b) stiffeners condition for C2 configuration

Table 5.3 distinguishes the cases where section loss was reported at the inner (S1), outer (S2), or both bearing stiffeners per web face. In general, the most prevalent behavior was with both stiffeners having exhibited thickness reduction.

Table 5.3: General metrics for stiffener corrosion of beams in compliance with C2 configuration

	Corroded Stiffeners (with Holes)	S1	S2	Both	Hole at S1	Hole at S2
W1	20 (5)	10	2	4	3	2
W2	4 (1)	0	2	1	0	1
W3	23 (6)	2	1	10	4	2
W4	19 (6)	1	0	8	4	2
W5	22 (10)	0	1	11	2	8
No Web Cor.	31 (7)	6	3	11	5	2
Total	119 (35)	19	9	45	18	17

5.3 General Metrics for Beam Geometry

Information included in this subsection describes the geometry of a typical stiffened beam end. These metrics describe the as-designed properties of the viaducts. However, this data was essential for the initiation of the numerical analysis at future stages of this work.

Except for information relevant to corrosion, the summarizing reports included parameters that allowed exploration of the support area characteristics. Plate girders were mainly reported, with depth in the range of 58 to 74 inches. Consequently, the bearing length of the recorded cases did not exceed 20% of the depth.

5.4 Final Corrosion Patterns

Following the procedure described in Sections 5.1 and 5.2, the recorded corrosion characteristics of stiffened beam ends were studied, and the general patterns defined in Section 3 were quantified to determine the final corrosion patterns. The final corrosion patterns reflected the most common corrosion topologies that inspection engineers find in the field. The output data and graphs produced from this investigation are presented in their entirety in Appendices 1 and 2, for beams with a unique bearing stiffener and two bearing stiffeners per web face, respectively.

Data in Table 5.4 refer to beams in compliance with the C1 configuration and present the range of variation of all the parameters involved in describing the general patterns for web and stiffener section loss and holes. The first six cases describe the thickness reduction profiles along the web, while Cases 7 to 15 are the web areas with holes. Finally, the bounds for stiffener corrosion and holes are also included.

Fig. 5.3 visualizes the upper bounds of the corrosion parameters for each of the patterns included in Table 5.4. The web hole patterns are projected on the associated web corrosion patterns, and the stiffener corrosion bounds have also been included.

Table 5.4: Analysis of final corrosion topologies for cases with unique bearing stiffener per web face

Web Section Loss Pattern						
No.	Pat.	CH₁ (d_w)	CH₂ (d_w)	CL₁ (d_w)	CL₂ (d_w)	t_{loss} / t_{web}
1	W1	0–20%				0–10%, 50–90%
2	W1	100%				30–80%
3	W2	0–20%		0–130%		20–80%
4	W3	0–16%		0–85%		40–80%
5	W4	70–100%	5–15%	0–25%	20–120%	40–90%
6	W5	100%	0–15%	0–70%		20–80%
Web Hole Pattern						
	Pat.	HL	HH (d_w)	c (d_w)	Web pat.	
7	H1	0–100% (c)	0–7%		W1	
8	H1	0–100% (c)	0–7%		W1	
	H4	0–100% (c)	0–5%	100%		
9	H2	0–30% (d _w)	0–8%		W2	
10	H1	0–100 % (c)	0–9%		W3	
11	H1	0–100% (c)	0–66%		W4	
	H2	0–54% (d _w)	0–13%			
12	H1	0–100% (c)	0–60%		W5	
13	H3	0–50% (d _w)	0–10%		W5	
14	H1	0–100% (c)	0–60%		W5	
	H2	0–30% (d _w)	0–8%			
15	H3	0–15% (d _w)	0–5%		W5	
	H4	0–60% (d _w)	0–20%	100%		
Stiffener Section Loss Pattern						
		SC (d_w)	t_{loss} / t_{stif}			
		0–25%, 100%	10–90%			
Stiffener Hole Pattern						
	Pat.	SHL (w_{stif})	SHH (d_w)			
16	HB	0–100%	0–20%			

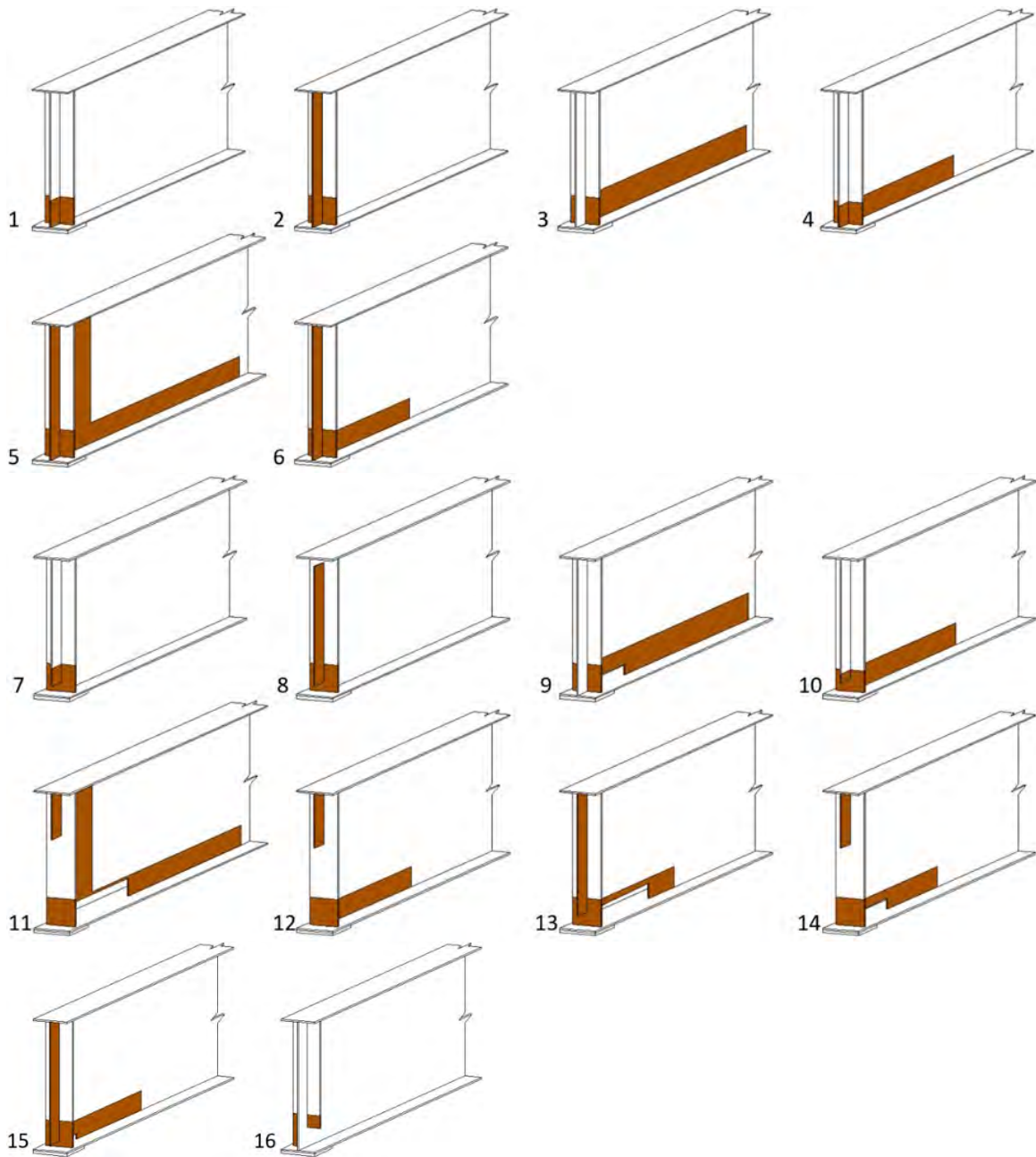


Figure 5.3: 16 final corrosion patterns for beam ends with one bearing stiffener, including corrosion and hole patterns for web and stiffeners (shaded areas illustrate corrosion domains)

Table 5.5 includes data for beams with two bearing stiffeners and presents the range of variation of all the parameters involved in describing the general patterns for web section loss and holes. Initially, the corrosion patterns are presented (Cases 1 to 7), while Cases 8 to 12 describe the web areas with holes. Following the numbering of Table 5.5 and the annotation of Tables 2.12 to 2.16, Fig. 5.4 visualizes the upper bounds of the web corrosion scenarios. As previously described, the holes were studied independently of the web condition, thus they are presented accordingly in Fig. 5.5.

Table 5.5: Analysis of final corrosion topologies for cases with two bearing stiffeners per web face

Web Section Loss Pattern						
No	Pat.	CH ₁ (d _w)	CH ₂ (d _w)	CL ₁	CL ₁ (d _w)	t _{loss} / t _{web}
1	W1	0–20%				20–70%
2	W1	0–100%				20–70%
3	W2	0–50%		0–100% (α)		0–50%
4	W2	100%		0% (α)		0–50%
5	W3	0–15%		10–100%		20–80%
6	W4	0–10%	10–100%	20–80%		20–80%
7	W5	0–16%	10–100%			20–80%
Web Hole Pattern						
	Pat.	HL	HH (d _w)	c (d _w)		
8	H1	0–100% (c)	0–7%			
9	H2	0–100% (c)	0–7%	50–100%		
10	H3	0–13% (d _w)	0–3%			
11	H4	0–100% (d _w)	0–10%			
12	H5	0–40% (d _w)	0–7%			

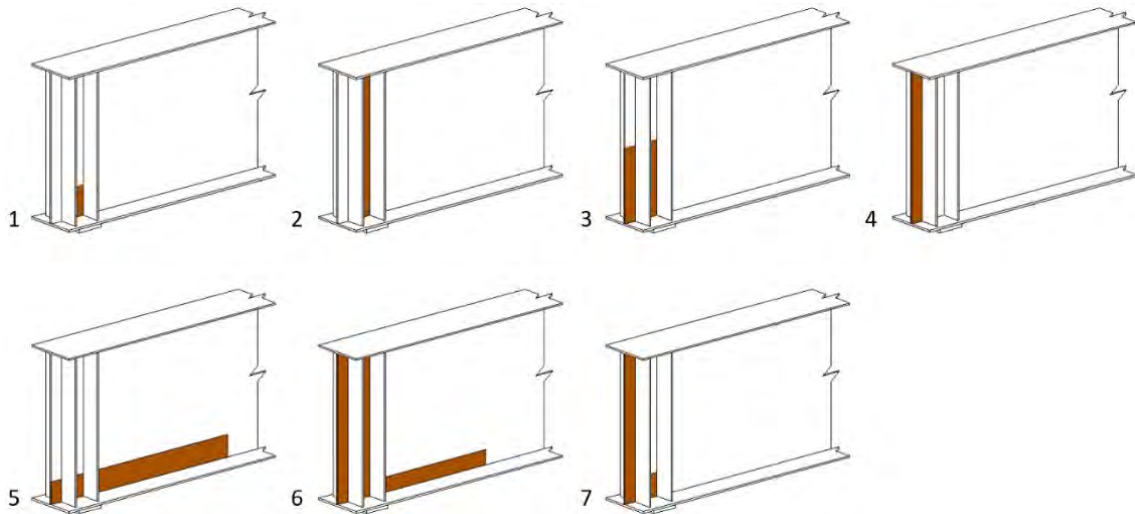


Figure 5.4: Seven final web corrosion patterns for beam ends with two bearing stiffeners (shaded areas illustrate corrosion domains under assumption of uniform section loss)

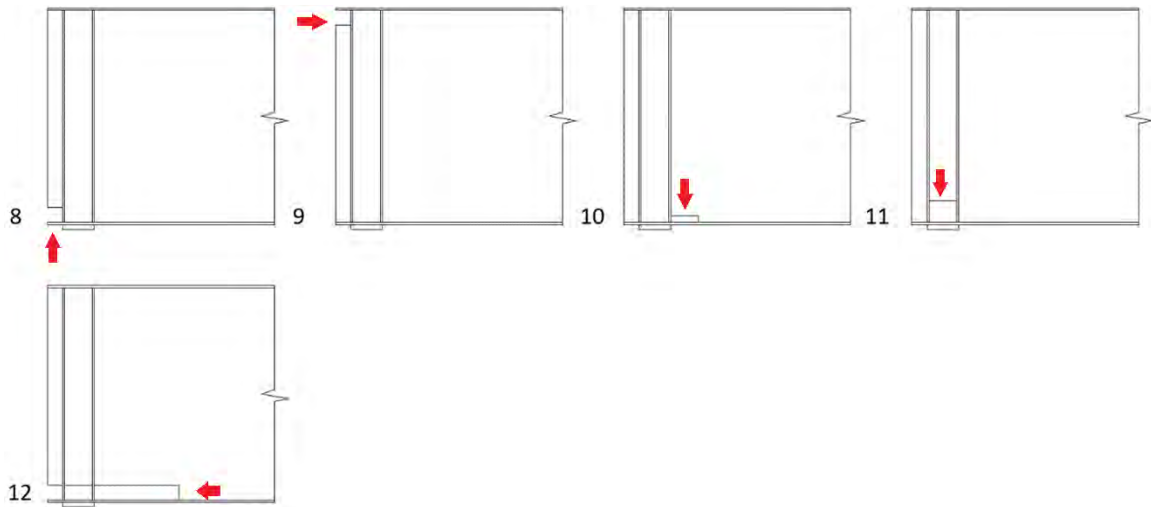


Figure 5.5: Five final web hole patterns for beam ends with two bearing stiffeners

Stiffener corrosion was examined individually for the inner and the outer stiffeners. The investigation revealed that there was no significant variation of the deterioration parameters for beams belonging to these two categories, neither for the thickness reduction characteristics nor for the holes. Fig. 5.6 visualizes the upper bounds of the corrosion characteristics for each of the three final patterns included in Table 5.6. Case 13 describes the section loss domain along the stiffeners, while Cases 14 and 15 describe holes at the bottom and the top of the stiffener, respectively. For illustrative purposes, the holes have been projected exclusively at a unique stiffener; however, they can be found at any of the four stiffeners.

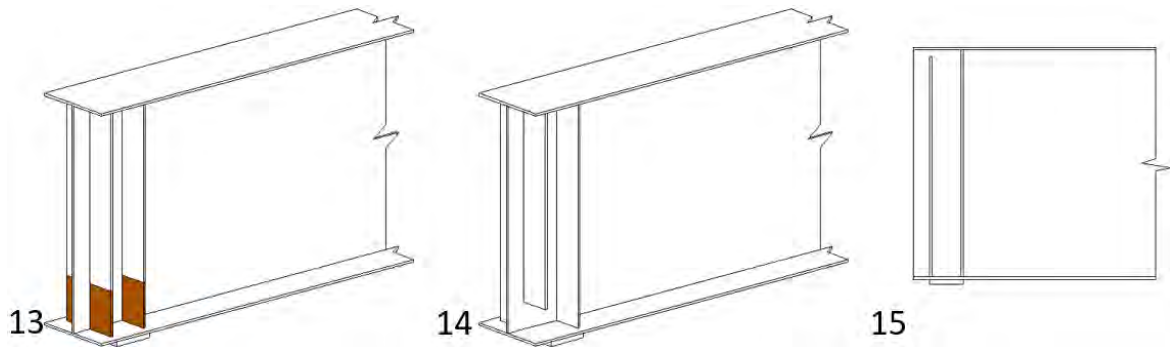


Figure 5.6: Final stiffener corrosion pattern and two hole patterns for beams in compliance with C2 configuration; 14 and 15 are holes located at stiffener's bottom and top, respectively

Table 5.6: Analysis of final corrosion topologies for stiffeners

Stiffener Section Loss Pattern						
No.		SC (d_w)	t_{loss} / t_{stif}			
13		0–20%, 100%	10–90%			
Stiffener Hole Pattern						
	Pat.	SHL (w_{stif})	SHH (d_w)			
14	HB	0–100%	0–20%			
15	HT	0–100%	0–3%			

The existence of one or two bearing stiffeners per web face unavoidably split the web to a different number of subdomains affecting the water flow of the leaking water. However, having quantified the bounds of the most common corrosion topologies, a comparison between the damaged areas (Fig. 5.7) revealed many similarities and common trends.

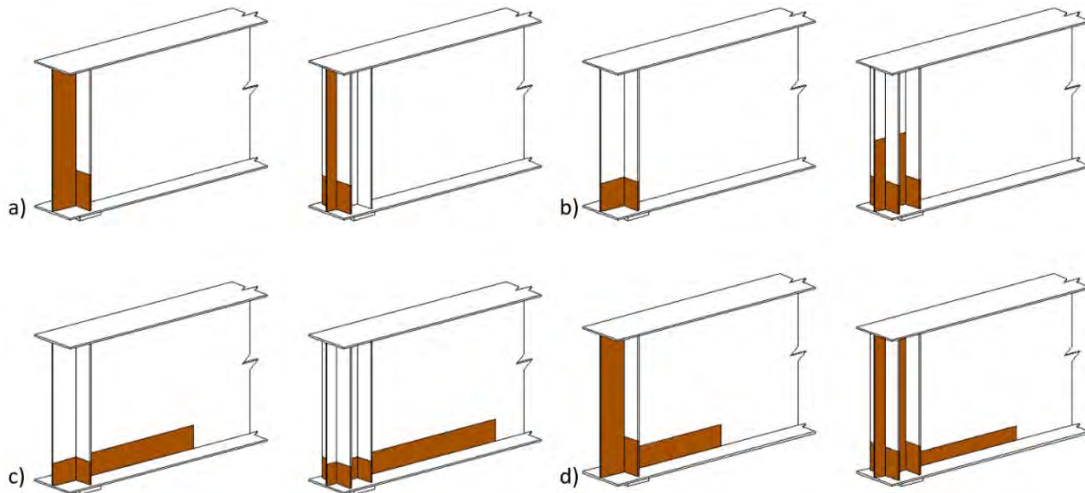


Figure 5.7: Comparison of damage cases with one and two bearing stiffeners per web face reveals similar corrosion patterns between configurations (displayed cases include information for web and stiffeners)

This page left blank intentionally.

6.0 Experimental Results

This section describes the results obtained from the experimental testing of the two naturally corroded girders, Specimens A and B. Specimen A resembles fully stiffened girders, while Specimen B is a rolled girder with partial stiffeners welded above bearing, which constitutes a common configuration for diaphragm connections.

In both cases, the critical corrosion characteristics defined the failure mode of the girders. This section includes some introductory observations and a detailed description of the failure mechanisms, along with several graphs on each test. At the end of the section, capacity predictions are also included, making use of point cloud data.

6.1 Specimen A

Specimen A was successfully tested on March 24, 2021. Given the experimental and instrumentation configuration, the applied load was estimated as the difference between the loads measured at the crossbeam and the intact end. As an intermediate step, the total reaction force developed at the crossbeam was calculated from the summation of the recordings in the two load cells (east and west) installed at the bottom end of each rod.

Fig. 6.1a depicts the applied load versus the vertical displacement at the tested end and captures the failure load at 223.8 kip for 0.87 inches of displacement. It is worth noting that the load was applied incrementally every 20 kips, while at the end of each loading increment, the project team inspected the beam's condition and, in particular, the interaction between the bottom flange of the tested end and the bridge bearing. For applied load greater than 150 kip, these loading pauses are captured in Fig. 6.1a as small steps characterized by minor load drop. The observed behavior is solely related to the utilized hydraulic system and not to the mechanical response of the specimen.

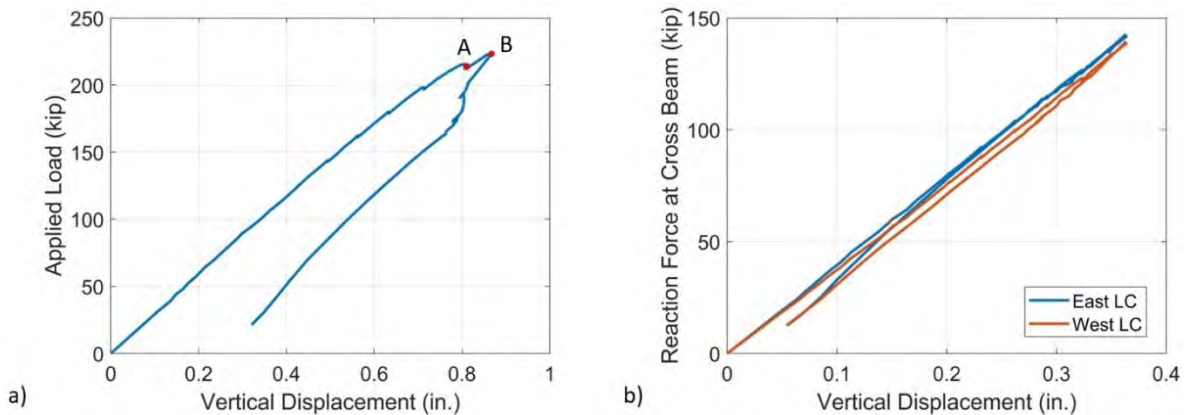


Figure 6.1: a) Applied load: vertical displacement plot for Specimen A; b) reaction force developed at crossbeam area was calculated from summation of loads captured by east and west load cells

Furthermore, Fig. 6.1a illustrates a relatively linear response of the specimen until failure, where a sudden capacity drop occurred. This behavior is consistent with the macroscopic observation of the specimen, where no large deformations were noticed prior to the sudden failure. The whole experimental process was captured by two cameras (Figure 6.2). The first camera recorded the plane of the web (side view of the beam), while the second camera recorded the beam profile. These photos illustrate the girder's deformation at the initial condition before loading, followed by deformations observed at different steps of the experimental procedure (points from A and B, Fig. 6.1a).



Initial



A

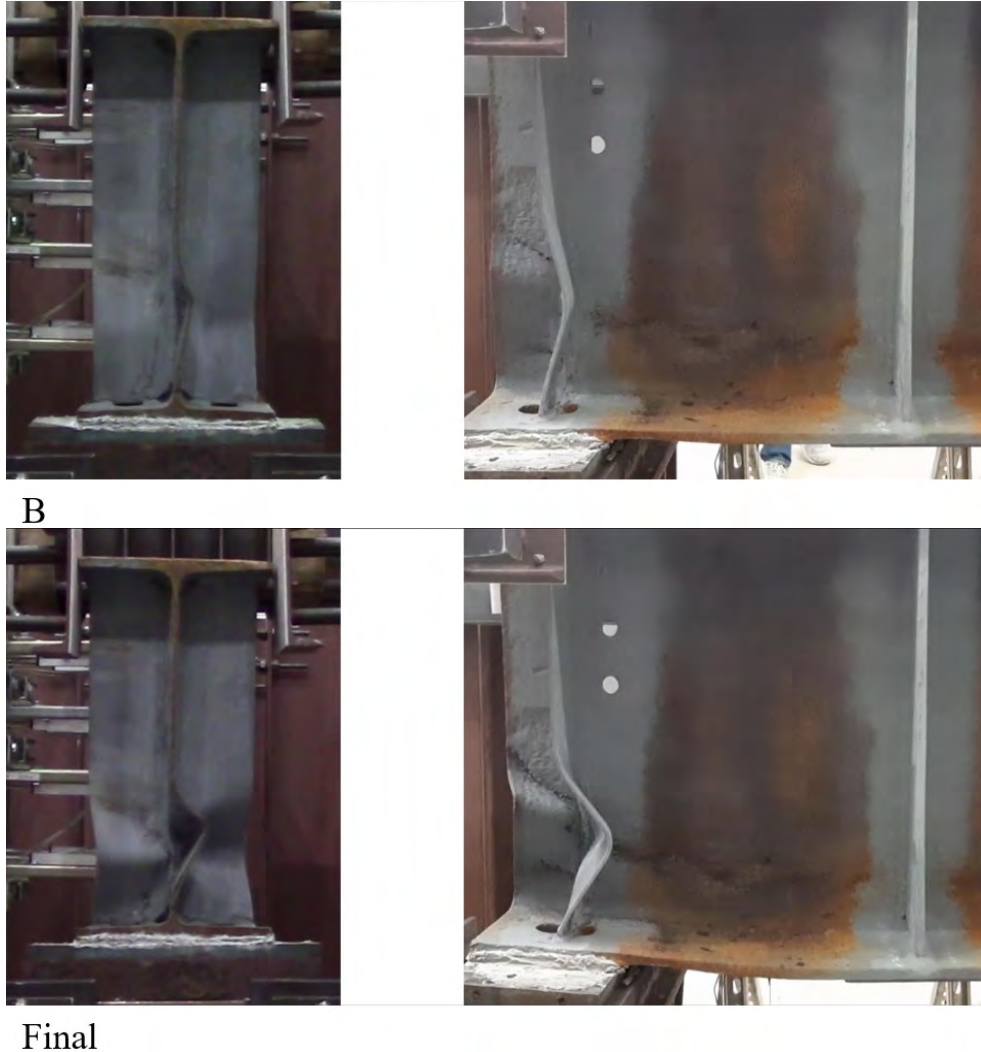


Figure 6.2: Side-by-side images showing side view of web and profile view of beam during experiment (A and B correspond to Fig. 6.1a)

From the initial condition pictures, web deviation from straightness was observed at the lower half of the depth. In addition, perforations also existed at the upper web half, due to the riveted plate removal. At Point A, which corresponds to applied load equal to 88% of the failure load, a slight out-of-plane bending of the bearing stiffener was captured.

Point B corresponds to the bearing capacity of Specimen A, and the failure mode is characterized by lateral deformations mainly developed at the web region toward the end of the beam and the bearing stiffener, governed by the initial web deviation from straightness at this area. In addition, the failure seemed to propagate diagonally following the region of the extensive section loss presented in Fig. 3.8a.

Taken altogether, an assertion that the failure mode is solely governed by the web characteristics (deviation from straightness and section loss profile) would be inaccurate, given that the welded bearing stiffeners have reduced thickness to resemble corrosion-induced section loss.

Fig. 6.3 presents the out-of-plane displacement profile as it was recorded from the two potentiometer columns; the exact configuration was previously presented in Fig. 3.10. The instruments were positioned over the height of the web close to the bearing (red) and adjacent (blue) stiffeners. Results are presented for two different loads: at 90% and the maximum applied load (F_u). The used potentiometers had a 4-inch capacity and were placed close to half of the stroke, in order to capture possible sideways deflection along both directions. The instruments recorded relative displacements from the moment of loading initiation; thus, the initial imperfection of the beam was not captured. As a result, the vertical black line illustrates the initial web position, assuming no deviation from straightness prior to load application. Between adjacent potentiometers in the same instrumentation column, the web section was considered linear.

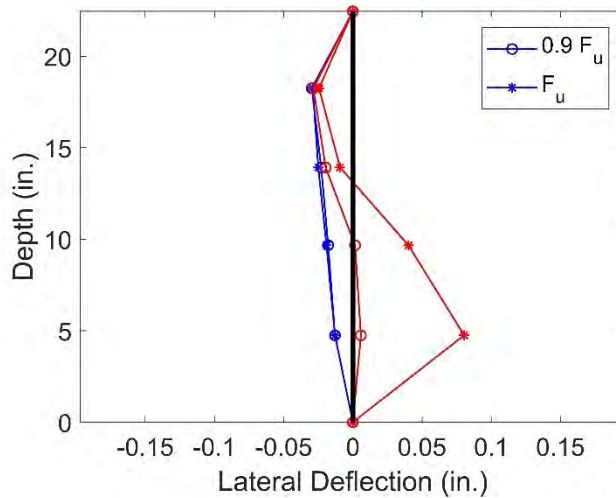


Figure 6.3: Beam's end lateral displacement profile as recorded from outer (blue) and inner (red) column of potentiometers, for two different loads, 0.9 and 1.0 F_u .

Interpreting Fig. 6.3, once again a sudden failure was captured, with displacements mainly developed close to bearing. Another interesting point lies at the negligible variation of data captured close to the adjacent stiffener (blue) between 0.9 and 1.0 F_u , denoting that the observed mode was not related to the shear failure of the panel.

6.2 Specimen B

Specimen B was successfully tested on April 28, 2021, on the same testing rig that Specimen A had been previously tested. Consequently, the same data post-processing procedure was followed to calculate the incrementally applied load at the bottom flange of the tested end.

The applied load versus the vertical displacement at the tested end is presented in Fig. 6.4a, where mainly a linear response was captured until the maximum load of 172.3 kip for 0.59 inch. The beam's behavior beyond that point was characterized by an instant reduction of the end's capability to bear load, as well as with rapidly increasing vertical and lateral deformations, denoting its failure.

Initially, making use of the two load cells installed at the lower end of each rod, employed to anchor the crossbeam at the strong floor, the reaction force developed there versus the vertical displacement at the same location was calculated and is presented in Fig. 6.4b. In the same figure, an excellent consistency of the reaction force developed along the two rods is highlighted.

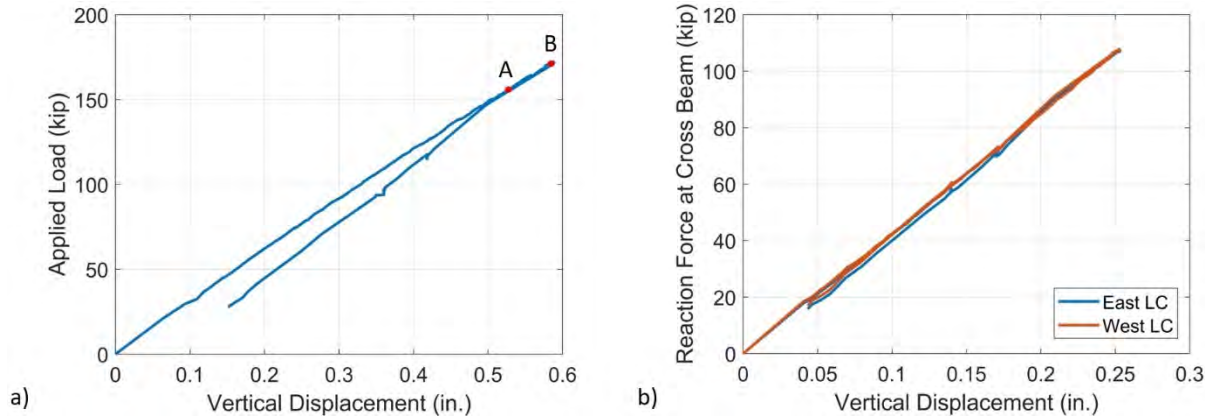
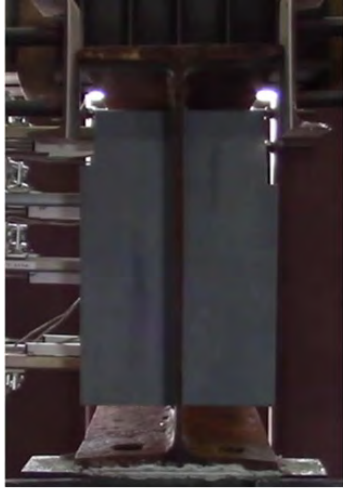


Figure 6.4: a) Applied load vs. vertical displacement plot for Specimen B; b) total applied load was calculated as difference between reaction force at intact end and summation of two load cells installed at bottom of each rod (west and east side)

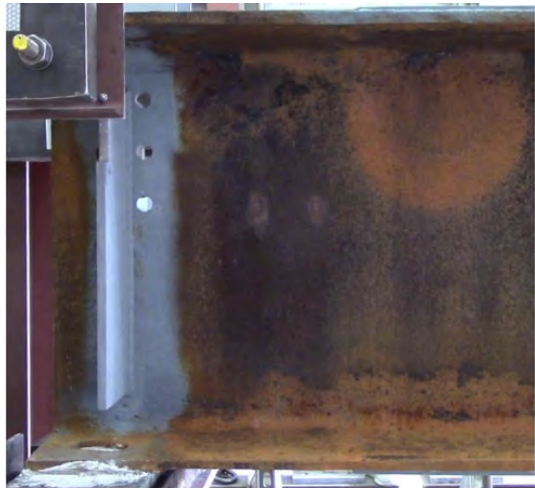
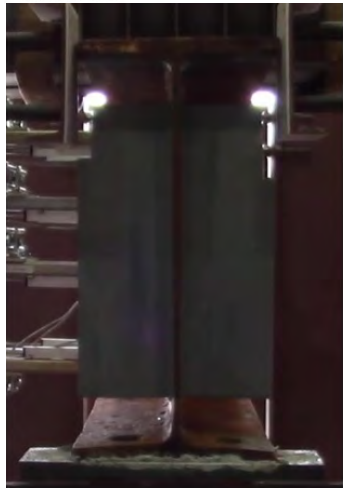
In Fig. 6.5, the deformation of the corroded end is presented, using images captured from two cameras that recorded the experimental process. The first camera recorded the plane of the web (side view of the beam), while the second camera recorded the beam profile. These photos illustrate the girder’s deformation at the initial condition before loading, followed by deformations observed at different steps of the experimental procedure (Points A and B, Fig. 6.4a).

The riveted plate in Fig. 3.3 was removed prior to the partial stiffener welding, revealing perforations at the upper part of the web (Fig. 6.5). Other than that, visual observation did not reveal significant deficiencies or deformations, before loading initiation. At Point A, which corresponded to 90% of the maximum applied load, the cameras’ captures did not depict any significant variation in specimen’s geometry, strengthening the linear response presented in Fig. 6.4a.

At Point B, where the undertaken load reached the magnitude of 172.3 kip, the whole web seemed to translate laterally along the same direction, with peak displacements concentrated at the bottom unstiffened part of the web. It is worth noting that, according to the remaining thickness profile derived from point clouds (Fig. 6.5b) capturing both web surfaces, the bottom web part coincided with a region of section loss.



Initial



A



B



Final

Figure 6.5: Side-by-side images showing side view of web and profile view of beam during experiment (A and B correspond to Fig. 6.4a)

Fig. 6.6a presents the lateral displacements as they were measured by the eight potentiometers for two different loads: 155.1 and 172.3 kip (0.9, and 1 F_u , where F_u is the failure load). Two columns of instruments had been installed, with four potentiometers each. The first column was placed to record the sideways deflection profile close to the partial stiffener (red), while the second one was placed 8 inches toward the inner side of the beam (blue), Fig. 3.15.

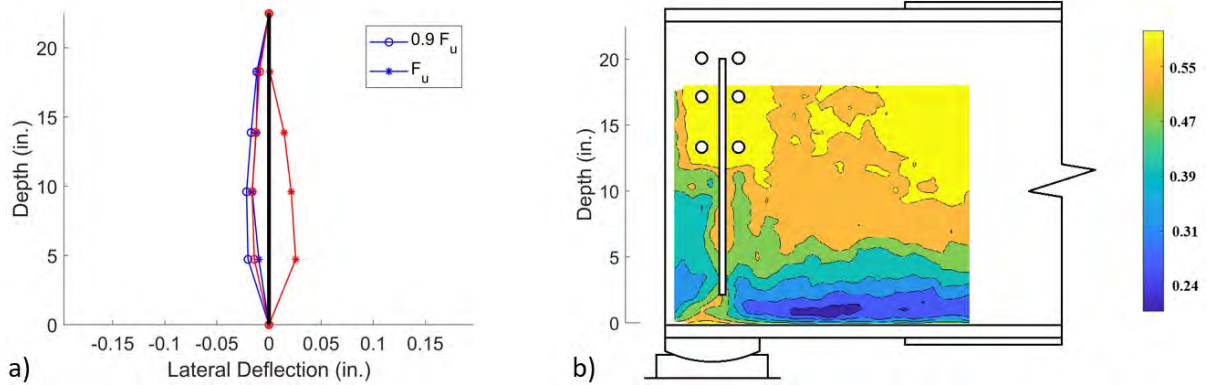


Figure 6.6: a) Measured web lateral deflections recorded close (red) and far (blue) for partial stiffener for 0.9 and 1 F_u , where F_u denotes maximum applied load; b) remaining thickness profile along web of Specimen B

Potentiometer data revealed no changes on lateral displacements profile, for the web part located far from the partial stiffener (blue), between the 90% of the maximum load and the obtained capacity. On the other hand, the recordings from the potentiometer array installed close to the partial stiffener agreed with observation of the specimen's deformed geometry, which indicated large displacements above bearing, with extensive distortion at the lower unstiffened part of the web.

It is worth noting that both experiments were terminated due to extensive post-peak inclination of the load spread beam installed between the hydraulic jacks and the actual bridge bearing (Fig. 6.7). The developed rotation was closely related to the cups that were installed on the top of the jacks' pistons and were meant to absorb the rotation at the same location. Their existence was preferred to avoid damaging the equipment, in case the developed rotation generated by distortion of the specimen exceeded the capacity of the bridge bearing, resulting in rocking phenomena between the load transfer beam and the pistons. However, a side effect of this configuration was that, potentially, it deactivated the operation of the actual sliding plates by absorbing the majority of the generated rotation. Even though pit corrosion was removed and grease was added at the interface between the two sliding plates, it seems that the reduced resistance of the recently fabricated cups provided less resistance, preventing the researchers from exploring the efficiency of the actual bridge bearing.



Figure 6.7: Both experiments terminated due to inclination of load spread beam, located between hydraulic jacks and bridge bearing

This page left blank intentionally.

7.0 Analytical Results

This section includes the results of the computational modeling. A high-fidelity computational model, which was capable of accurately predicting the capacity of composite plate girders with corroded ends, was validated based on the experimental data of Specimen A, as well as from the literature. Making use of the FEM, an extensive parametric analysis was conducted to gain better understanding of the mechanics of the corroded beam end.

Some interesting general observations from the parametric analysis are as follows.

- For the examined applied imperfection amplitude, the numerically obtained capacities proved to be only slightly sensitive to the initial geometric imperfection of the web and the bearing stiffeners.
- Three different general corrosion shapes were examined, and each one was found to have a different harming effect on the bearing strength.
- The dimensions of the corrosion-induced damage area that had significant effect on the remaining bearing capacity were defined for the web and the stiffeners.

7.1 Computational Model Validation

Following the procedure described in Section 4, the applied load–vertical displacement curve was plotted to compare the finite element output with the experimental results for Specimen A. Specimen B was not modeled, since its configuration did not include a web panel close to the tested end. Consequently, its failure mechanism lay more toward the mechanics of the unstiffened girders, which constituted the research topic of a previous study by the researchers.

Quasi-static analysis was performed up to failure, as post buckling was outside of the scope of this study. Comparison of load–vertical displacement curves for numerical and experimental models is presented in Fig. 7.1a, indicating that the computational model satisfactorily captured the failure load as well as the stiffness of the specimen. In detail, for Specimen A the difference between the numerically acquired peak load and the experimental value was 3.1% (experimental: 223.8 kip; FEM: 230.7 kip). In the same figure, the reaction force developed at the crossbeam area is also included (Fig. 7.1b).

It is also worth noting that the potentiometers monitoring the lateral displacements of the web were in fixed stations during the whole experimental procedure. On the other hand, the load was applied upward to the bottom flange of the tested end, resulting in vertical displacements that exceeded the 0.9 inch along the tested end of Specimen A, further resulting in two main sources of error. First, the employed instruments were constantly measuring different locations along the web, and second, in some cases, the remaining thickness along the recorded trajectories varied significantly.

Taken altogether, the researchers considered the provided accuracy adequate for macroscopic observation of the lateral displacement profile but not for calibration or validation of the FEM. Consequently, a comparison between experimental and numerical lateral deflections was not included in this section.

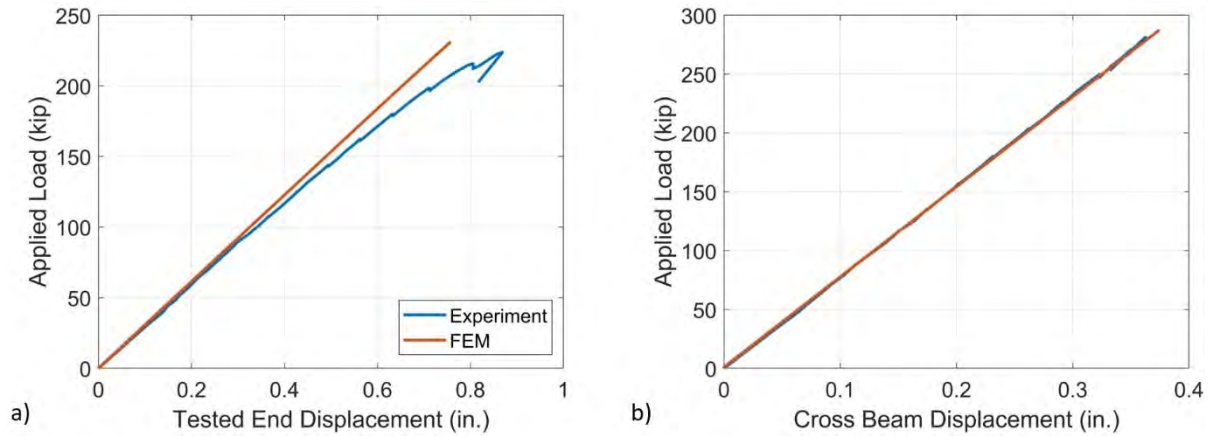


Figure 7.1: Comparison of experimental and numerical results a) at tested end and b) crossbeam area for Specimen A

Fig. 7.2 presents the failure mode as it was captured by the two cameras recording the experimental procedure as well as the FEM. Visual observation indicated that the computational model was able to capture satisfactorily the resulting displacements, which were mainly concentrated around the bearing stiffener.

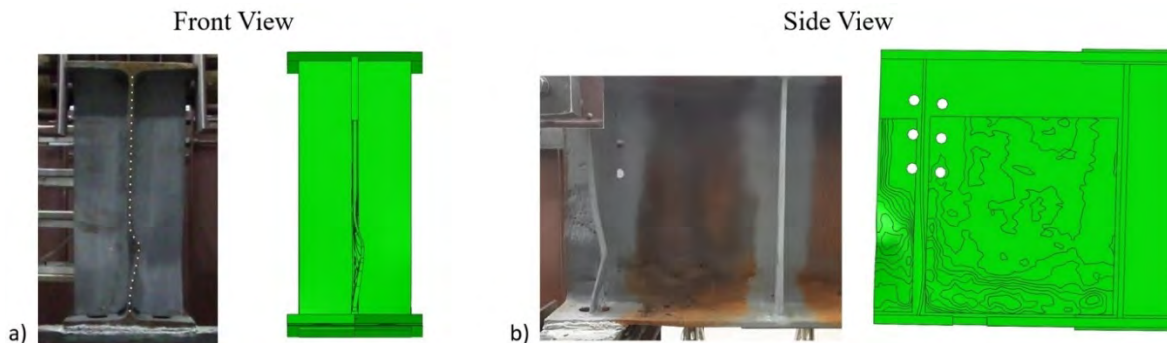


Figure 7.2: Experimental and numerical a) front and b) side view of Specimen A, at peak load

To conclude, based on the presented results for Specimen A, the model was considered valid and capable of capturing the stiffness, failure load, and mode of plate girders with corroded ends.

7.2 Composite Action Validation

Following the assumptions presented in Section 4.2, Fig. 7.3 depicts comparison between numerical and experimental results for the specimen POS2 tested by Mans (21). The presented aspect of the FEM was able to capture the stiffness of the girder, even after the bottom flange yielding, for vertical displacement equal to 75 mm. The analysis was not continued beyond 310 kip of applied load, where initiation of the concrete slab failure defined the test's outcome.

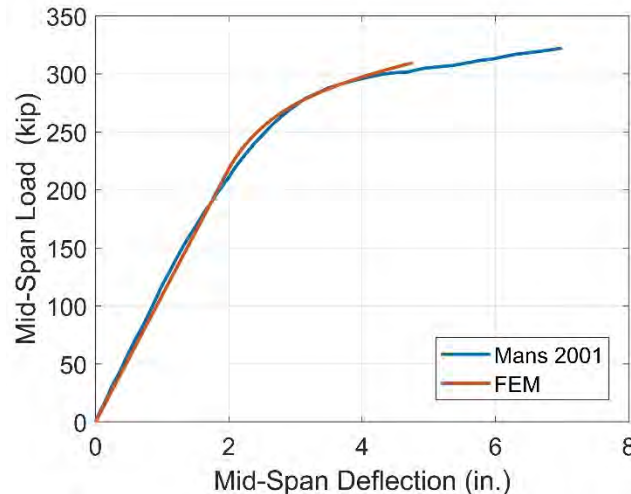


Figure 7.3: Comparison between experimental and numerical results for experiment conducted by Mans in composite girder

In short, by combining aspects from the two modeling approaches, one validated using a laboratory experiment of a beam with corroded end (this study), and a second one with a validated modeling approach of a composite beam test reported by Mans (21), the authors were able to capture both the composite action and the failure of girders with deteriorated stiffened ends.

7.3 Geometric Imperfection Amplitude

A previous study by the researchers revealed both experimentally (15) and numerically (16) the deleterious effect of web imperfections on the capacity of unstiffened girders with corroded ends. Specifically, it was highlighted that the corrosion-induced web deviation from straightness was a critical parameter that could significantly reduce the load-bearing capacity of deteriorated beams. Building on this experience and on inspection reports and inspectors' observations, the project team concluded that similar imperfections were also present on stiffened beams.

Consequently, analyses were carried out to evaluate the effect of geometric nonlinearities to the residual strength of stiffened ends. The pre-loading web deviation was incorporated in the simulated geometries by introducing and scaling imperfections based on the eigenmode

shapes. Each scenario was initially solved using the eigenvalue buckling analysis algorithm and the eigenmode that involved at the damaged end was introduced as geometric imperfection for the quasi-static analysis.

A general result that emerged from the finite element study was that, in contrast with unstiffened beams, the results were, in general, insensitive to geometric imperfections with magnitudes in the range of $0.1 t_{web}$ to $2 t_{web}$. Fig. 7.4 shows computed maximum loads for increasing imperfection amplitude. It is worth noting that among 170 examined scenarios, the most significant capacity reduction did not exceed 23%. Based on these findings, the most aggressive imperfection amplitude, equal to $1.0 t_{web}$, was considered for the rest of the parametric study.

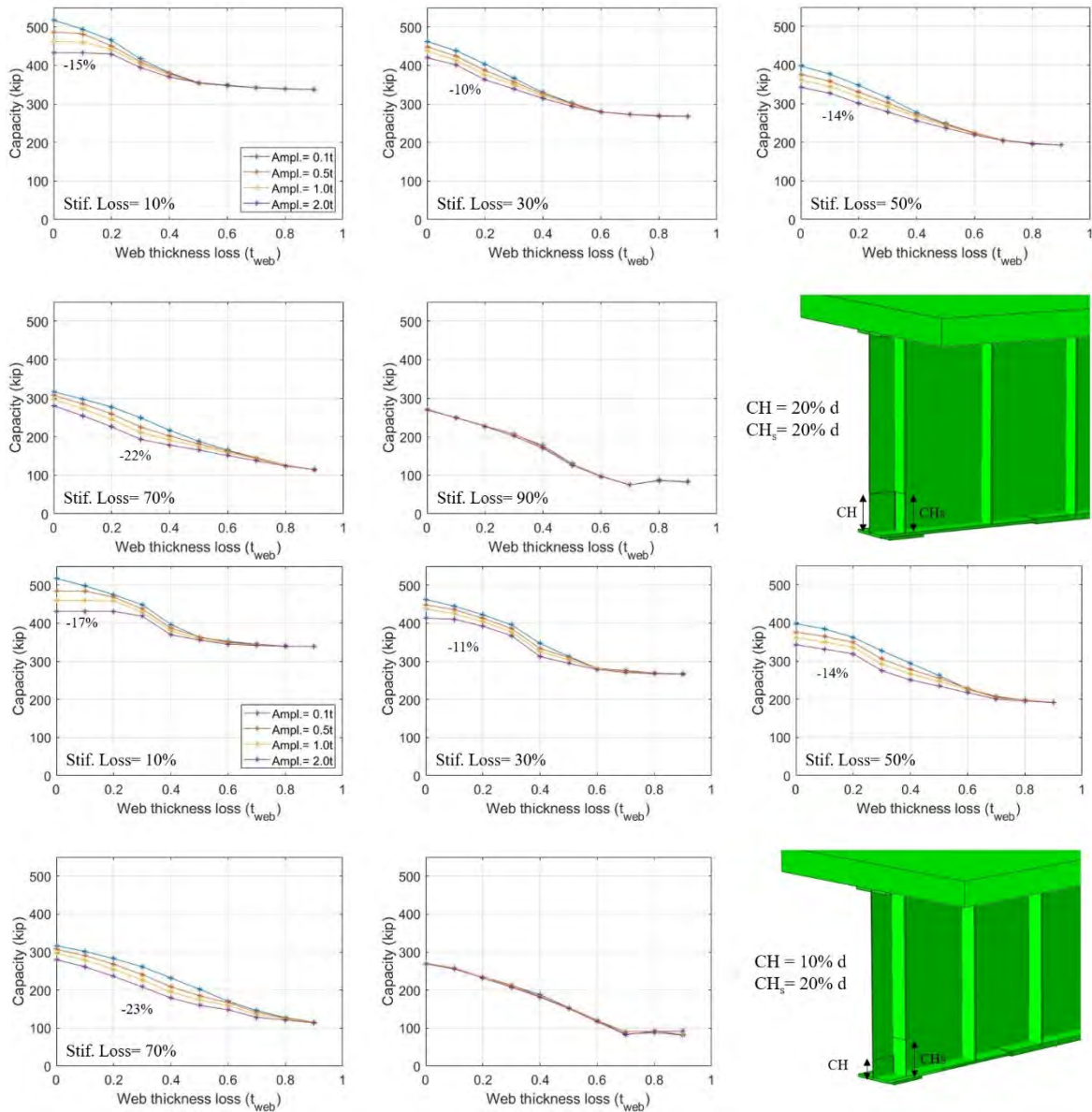


Figure 7.4: Capacity of beam ends with W1 corrosion pattern and imperfection amplitude in range of $0.1 t_{web}$ to $2.0 t_{web}$

7.4 Stiffener Corrosion Topology Effect

7.4.1 Stiffener Section Loss

A series of analyses was run to study the effect of the stiffener corrosion characteristics on the girder's strength. As shown in Fig. 7.5, the stiffener section loss was related to the residual bearing capacity for three different levels of web section loss (30%, 50%, and 70% of t_{web}) for scenarios according to the three examined corrosion patterns, W1, W2, and W3. The key observation from this figure was that there was a link between the remaining web and stiffener thicknesses. In detail, for limited web section loss ($t_{w\ loss} = 30\%$) and extensive stiffener damage ($t_{s\ loss} > 0.7 t_{web}$) the capacity tended to plateau, highlighting the web's contribution. On the other hand, for increased web damage, a linear relationship between the capacity and stiffener section loss was observed.

The damage dimensions of the web corrosion scenario examined for the W2 pattern were limited to 10% of depth and 20% of the web panel for corrosion height and length, respectively. Results presented in Fig. 7.5b depict minor effect of the web condition to the bearing capacity.

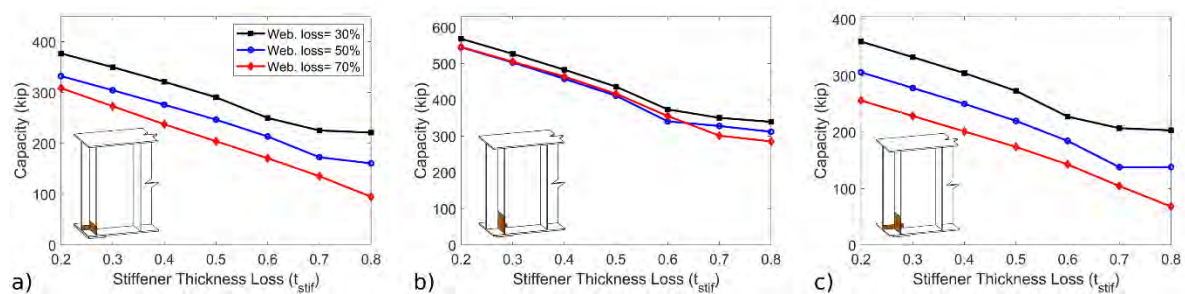


Figure 7.5: Effect of stiffener section loss related to a) W1; b) W2; and c) W3 patterns (relationship between bearing capacity and stiffeners' thickness could be idealized as linear)

7.4.2 Stiffener Corrosion Height Effect

To evaluate the impact of stiffener damage height to the bearing capacity, analyses were run for corrosion height (CHs) in the range of 5% to 100% of the stiffener depth (Fig. 7.6). For the presented results, stiffener section losses equal to 50%, 30%, and 40% were considered for the patterns W1, W2, and W3, respectively. A general picture emerging from Fig. 7.6 was that the remaining section within the bottom 10% of the stiffeners' depth defined the residual bearing capacity.

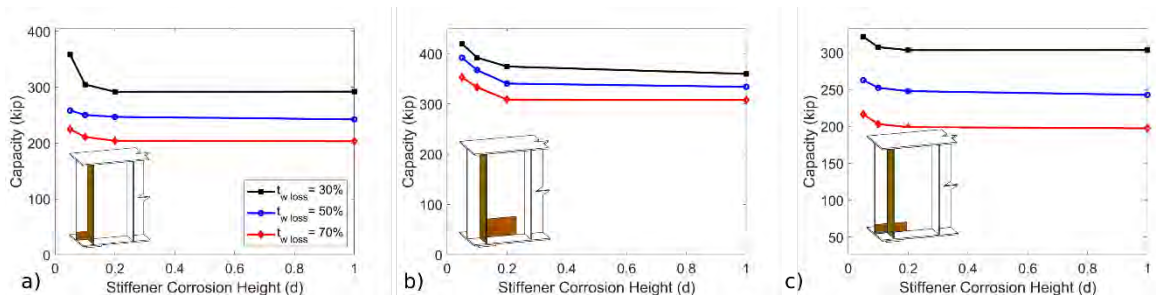


Figure 7.6: Effect of stiffener corrosion height related to a) W1; b) W2; and c) W3 patterns (stiffeners' condition at bottom 10% was critical for remaining capacity)

7.5 Web Corrosion Topology Effect

7.5.1 Section Loss Effect

In addition to the effect of stiffener damage, sensitivity analysis with respect to web section loss ($t_{w \text{ loss}}$) and to the web corrosion length (CL) and height (CH) was conducted. Fig. 7.7 shows that the relationship between capacity and web thickness loss was related both to the stiffener condition and the corrosion location and dimensions. In detail, in Fig. 7.7a, the damage area within the web was limited between the end of the beam and the pair of bearing stiffeners (W1 pattern). For this case, the capacity tended to plateau for a combination of extensive web damage ($t_{w \text{ loss}} > 0.5$) and limited section loss along the stiffeners ($t_{s \text{ loss}} = 20\%$). This behavior highlighted the load-bearing contribution of stiffeners in combination with the intact web part located within the panel. However, for increasing stiffeners damage, the capacity tended to linearly decrease. For the scenarios presented in Fig. 7.7b, where the web damage was exclusively located within the first panel (W2 pattern), the capacity curves plateau for web section loss was higher than 40%, regardless of the stiffeners' condition. For web section loss in the range of 20% to 80%, the capacity reduction did not exceed 28%. On the other hand, for the presented scenario in Fig. 7.7c, where the web damage extended along both sides of the bearing stiffeners (W3 pattern), capacity drop exceeded 50% for remaining web thickness in the range of 80% to 20%. Taken altogether, no clear relationship could be inferred between web section loss and remaining capacity, since it seemed to be also linked with other parameters.

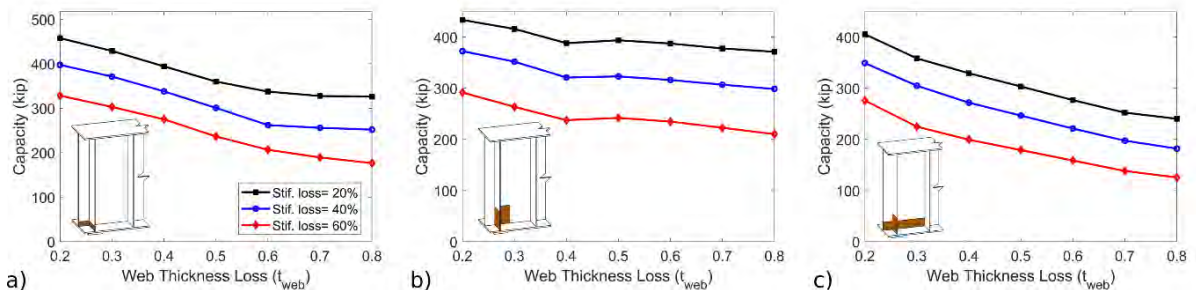


Figure 7.7: Effect of web section loss for scenarios related to a) W1; b) W2; and c) W3 patterns. (In some cases, stiffeners' contribution minimized aftermath of web section loss; dark- and light-brown shades represent minimum and maximum bounds of examined scenarios)

7.5.2 Web Corrosion Length Effect

Corrosion pattern W1 was created based on the assumption of uniform section loss along the whole domain between the bearing stiffener and the web region toward the end of the beam.

Consequently, in order to examine the effect of corrosion length on capacity, corrosion patterns W2 and W3 were exclusively employed. Fig. 7.8a demonstrates strong evidence that if the corrosion length (CL) exceeds the bearing by more than 10%, it does not have any further effect on the beam's strength. Fig. 7.8b and c show that the corrosion pattern that was characterized by section loss along both sides of the bearing stiffeners seemed to dominate the failure, with the corrosion length within the panel not affecting the remaining capacity regardless of its extent. The same trends were observed for different levels of stiffener section loss.

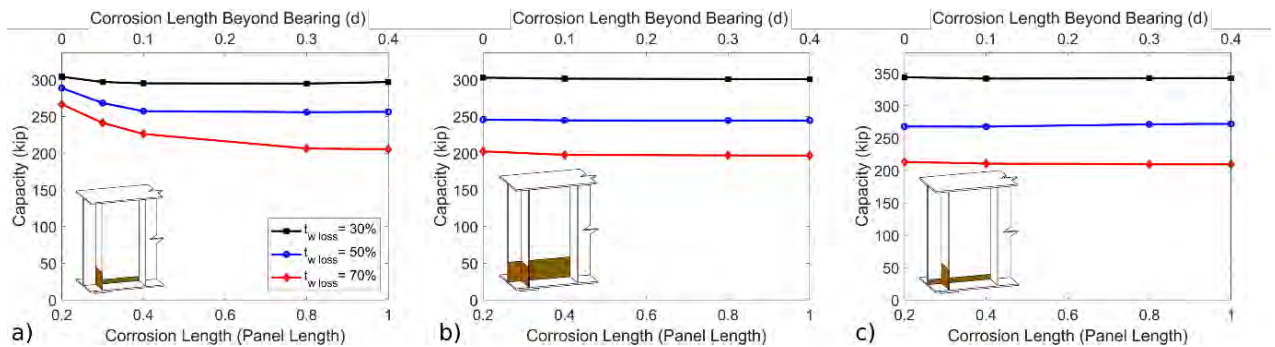


Figure 7.8: Effect of corrosion length for scenarios related to a) W2; and b-c) W3 patterns. Corrosion length had no effect to bearing capacity when exceeding bearing length by more than 10% of the depth. Dark- and light-brown shades represent minimum and maximum bounds of examined scenarios.

7.5.3 Web Corrosion Height Effect

In Fig. 7.9, the corrosion height is related to the residual capacity of beams with W1, W2, and W3 web corrosion patterns. For each case, the maximum corrosion height is defined in Table 4.1. Results highlight a common characteristic of the three examined patterns: the negligible impact of damage height (CH) beyond 10% of the depth. Another finding was that the corrosion height had reducing effect for increasing web section loss. Finally, similarly to the effect of corrosion length, the observed trends were consistent for varying stiffener section loss.

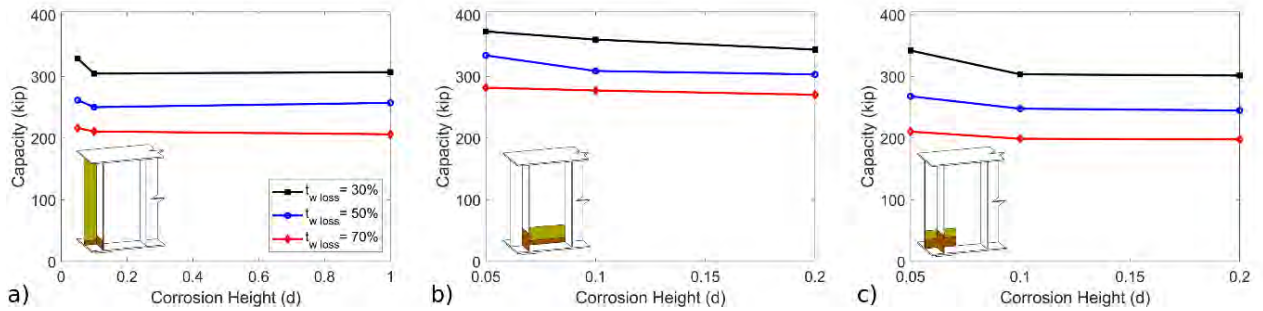


Figure 7.9: Effect of corrosion height for scenarios related to a) W1; b) W2; and c) W3 patterns. Corrosion height had no effect to bearing capacity when higher than 10% of depth; dark- and light-brown shades represent minimum and maximum bounds of examined scenarios

Notably, conclusions extracted from these results were representative trends for the behavior of corroded stiffened girders belonging to each one of the W1, W2, or W3 corrosion patterns. However, individual cases may deviate from this behavior, considering that beam end corrosion is a multi-parametric problem.

7.6 Failure Modes

The observed failure modes were mainly governed by the imported eigenmode, which was always characterized by large displacements at the weakest component between the corroded web and the stiffeners. Even though yielding usually initiated at the web above the inner edge of the bearing plate, it further expanded when the developed reaction force approached the bearing strength of the girder. In addition, the combination of the dense stiffeners spacing close to the supports as well as the magnitude of the imported eigenmodes prevented the first panels' shear failure for all of the examined scenarios.

8.0 Implementation and Technology Transfer

This section includes the proposed procedures that are the outcome of the research project. The structure of the section is as follows. First, the current procedures are presented and evaluated through a comparison to the experimentally and numerically obtained capacities. Second, the new procedures are presented in detail and the new equations are described, along with all the necessary information on how to apply them for different deteriorations. At the end of the section, the new procedures are evaluated following the same comparison to experimental and numerical results. The efficiency of the new results is demonstrated at the end of the section using the numerically obtained capacities from a new test data set that had not been previously used for the equations training.

8.1 Evaluation of Current Procedures

Before proceeding with the development of new procedures for deteriorated beam capacity, it is critical to evaluate the current MassDOT procedures. This evaluation included the following two steps for the specimens that were tested during this research project:

1. Follow the current MassDOT procedures and calculating the remaining capacity.
2. Compare the values from (1) with the experimentally obtained capacities.

8.1.1 Description of Current MassDOT Procedures

In the Commonwealth of Massachusetts, evaluation of beam ends with bearing stiffeners is conducted following the recommendations of Section 7.2.9.5 of the draft *MassDOT 2020 Bridge Manual (24)*.

The corroded end resistance at both the inventory and operating level is determined as follows:

$$R_{\text{yield}} = (\Phi_b = 1.0) (R_{n,\text{yield}}) \quad (8.1)$$

Based on the geometric configuration of the specimens that fall under the scope of the current research work (with overhang length $< 5k$), the nominal yielding capacity is calculated as follows:

$$R_{n,\text{yield}} = F_y A_g \quad (8.2)$$

Where:

F_y = minimum yield strength (ksi)

A_g = gross area remaining at bearing (in².)

The remaining gross area (A_g) considers the condition of web and stiffeners at the bottom 4 inches of the corroded end (Fig. 8.1) and is calculated as follows:

$$A_g = t_{ave} (N + 2.5k) + \sum \text{Bearing Stiffener Areas} - \sum \text{Hole Areas} \quad (8.3)$$

Where:

t_{ave} = average web remaining thickness (in.)

N = bearing length (in.)

k = distance from outer face of flange to toe of web fillet for a rolled shape, or toe of web to flange weld for a plate girder (in.)

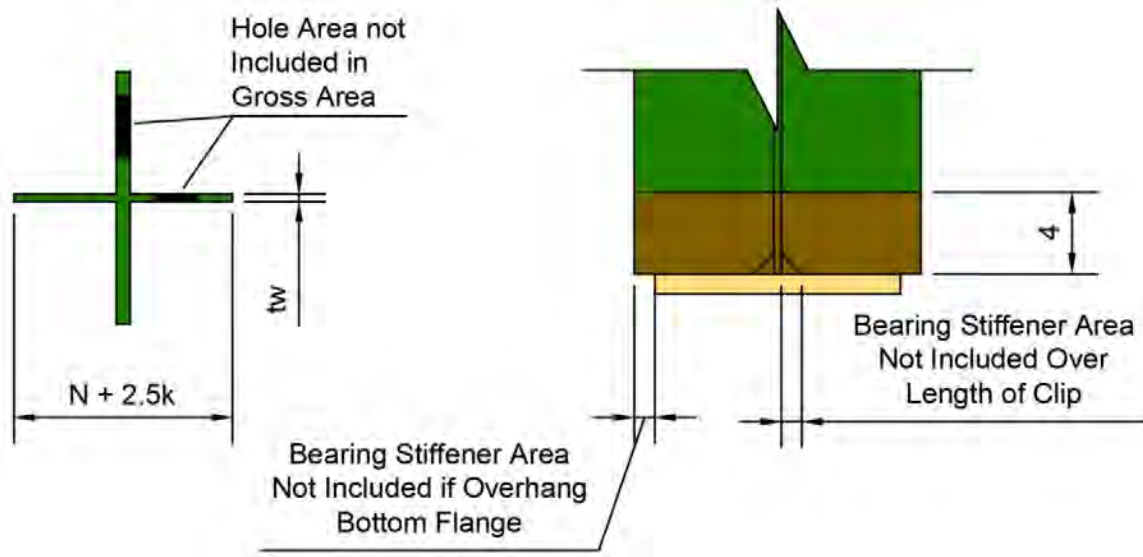


Figure 8.1: Domain for calculation of A_g , according to current provisions

8.1.2 Comparison between Experimental and Current Predicted Capacities

To calculate the failure load of the tested specimens according to the current procedures, the obtained point cloud data was employed to define the specimens' condition. Even though Fig. 8.2 depicts thickness contour maps fitted on the thickness values of more than 80,000 points emerging from the post-processing of point cloud data, both the proposed and the current analytical tools use a single value of remaining web thickness to grossly account for deterioration present at beam ends. However, given the nonuniformity of the remaining section profile, this poses a challenge to selecting the suitable corrosion input.

In the framework of this work, the average of the points located within the $N + 2.5k$ by 4 in. of the web was calculated and considered as the corrosion input (t_w). Regarding the stiffeners, they were welded to the beam for the experiment, and the nominal thickness was used.

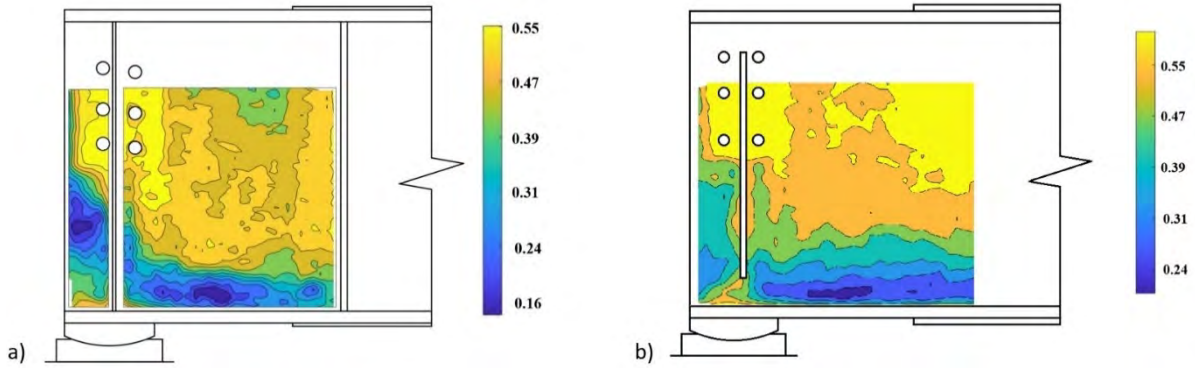


Figure 8.2: Contour maps depicting remaining thickness of Specimens a) A and b) B

Specimen A

Specimen A was a fully stiffened 24CB120 with the defining feature of a diagonal area of section loss above bearing, as well as initial web deviation from straightness at the same location. Stiffeners were 0.25 in. thick plated to resemble stiffeners with 50% section loss. The exact parameters used to calculate the unfactored nominal capacity according to the current procedures are given in Table 8.1.

Table 8.1: Parameters used for capacity calculation of Specimen A

	E (ksi)	Beam F_y (ksi)	Stif. F_y (ksi)				
	d (in)	t_w (in.)	t_r (in.)	k (in.)	N (in.)	L₀ (in.)	Stif. width (in.)
Material Properties	29.000	38	48				
Beam Geometry	24.31	0.556	0.93	1.63	7	0	5
	t _{rem} (in.)	H (in.)	t _s (in.)				
Corrosion	0.35	0	0.25				

It should be noted that the girder and the stiffeners had different material properties, given that they were manufactured more than 80 years apart. To evaluate an in-service girder, engineers would assume the minimum yield stress between all the girder's components as the input for the analytical estimation; however, in order to acquire a more representative overview of the equation capabilities, experimentally obtained strengths were used for web end stiffeners, as they were available from the team's previous work.

Following the procedure presented in 8.1.1, the beam strength equalled 300.9 kip, overestimating the experimentally obtained capacity (223.8 kip) by 34% (Table 8.2).

Table 8.2: Comparison between experimental and predicted capacity for Specimen A

Specimen 1	
Current MassDOT prediction (kip)	300.9
Experimental peak load (kip)	223.8

Specimen B

Specimen B was a partially stiffened 24CB120 in relatively good condition, with limited section loss mainly at the lower unstiffened web part. Considering that the stiffeners do not cover the whole depth, loads were not transferred between the stiffener plates and the flanges. Consequently, its classification lay toward the unstiffened girders, and the associated provisions were employed. Both the current analytical tools, as well as those proposed by the researchers, for capacity evaluation of rolled unstiffened girders with corroded ends can be found in (14). The exact parameters used to calculate the unfactored nominal capacity according to the current procedures are given in Table 8.3.

Table 8.3: Parameters used for capacity estimation of Specimen B

	E (ksi)	F_y (ksi)				
Material Properties	29.000	38				
	d (in)	t_w (in)	t_r (in)	k (in)	N (in)	L₀ (in)
Beam Geometry	24.31	0.556	0.93	1.63	7	0
	t _{rem} (in.)	H (in)				
Corrosion	0.4	0				

According to the current procedures, the nominal capacity of Specimen B was 129.2 kip and underestimated the experimental capacity by 25% (Table 8.4).

Table 8.4: Comparison between experimental and predicted capacity for Specimen B

Specimen A	
Current MassDOT prediction (kip)	129.2
Experimental peak load (kip)	172.3

8.1.3 Comparison between Numerically Obtained and Current Predicted Capacities

To gain better understanding of the efficiency of the current procedures, the predictions obtained according to the 2020 draft MassDOT *Bridge Manual* (24) were compared with selected results coming from the high-fidelity numerical model, under the assumption of uniform section loss. In cases where the examined corrosion scenario did not exceed the area over which the remaining web thickness (t_w) was calculated, the weighted average over the entire area was calculated. An example is given in Fig. 8.3, where a deterioration scenario with section loss 50 % of the intact web thickness is presented. Its length equals half of the area of interest; thus, the remaining thickness t_w in equation (8.3) will be 75% of the intact web thickness. The same methodology applies to stiffener remaining thickness calculation.

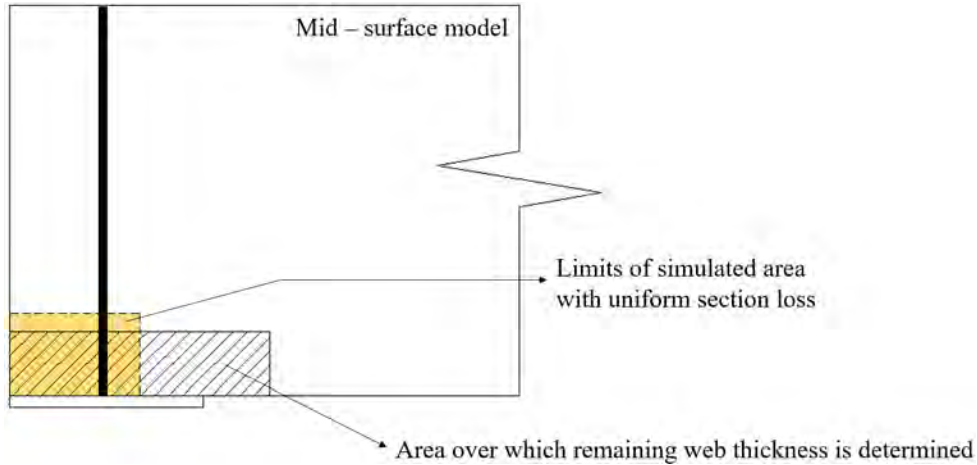


Figure 8.3: Beam end with corrosion scenario projected on bottom of web

Fig. 8.4 illustrates the predicted versus the computationally obtained capacities for numerous scenarios for each of the W1, W2, and W3 general corrosion patterns, while an overview of the examined beam geometries and corrosion characteristics is presented in Section 8.2.

The solid diagonal line denotes the finite element output and represents the perfect estimation. Each dot stands for the analytically obtained prediction of a unique scenario, making use of the current provisions. If a point lies above the solid line, the distance from the solid line provides the overestimating load, and vice versa. Having explained its structure, an emerging general remark is that the current procedures significantly overestimated the remaining capacity for the W1 general pattern, while for W2 and W3 cases, an overestimating tendency was observed for the lower half in the range of the obtained capacities, performing better to the upper half.

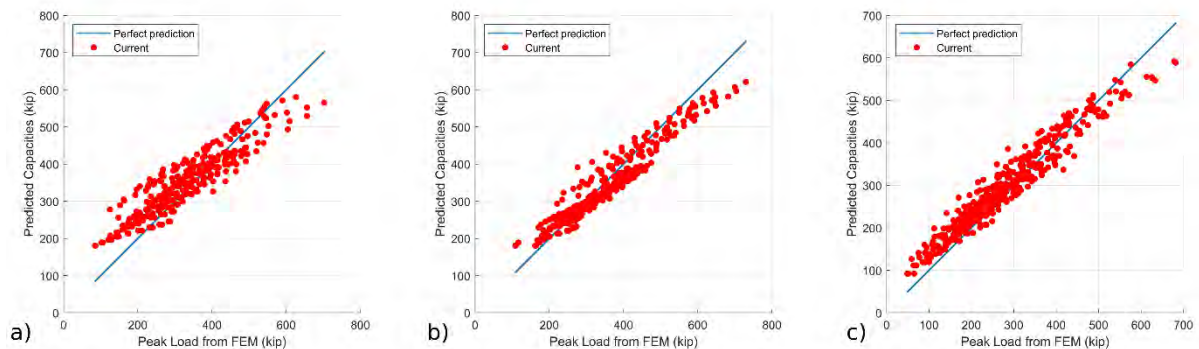


Figure 8.4: Comparison between predicted and computationally obtained capacities for current procedures, and a) W1; b) W2; and c) W3 general corrosion patterns (line represents perfect prediction; estimations lying above line overestimate actual strength)

To address the observed poor performance, especially for the W1 general corrosion pattern, new closed-form equations were developed based on the current procedures.

8.2 Proposed Procedures

A critical objective of this research was to develop simple equations that could be used by practicing engineers to determine the residual capacity of corroded girders containing stiffeners. To achieve this goal, empirical equations were developed to describe the relationship between corrosion characteristics and capacities of a sample consisting of more than 1,000 scenarios. The data presented in Section 7 was enriched with additional scenarios in the range of variability for the general corrosion patterns W1, W2, and W3, presented in Table 8.5. The simulated girder configuration on which the damage scenarios were projected is illustrated in Fig. 4.10, while the dimension characteristics of the three different variations are presented in Table 8.6. The efforts were focused on beams with overhang length less than $5k$, where k denotes the distance for the face of flange to web toe fillet, similar to the experimentally tested specimen for which the FEM was validated. Regarding material properties, even though structural steel type with 36 ksi yield stress was mainly used for steel bridge applications up to the 1970s, when the vast majority of the corroded stiffened girders in Massachusetts were built, analyses were also carried out for steel with yield stress equal to 48 ksi. To account for corrosion-induced web or stiffener deviation from straightness, imperfection amplitude equal to $1 t_{web}$ was considered for each scenario.

Table 8.5: Analytical description of examined corrosion patterns

No.	Pat.	CH (d)	CL (d)	t_{wloss}/t_{web}	CHs (d)	t_{sloss}/t_{stiff}
1	W1	0–20%	-	0–10%, 50–90%	-	-
2	W1	100%	-	30–80%	-	-
3	W2	0–20%	0–130%	20–80%	-	-
4	W3	0–16%	0–85%	40–80%	-	-
5	S1	-			0–25%, 100%	10–90%

Table 8.6: Design specifications of three employed geometries

	Geometry I	Geometry II	Geometry III
Depth (in.)	63.0	75.0	63.0
Web thickness (in.)	0.375	0.5	0.375
Stiffener width (in.)	6.0	5.0	5.0
Stiffener thickness (in.)	0.625	0.625	1.0

8.2.1 Equation Formulation

According to the current procedures, the residual bearing capacity of corroded stiffened girders is calculated on the basis of the yielding capacity, according to Eq. (8.2). Given that the failure modes observed in Section 7 of the current study initiated with localized yielding along the damaged locations, the current procedures constituted the starting point for the development of empirical equations that captured the residual bearing failure load. Figs. 7.5 and 7.6 highlight that stiffeners' section loss had a more deleterious effect compared to web section loss. Consequently, the first change modified the assumption of the current provisions that both the web and the stiffener equally contribute to the residual capacity. Analytically, this was expressed by separating the contributions from the yield strength of web and stiffeners into two distinct terms, as expressed in the following equation:

$$R_n = a F_y A_{stif} + b F_y A_{web} \quad (8.4)$$

Where, a and b are newly introduced constants, and A_{web} and A_{stif} denote the gross section of the web and stiffeners, respectively. Another point emerging from Fig. 7.5 was the relatively linear capacity response to stiffener section loss compared to the nonlinear relationship between strength and web section loss. This observation is encapsulated in Eq. (8.5) as follows:

$$R_n = a F_y A_{stif} + b (F_y A_{web})^c \quad (8.5)$$

Where, c is a newly added constant.

8.2.2 Corrosion Input

A key observation emerging from the computational work of Section 7 was the dimensions of the damage area that significantly affect the remaining capacity of the corroded girders. A corroded area that extended beyond 10% of the web and stiffener height or beyond 10% of the bearing length did not further decrease the girder strength. To incorporate these findings, the length of the web over which the A_{web} is calculated was modified from $N+2.5k$ to $N+0.1d$. Furthermore, the girder's condition at the bottom 4 inches of the web and stiffener was evaluated for capacity estimations. In terms of this study, the web and stiffener region that is located at the bottom 4 inches and extends between the outer bearing edge and 10% beyond the bearing length is referred to as the area of interest. To account for holes' existence along the web or the stiffeners within the area of interest, A_{web} and A_{stif} are defined in Eqs. (8.6) and (8.7), respectively (see also Figure 8.5).

$$A_{web} = t_w (N + 0.1d) - \sum \text{Web hole areas} \quad (8.6)$$

Where, t_w is the remaining web thickness for each one of the general web corrosion patterns, as defined in Fig. 8.5.

$$A_{stif} = 2 t_s b_s - \sum \text{Stiffener hole areas} \quad (8.7)$$

Where, t_s denotes the remaining stiffener thickness within the 4 bottom inches, and b_s is the stiffener width.

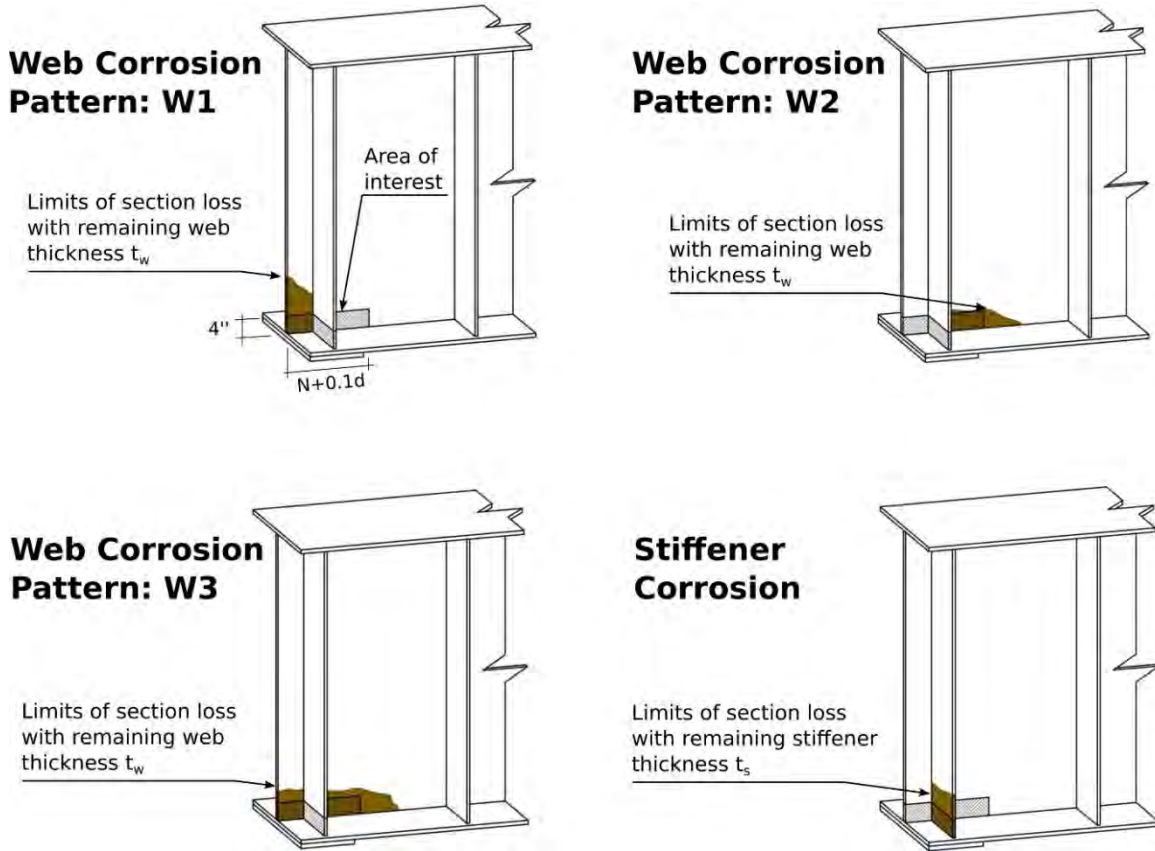


Figure 8.5: Parameters for capacity calculation according to proposed equations

8.2.3 Equation Fitting

Least squares analysis was performed to fit the computationally obtained data points to the nonlinear model in Eq. (8.5). In this framework, the obtained capacities were set as the dependent variable, while $F_y A_{web}$ and $F_y A_{stif}$ were considered as the independent variables. Three different sets of the constants a , b , and c were derived and are presented in Table 8.7 for each of the general corrosion patterns W1, W2, and W3. Furthermore, Fig. 8.6 illustrates the predicted versus the computationally obtained capacities for the employed training sets, highlighting that for the three studied patterns, the predicted capacities lay close to the solid diagonal line that represents the perfect estimation. Within the same figure, capacities obtained making use of the current procedures are also included. A general remark is that the proposed provisions significantly improved the response for the W1 general pattern, while they provided more accurate estimations for the W2 and W3 patterns.

Table 8.7: Parameters emerging nonlinear regression for Eq. 8.6

Pattern	W1	W2	W3
a	1.33	1.46	1.00
b	0.55	1.16	0.21
c	1.48	0.93	1.23

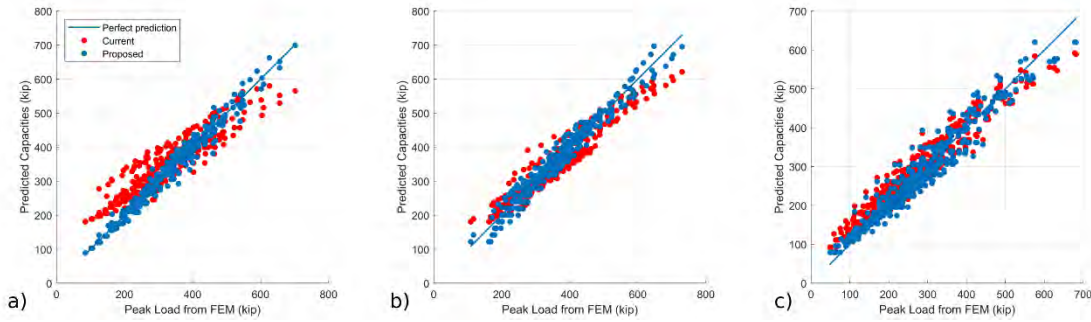


Figure 8.6: For training set, comparison between predicted and computationally obtained capacities for a) W1; b) W2; and c) W3 general corrosion patterns (line represents perfect prediction, while blue and red points depict estimation according to proposed and current provisions)

Interesting observations can be also drawn from the derived parameters values presented in Table 8.7. In detail, for the proposed provisions and the general patterns W1 and W2, where the actual web condition is analytically underestimated by considering the remaining web thickness t_w of the damaged area representative for the whole web area of interest, the stiffeners' contribution is significantly increased with a values in the range between 1.33 and 1.46. On the other hand, for the W3 pattern, where the damage extends along both sides of the bearing stiffeners, t_w reflects the actual web condition and a is equal to unit.

Other equation forms were also examined but did not result in significant gains with respect to accuracy, so the proposed equation was adopted for its simplicity and direct relationship to the parameters contributing to strength (deteriorated web and stiffeners).

8.3. Evaluation of Proposed Procedures

8.3.1 Comparison between Experimental and New Predicted Capacities

Specimen A

The trained equations were combined with 3D laser scanning to evaluate the remaining capacity of Specimen A. It should be recalled that the stiffeners were welded to the girder before testing. As a result, the naturally developed corrosion topology along the web of the tested end did not directly fall into one of the assumed general corrosion patterns W1, W2, or W3. However, by considering that the web had experienced at least 25% section loss at both sides of the bearing stiffeners, the W3 general pattern and the associated parameters presented in Table 8.7 were selected to describe the girder's condition.

By averaging the scanned data along the whole area of interest, due to the W3 pattern, the remaining thickness was found equal to 0.35 inch, which corresponded to bearing capacity of 180.3 kip (Table 8.8). Summarizing, the current procedures overestimate the actual capacity by 25%, while the proposed equations underestimate it by 20%. These results not only provide credibility to the developed equation but also constitute a first sign of its robustness,

since it was developed for plate girders with at least twice the depth of the examined specimen.

Table 8.8: Comparison between experimental and analytical prediction predictions for Specimen A

	Experimental	Current Procedure	Proposed Procedure
Capacity (kip)	223.8	279.9	180.3

Specimen B

Specimen B was evaluated by making use of provisions for unstiffened girders which were not considered relevant to the scope of this work. However, for the sake of completeness, equations previously developed by the researchers (14) were employed to estimate the strength of Specimen B (Table 8.9).

Table 8.9: Comparison between experimental and analytical prediction predictions for Specimen B

	Experimental	Current Procedure	Proposed Procedure
Capacity (kip)	172.3	129.3	171.1

8.3.2 Analytical Provisions and 3D Scanning.

Even though the previously mentioned results demonstrated a significantly improved response of the developed procedures, researchers and engineers should be very cautious regarding 3D laser scanning implementation with analytical provisions. A previous research work by the authors on rolled unstiffened girders (17) revealed that averaging all the points within the area of interest may result in overly optimistic capacity predictions. This behavior was attributed to the fact that if a subdomain in critical condition is present within the area of interest, it can potentially define the beam end's failure. Thus, by taking into account the whole area, it is possible to underrate its deleterious effect.

Nevertheless, that does not seem to be the case for the examined specimen. Observation of the remaining thickness profile within the areas of interest (Fig. 8.2a) indicated that maximum section loss was observed at the right side of the bearing stiffener. However, the failure mode was governed by large displacements developed at the outer part of the web, following the pre-loading web deviation from straightness at that location. These observations provided strong evidence that the significantly overestimating prediction obtained by the current provisions does not emerge from the remaining thickness input but is in compliance with the overall overestimating tendency noticed in Fig. 8.4.

In short, the current experiment provided additional data points to the argument that the critical feature of a corroded end defines its failure mode and load. Consequently, engineering judgement is always a requirement for the equations' implementation, regardless of the equipment employed for the remaining thickness estimation.

8.3.3 Comparison between Numerically Obtained and New Predicted Capacities

To validate the efficiency of the proposed provisions, a series of simulations that were not part of the training set were conducted. For the W1 general corrosion pattern, analyses were run for 36 ksi steel and the beam configuration labeled as Geometry II in Table 8.6. For the W2 pattern, the same beam configuration was used, but 48 ksi steel was used to evaluate the procedures' robustness to varying material properties. Finally, for the W3 general corrosion pattern, Geometry II was combined with 36 ksi steel. The capacities depending on corrosion scenario are presented in Fig. 8.7.

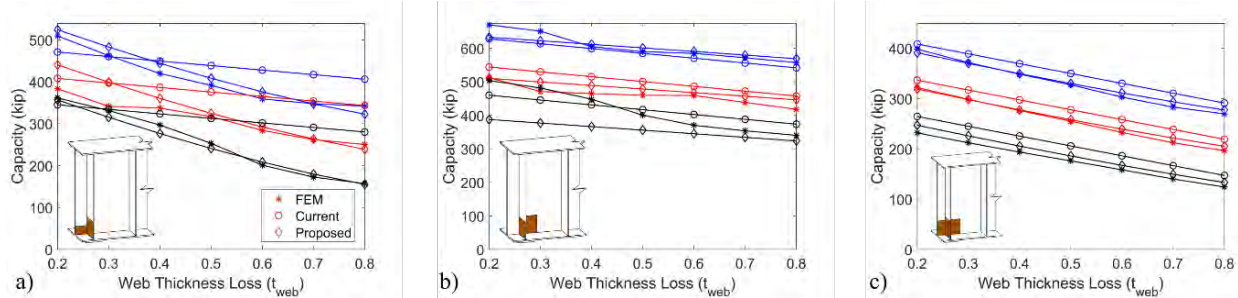


Figure 8.7: Comparison between predicted failure loads and numerical results (blue, red, and black denote 30%, 50%, and 70% stiffener section loss, respectively)

Results highlight the general accuracy of the proposed equation in comparison with the finite element simulation of the proposed equations for the three examined corrosion patterns. It is worth noting that for most of the cases, the current procedures overestimated the capacity predicted by the FEMs. On the other hand, the proposed equation provided significantly improved estimations. To quantify the predictions deviation from the actual capacities, both procedures were evaluated with the mean squared error (MSE), defined as:

$$MSE = \frac{1}{n} \sum_{i=1}^n (y_i - \hat{y}_i)^2 \quad (8.7)$$

Where:

y_i : experimentally obtained capacity of the i th specimen

\hat{y}_i : predicted capacity according to the current or the proposed provisions for the i th specimen

n : number of specimens

Making use of Eq. (8.7), the predicted capacities according to the developed equation resulted in an 89% error reduction for patterns W1 and W3 when compared with current rating equations. For corrosion scenario W2, even though the proposed equation provided more accurate estimations for the 30% and 50% stiffener section loss, the overall MSE value was increased by 73% due to the conservative estimations for stiffener section loss equal to 70% (black lines in Fig. 8.7b). However, for the 30% and 50% stiffener section loss, the proposed equations provided more accurate estimations.

This page left blank intentionally.

9.0 Conclusions

This research project focused on plate girders with corroded beam ends, which are commonly found in the Commonwealth of Massachusetts because of aging and deterioration. The goal of the study was to investigate the efficiency and accuracy of the current procedures for the bearing capacity assessment of deteriorated stiffened ends. The most important outcome of this work is the new set of equations, which are provided in Section 8. Several interesting findings from all the phases of the work are presented in this section.

9.1. Phase I: Most Common Corrosion Topologies—Data Collection

Thirty inspection reports of bridges with beam end deterioration and 210 corroded stiffened ends were examined in detail. Based on this real data, numerous parameters were defined and quantified through an extensive statistical analysis. The main findings from Phase I are as follows.

Corrosion Topologies:

- Two main configurations were identified at the support area: beams with one or two bearing stiffeners per web face.
- Corrosion patterns were provided for both configurations, which describe the usual deterioration condition for the web and the bearing stiffeners.
- The leaking water flow restrictions due to the stiffeners' existence might result to the significantly high population of beams with web holes (64% of the examined beam ends).
- For beam ends with two bearing stiffeners per web face, no significant variation was noticed between the inner and the outer stiffeners.
- Similarities at the corrosion topologies of beams with one or two bearing stiffeners were noticed.
- For the numerical analysis, the corrosion scenarios were projected on plate girders with depth approximately in the range of 58 in. to 70 in., as it represents the vast majority of stiffened girders.

Inspection Methods:

- It was observed that there is currently a lack of a comprehensive and unified inspection protocol among the MassDOT districts as well as among inspection engineers.
- Usually there are no more than one or two web thickness measurements reported per corroded end.
- No data are usually reported for stiffeners' condition.

9.2. Phase II: Experimental Testing

Full-scale laboratory testing was conducted on two 4-inch-deep specimens built on two naturally corroded rolled girders obtained from a decommissioned bridge in Massachusetts. The first specimen was designed and fabricated to resemble plate girders by welding full-depth stiffeners and creating two web panels along the deteriorated end. Partial stiffeners were welded to the second girder to study the effect of plates found in the field for diaphragm connections. The experimental configuration was designed to laterally restrict the top flange, mimicking in-service conditions and ensuring that failure occurred at the corroded end. The load was applied upward to the tested end, resembling the developed reaction force. The specimen was vertically restricted by a crossbeam placed on the top flange approximately 4 feet from the tested end. This configuration served two purposes: it ensured that the failure was shear dominated and that more than 75% of the load was distributed to the studied end. The main findings of Phase II are as follows.

- Both specimens were scanned, making use of a 3D laser scanner, and the obtained point clouds were post-processed to develop contour maps depicting the remaining web thickness along the web of the tested end. Both specimens showed similar corrosion-induced damage, probably governed by the in-service configuration.
- Regarding the experimentally obtained failures, both specimens were characterized by instant capacity drop governed by large displacements developed at peak load. For the partially stiffened end, the web deflection profile reflected the initial imperfect geometry due to pre-loading web deviation from straightness, combined with significant deformations at the bearing stiffeners, designed to resemble members with 50% section loss. For the second specimen, large displacements were mainly observed at the unstiffened part of the web's bottom.
- The analytical provisions currently in use by MassDOT encapsulate the corrosion effect on a damaged end with a unique value describing the gross area above the support. Since bearing stiffeners with uniform sections had been welded at the tested girder, the challenge rested with determining the thickness value describing the remaining web section. For both specimens, the average thickness of the points located within the defined area of interest obtained with 3D laser scanning was calculated. For the stiffened specimen, the numerically obtained capacity overestimated the actual one by 24%, while for the partially stiffened one, analytical provisions provided an estimation that was 25% lower.
- All experimentally observed failures had a common characteristic, **the lateral deflection of the web at peak load**, which indicated a buckling-related failure mechanism.

9.3. Phase III: Computational Results— Parametric Analysis

The experimentally obtained data were used to calibrate a high-fidelity numerical model capable of predicting the capacity of girders with stiffened ends. The numerous aspects of the calibration for the numerical modeling are included in Section 4. Furthermore, experimental data obtained from the literature were also used to validate the composite action generated by the interaction between shear studs and concrete decks. The model generation, under the combination of the validated assumption, as well as the post-processing were automated by combining Python programming language and Abaqus FEA software. This technique remarkably increased the efficiency of the available computational capacity, allowing the researchers to conduct an extensive parametric analysis simulating and analyzing thousands of combinations of corrosion topologies for several beam types and lengths. The scenarios computationally analyzed came from the corrosion topologies identified in Phase I of this work, under the assumption of uniform thickness loss. The main findings of Phase III are as follows.

- **The project team analyzed a total of more than 1,000 models** accounting for three distinct general corrosion patterns. The results were processed, and the peak loads of the beams ends were recorded.
- The computational model assumptions were based on experimental observations. The project team built a high-fidelity computational model that is capable of predicting accurately the capacity of corroded beam ends.
- The design characteristics of the plate girders over which the examined corrosion scenarios were projected were mined from construction drawings of deteriorated bridges from Massachusetts. The first two web panels along each end were spaced every half times the girder's depth. For the remaining panels, their length was doubled. Probably due to this design, and for the total of the examined scenarios, no panel failure was observed.
- The initial geometric imperfection had a slight effect on the numerically obtained capacities. This finding was consistent with the literature of plate buckling and stiffened plate buckling. Stiffened plates are generally less imperfection-sensitive than unstiffened plates. Thus, this finding was different than the finding for the effect of initial web deviation from straightness for unstiffened rolled girders.
- The stiffeners' section loss was found to have a very harmful effect on the bearing strength compared to web thickness loss, highlighting the need for extensive bearing stiffener condition documentation for field girders.
- For the examined corrosion patterns where the damage area initiated from the base of the web and the stiffeners, the web and stiffener corrosion height had no effect on the bearing capacity when the height exceeded 10% of the depth. The web corrosion length had no effect on the bearing capacity when it exceeded the bearing length by more than 10% of the depth.

9.4. New Procedures: Final Outcome

Taken altogether, the current procedures presented a significant overestimating tendency for deterioration scenarios in compliance with one out of the three examined general corrosion patterns. Building on the current procedures and by integrating findings from Phase III of this study, the project team proposed new closed-form equations for the capacity estimation of plate girders with corroded ends. The proposed modifications regard three main aspects:

1. The linearity of the equation
2. The area over which the beam condition is examined
3. The remaining thickness calculation

A set of parameters was proposed for each of the three examined general corrosion patterns. It is worth noting that the evaluation of the proposed procedures based on numerical end experimental data highlighted demonstrated improved efficiency and reduced errors compared to the equations currently in use.

10.0 Limitations and Future Work

The methodology of this work emerges from real corrosion data and acts complementary to a previous work by the authors aiming to address the remaining capacity of rolled girders with corroded ends. Experimentally, the investigation efforts were focused on the girder, while the deck contribution was simulated by the applied boundary conditions. On the other hand, computational models accounted for plate girders with composite decks. However, none of the approaches captured additional stiffness emerging from the diaphragm behavior. This is an area for future work. Future studies will have to examine the behavior of the corroded beams as part of the whole bridge and the potential redistribution of forces after the failure (or even the loading) of one beam end. The system behavior of the bridge is hugely important, and it is expected to provide more capacity, although this remains to be validated.

To analytically evaluate the capacity of the tested specimens, thickness estimations were derived by averaging the thickness output of point cloud data above the bearing. Even though the resulting capacities were close to the experimental failure loads, the use of the average thickness needs to be further investigated.

It is worth noting that the proposed equations emerge from the relationship between corrosion characteristics and bearing failure load of a sample consisting of more than 1,000 simulated scenarios of plate girders. On the other hand, stiffened rolled girders typically found in girder bridges have increased web thickness and reduced slenderness ratio compared to the range of the computationally examined scenarios in the framework of the current research. Consequently, even though the conducted experiment provided evidence that the proposed equations apply for rolled stiffened beams, additional data points are required.

This page left blank intentionally.

11.0 References

1. 2021 Report Card for America's Infrastructure. <https://infrastructurereportcard.org>.
2. Massachusetts Dept. of Transportation. *MassDOT Bridge Inspection Handbook*. Highway Division Bridge Section, 2015.
3. Kayser, J. R., and A. S. Nowak. Capacity Loss Due to Corrosion in Steel-Girder Bridges. *Journal of Structural Engineering*, Vol. 115, 1989, pp. 1525–1537.
4. Van de Lindt, J. W., and T. M. Ahlborn. *Development of Steel Beam End Deterioration Guidelines*. Publication MDOT-RC-1454. Michigan Tech Transportation Institute, 2005.
5. Sugimoto, I., Y. Kobayashi, and A. Ichikawa. Durability Evaluation Based on Buckling Characteristics of Corroded Steel Deck Girders. *Quarterly Report of Railway Technical Research Institute*, Vol. 47, 2006, pp. 150–155.
6. Kim, I. T., M. J. Lee, J. H. Ahn, and A. Kainuma. Experimental Evaluation of Shear Buckling Behaviors and Strength of Locally Corroded Web. *Journal of Constructional Steel Research*, Vol. 83, 2013, pp. 75–89.
7. Ahn, J. H., J. H. Cheung, W. H. Lee, H. Oh, and I. T. Kim. Shear Buckling Experiments of Web Panel with Pitting and Through-Thickness Corrosion Damage. *Journal of Constructional Steel Research*, Vol. 115, 2015, pp. 290–302.
8. Ahn, J. H., I. T. Kim, S. Kainuma, and M. J. Lee. Residual Shear Strength of Steel Plate Girder Due to Web Local Corrosion. *Journal of Constructional Steel Research*, Vol. 89, 2013, pp. 198–212.
9. Khurram, N., E. Sasaki, H. Katsuchi, and H. Yamada. Experimental and Numerical Evaluation of Bearing Capacity of Steel Plate Girder Affected by End Panel Corrosion. *International Journal of Steel Structures*, Vol. 14, 2014, pp. 659–676.
10. Ahn, J. H., S., Kainuma, and I.T. Kim. Shear Failure Behaviors of a Web Panel with Local Corrosion Depending on Web Boundary Conditions. *Thin-Walled Structures*, Vol. 73, 2013, pp. 302–317.
11. Usukura, M., T. Yamaguchi, Y. Suzuki, and Y. Mitsugi. Strength Evaluation for a Corroded Damaged Steel Girder End Considering its Collapse Mechanism. Proceedings of the 13th East Asia-Pacific Conference on Structural Engineering and Construction (EASEC), 2013.
12. Liu, C., T. Miyashita, and M. Nagai. Analytical Study on Shear Capacity of Steel I-Girders with Local Corrosion Nearby Supports. *Procedia Engineering*, Vol. 14, 2011, pp. 2276–2284.
13. Yamaguchi, E., and T. Akagi. Degradation of Load-Carrying Capacity of Steel I-Girder End due to Corrosion. Proceedings of the 13th East Asia-Pacific Conference on Structural Engineering and Construction (EASEC), 2013.
14. Tzortzinis, G., S. Gerasimidis, S. Brena, and B. Knickle. *Development of Load Rating Procedures for Deteriorated Steel Beam Ends: Deliverable 4*. Tech Report 19-008. University of Massachusetts Transportation Center, 2019.
15. Tzortzinis, G., B. T. Knickle, A. Bardow, S. F. Breña, and S. Gerasimidis. Strength Evaluation of Deteriorated Girder Ends. I: Experimental Study on Naturally Corroded I-Beams. *Thin-Walled Structures*, Vol. 159, 2021, p. 107220.

16. Tzortzinis, G., B. T. Knickle, A. Bardow, S. F. Breña, and S. Gerasimidis. Strength Evaluation of Deteriorated Girder Ends. II: Numerical Study on Corroded I-Beams. *Thin-Walled Structures*, Vol. 159, 2021, p. 107216.
17. Tzortzinis, G., C. Ai, S. F. Breña, and S. Gerasimidis. Using 3D Laser Scanning for Estimating the Capacity of Corroded Steel Bridge Girders: Experiments, Computations and Analytical Solutions (Under Review).
18. *Code of Federal Regulations*. <https://www.gpo.gov/fdsys/pkg/CFR-2012-title23-voll1/pdf/CFR-2012-title23-voll1-sec650-311.pdf>. Accessed June 14, 2021.
19. *ABAQUS, User's Guide*. Dassault Systems Simulia Corporation, Providence, RI, 2014.
20. Barth, K. E., and H. Wu. Efficient Nonlinear Finite Element Modeling of Slab on Steel Stringer Bridges. *Finite Elements in Analysis and Design*, Vol. 14, 2006.
21. Mans, P. H. Full Scale Testing of Composite Plate Girders Constructed Using 70-ksi High Performance Steel. Master's thesis, University of Nebraska, 2001.
22. American Association of State Highway and Transportation Officials. *Standard Specifications for Highway Bridges*. 1965.
23. Nagaraja Rao, N. R. *Material Properties of Structural Carbon and High-Strength Steels*. Fritz Laboratory Reports, 1963.
24. Massachusetts Dept. of Transportation. *Draft LRFD Bridge Manual, Part I*. Highway Division Bridge Section, 2020.

12.0 Appendix

12.1 Appendix A: Detailed Data and Processing Graphs for Beam Ends with One Bearing Stiffener

W1 Corrosion Pattern

Corrosion height (CH_1) is the unique geometric characteristic of the W1 pattern, which describes web section loss at the domain between the stiffener and the beam end. Fig. 12.1 presents the CH_1 distribution of the recorded cases. Two main trends are observed, beams with full height corrosion and beams with deterioration up to the lower 20% of the web depth.

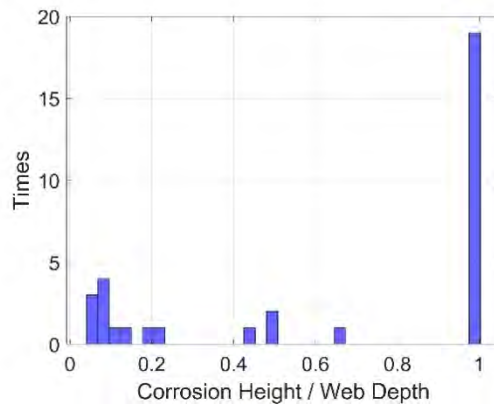


Figure 12.1: Corrosion height distribution for W1 pattern

Fig. 12.2 displays the web section loss for these two trends. The available recordings cover a range between 50% and 90% of the nominal intact thickness for the beams with corrosion at the web bottom, and 30% to 80% for beams with full height corrosion.

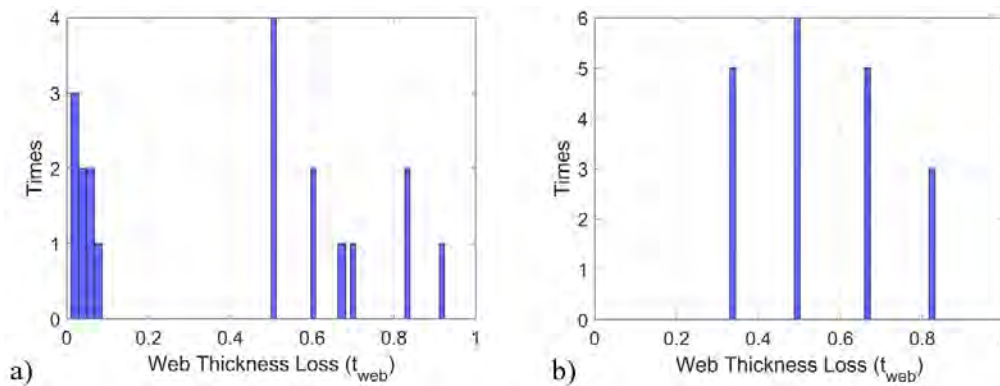


Figure 12.2: Web thickness loss distribution for W1 cases with a) deterioration up to 20% of web depth, and b) full height corrosion

Web Holes

H1 is the most commonly associated web hole pattern for the W1 web corrosion scenario. The corresponding holes lengths and heights of the areas with 100% section loss are presented in Fig. 12.3 and reveal that the holes were mainly limited at the 7% of the web bottom. However, there was the extreme case of 68% of web depth for hole height.

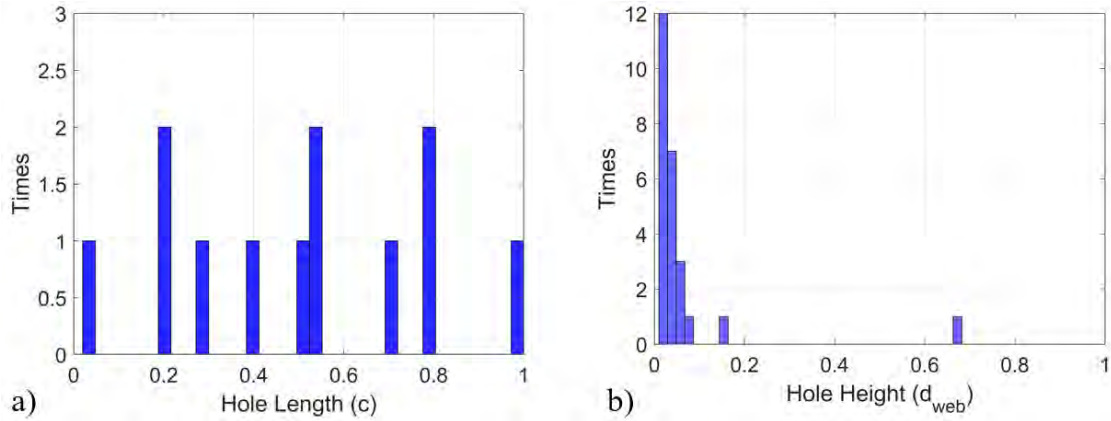


Figure 12.3: a) Length and b) height of W1 web corrosion pattern for beams with one stiffener per web face

According to Table 5.1, the H4 hole pattern was found six times, four times in combination with H1 and two times as a unique case. The H4 topological characteristics (Fig. 12.4) reveal that the hole is mainly found at the top of the web and covers up to 5% of the web depth.

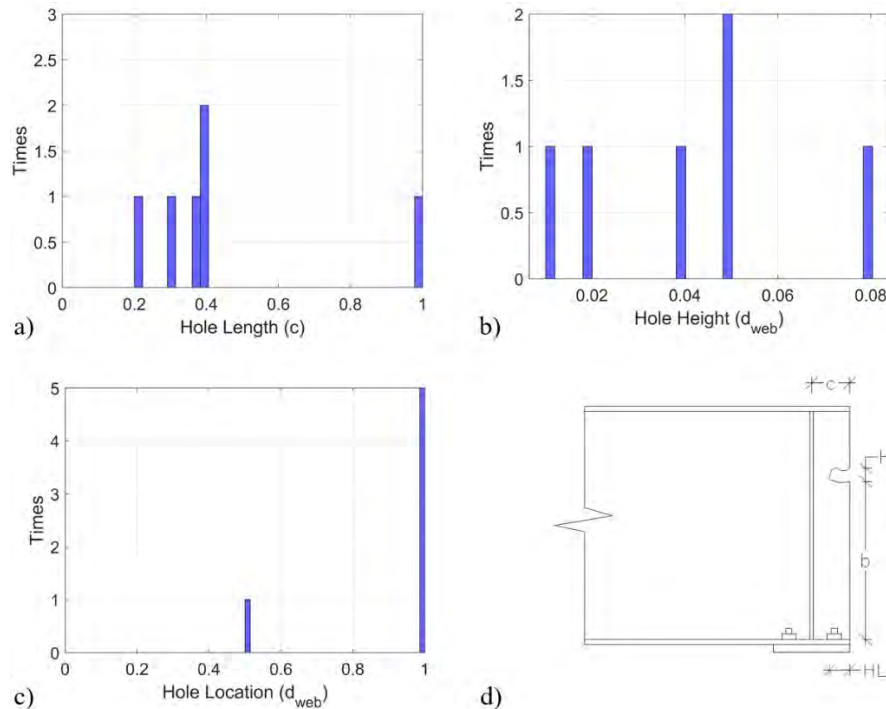
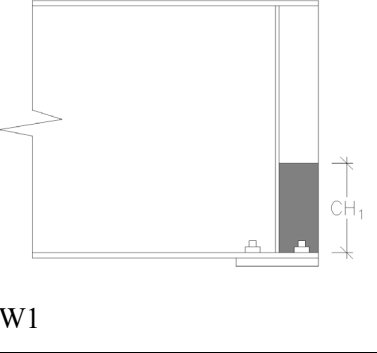
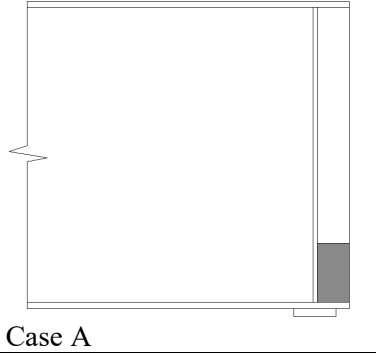
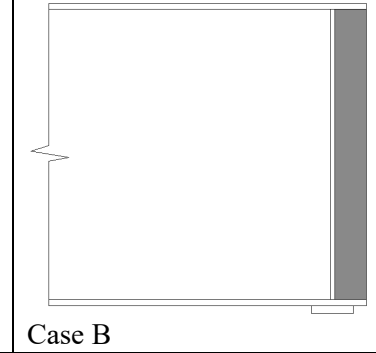
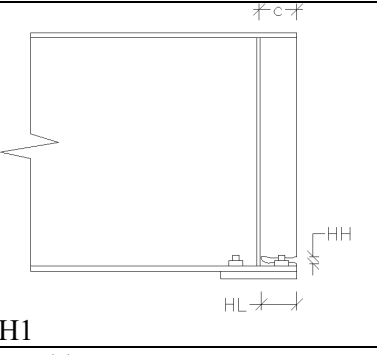
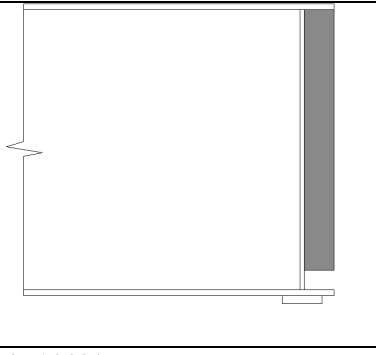
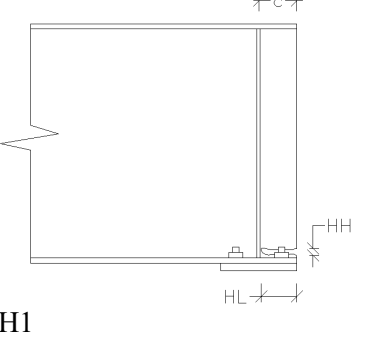
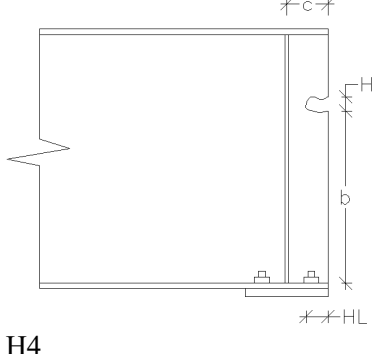
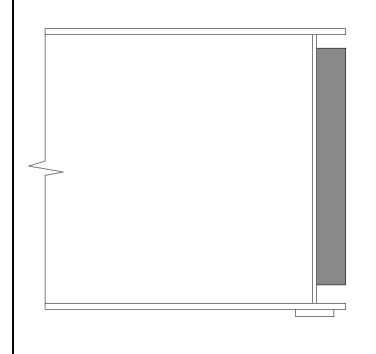


Figure 12.4: a) Hole length; b) height; c) distance from the bottom flange; and d) nomenclature of H4 pattern

Table 12.1, summarizes the most common corrosion topologies for the W1 pattern.

Table 12.1: Dimension of most common deterioration scenarios for W1 web corrosion pattern and associated holes

		
W1	Case A	Case B
CH ₁ (d _w)	0–20%	100%
tW _{loss} (t _{web})	0–10%, 50–90%	30–80%
		
H1		
HL (c)	0–100%	
HH (d _w)	0–7%	
		
H1	H4	
HL (c)		0–100%
HH (d _w)		0–7%
	HL (c)	0–100%
	HH (d _w)	0–5%
	c (d _w)	100 %

W2 Corrosion Pattern

Corrosion height (CH_1) and length (CL_1) are the two geometric characteristics of the W2 pattern, which describes a damaged area at the web bottom in front of the bearing stiffener. Fig. 12.5 presents the distribution of the recorded corrosion dimensions as well as the corresponding section losses. From Fig. 12.5b, it can be interpolated that corrosion length is not so commonly documented compared to the corrosion height. However, the available data mainly depict short areas (up to $0.1 d_w$) that expand long ($0.5-1.3 d_w$) along the longitudinal beam axis.

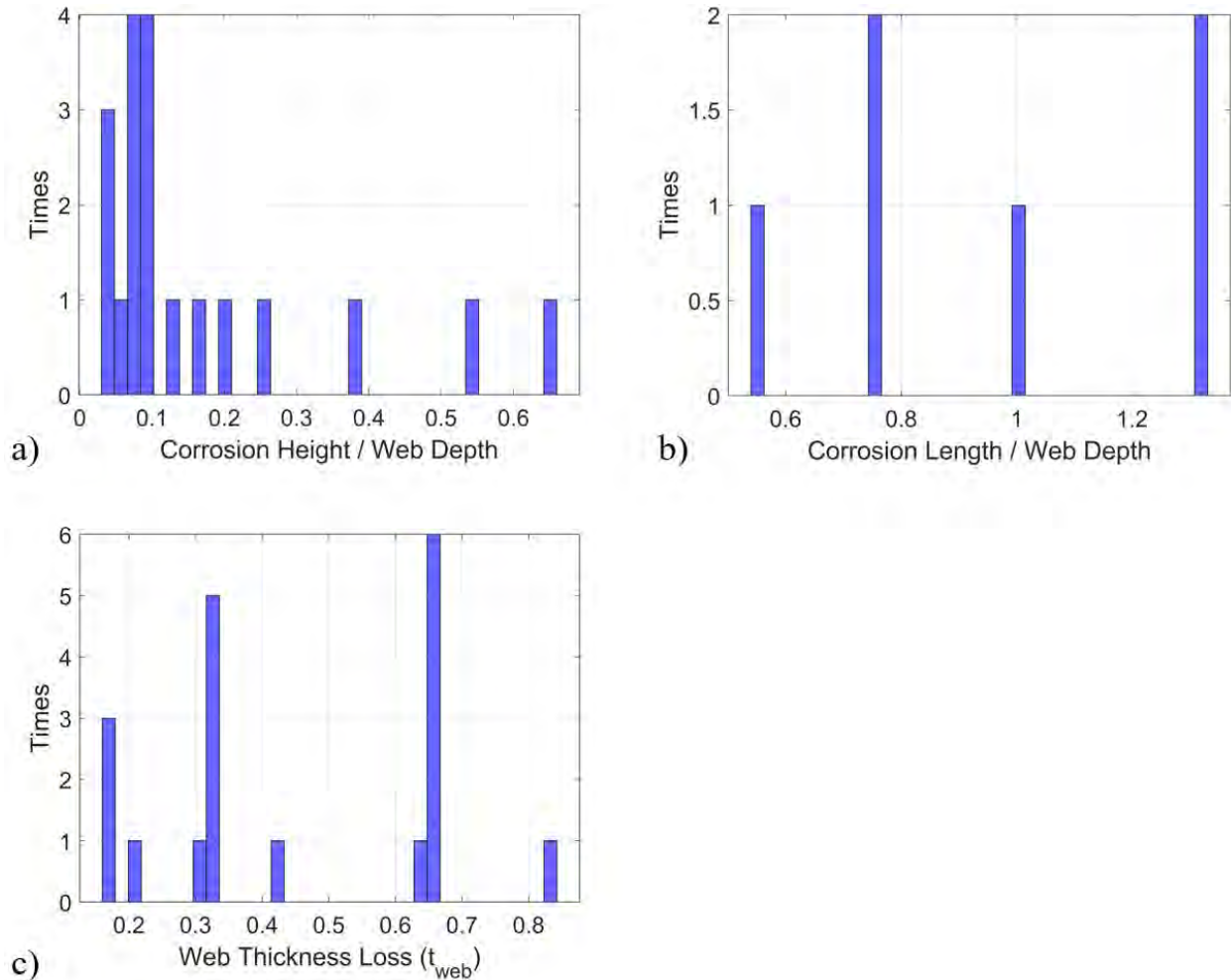


Figure 12.5: Distribution of deterioration characteristics for W2 corrosion scenario for beams with unique stiffener above bearing

Web Holes

The H2 pattern is the only hole scenario with boundaries entirely within the W2 web deterioration pattern and, consequently, the unique hole pattern associated with it. Hole morphology seems to follow the trend of the web deterioration, formulating short holes initiating from the web–stiffener intersection and expanding along the longitudinal axis (Figure 12.6).

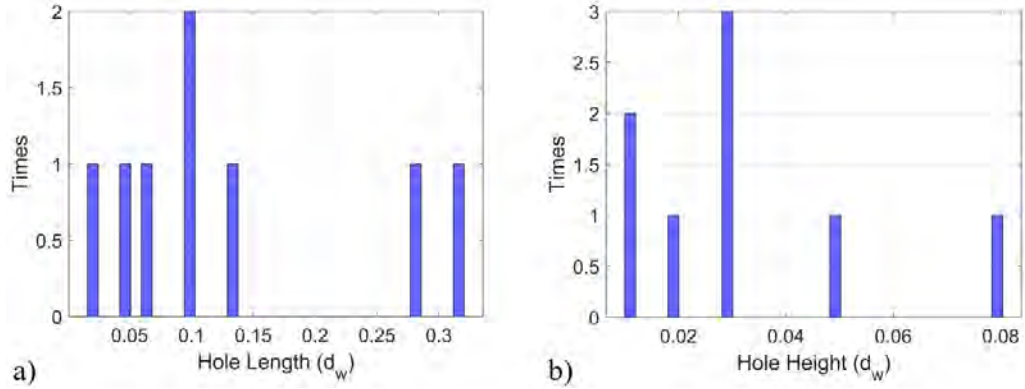
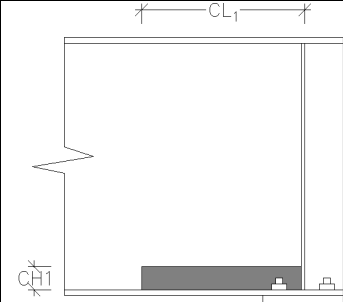
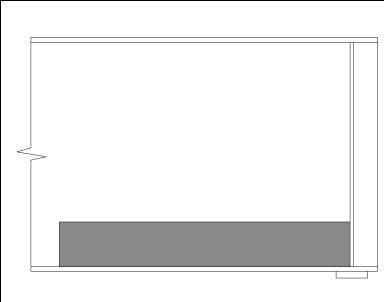
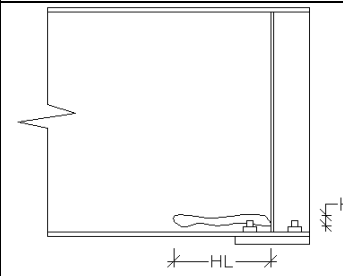
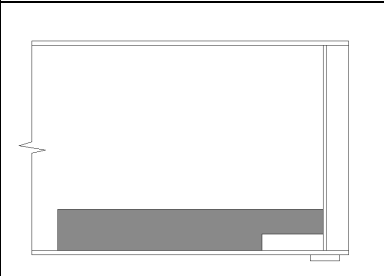


Figure 12.6: a) Length and b) height of H2 holes associated with W2 web corrosion pattern for beams with unique stiffener above bearing

Table 12.2 summarizes the most common section loss and hole topologies for the W2 pattern.

Table 12.2: Dimension of most common deterioration scenarios for W2 web corrosion pattern and associated holes

	
W2	
CH_1 (d_w)	0–20%
CL_1 (d_w)	0–130%
$t_{W_{loss}}$ (t_{web})	20–80%
	
H2	
HL (d_w)	0–30%
HH (d_w)	0–8%

W3 Corrosion Pattern

Corrosion height (CH_1) and length (CL_1) are the two geometric characteristics of the W3 pattern, which describes a damaged area on web equally high along both sides of the stiffener. The area between the stiffener and the web edge is considered deteriorated along the whole length. Fig. 12.7 presents the distribution of the 10 recorded corrosion dimensions and the corresponding section losses. The available data present short areas (up to $0.15 d_w$) that expand long (up to $0.8 d_w$) along the longitudinal beam axis.

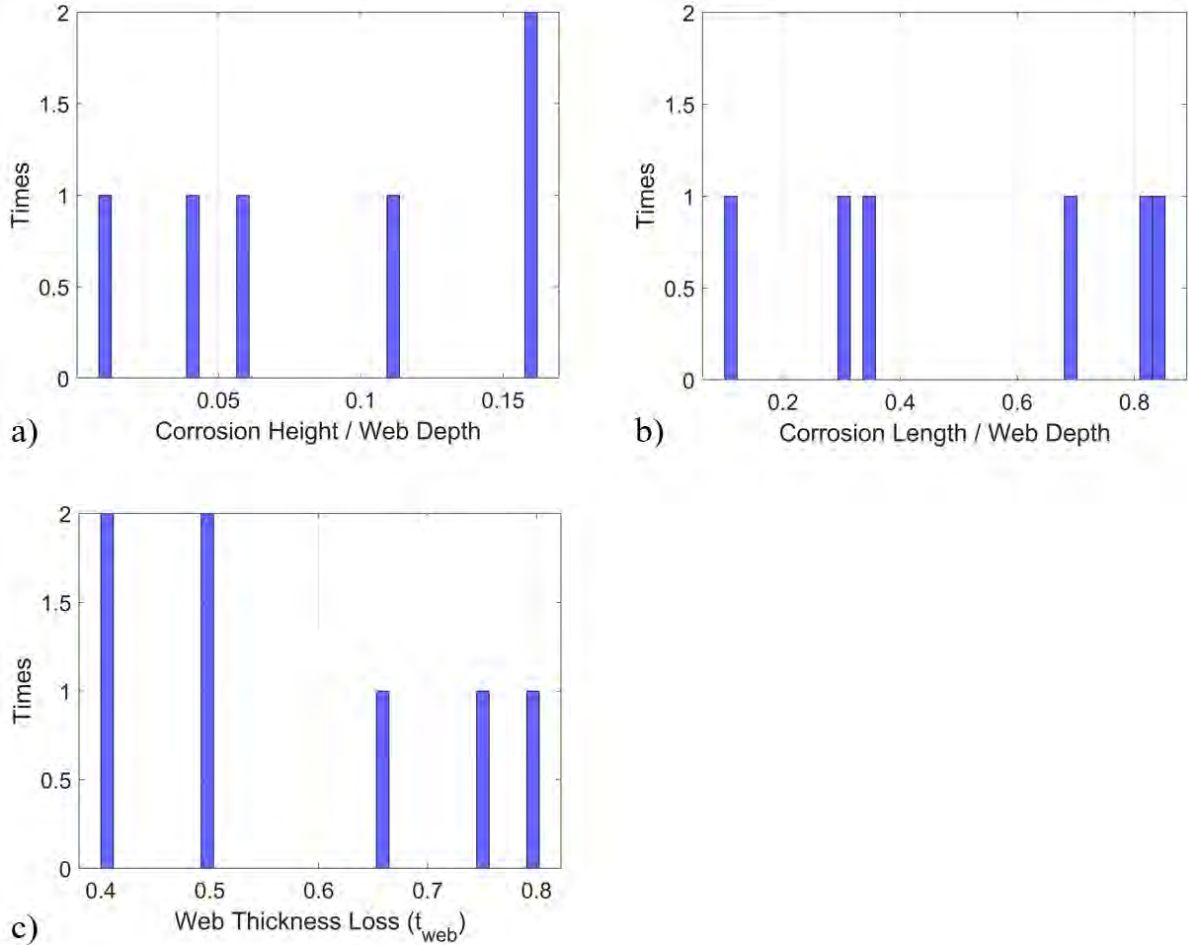


Figure 12.7: Distribution of deterioration characteristics for W3 corrosion scenario for beams with unique stiffener above bearing

Web Holes

Out of the 10 recorded W3 cases, the H1 hole pattern was reported six times, either as the unique hole pattern or in combination with the H2. According to Fig. 12.8, the height of H1 extends up to 9% of depth (d_w), while its length extends along the whole surface between the outer web edge and the stiffener (hole length = c).

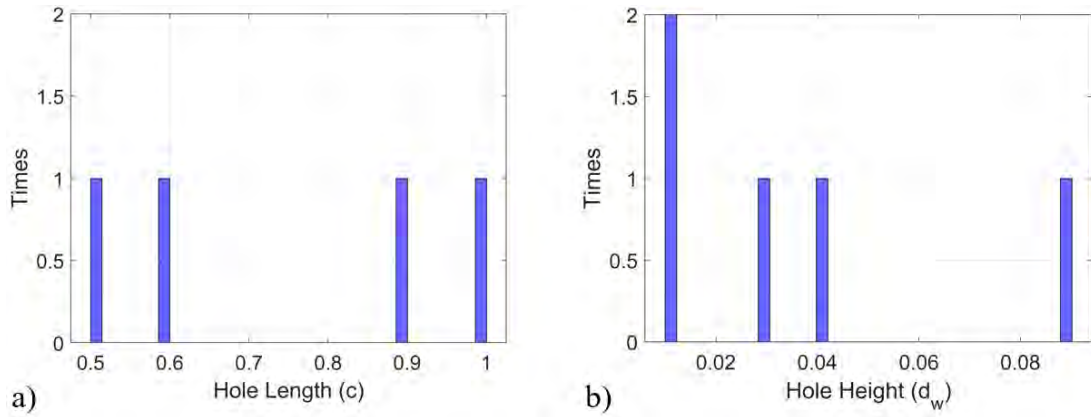
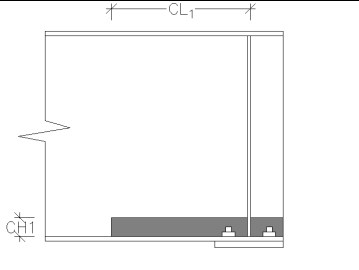

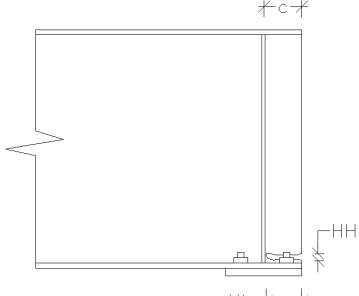
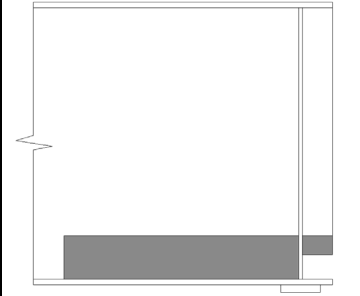


Figure 12.8: a) Length and b) height of H2 holes associated with W3 web corrosion pattern for beams with unique stiffener above bearing

Table 12.3: Dimension of most common deterioration scenarios for W3 web corrosion pattern and associated holes

	
W3	
CH_1 (d_w)	0–16%
CL_1 (d_w)	0–85%
tw_{loss} (t_{web})	40–80%
	
H1	
HL (c)	0–100%
HH (d_w)	0–9%

W4 Corrosion Pattern

Two corrosion heights (CH_1 and CH_2) and two corrosion lengths (CL_1 and CL_2) were introduced to describe the W4 deterioration scenario, where the damaged area extends along both sides of the bearing stiffener with varying deterioration height. The W4 pattern constitutes the most rarely found scenario (4%), and the distribution of its corrosion metrics are presented in Figs. 12.9 and 12.10.

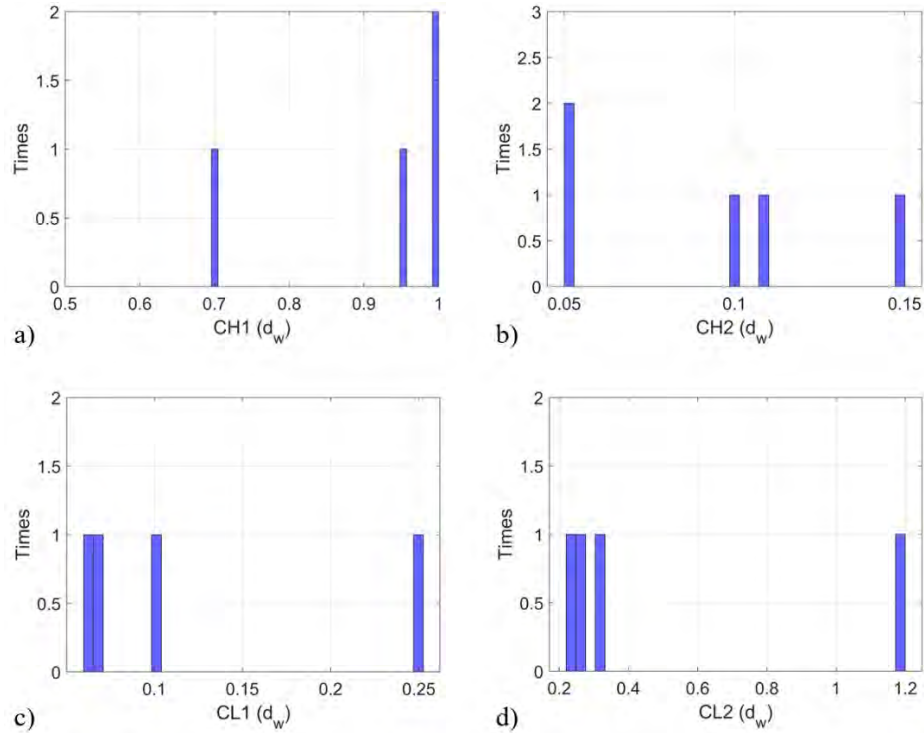


Figure 12.9: Corrosion height and length distribution of W4 corrosion pattern for beams with unique stiffener above bearing

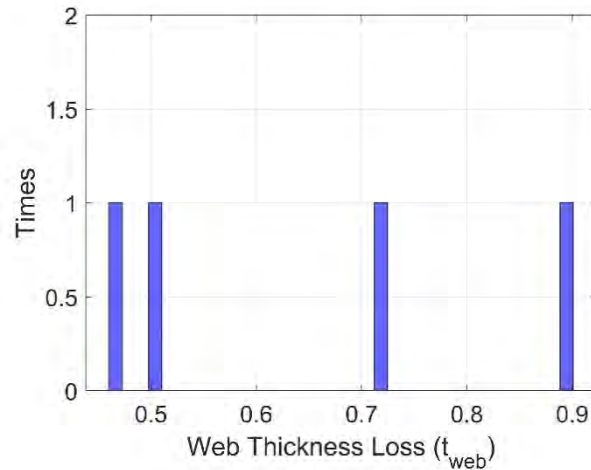


Figure 12.10: Thickness loss distribution of W4 corrosion pattern for beams with one bearing stiffener

Web Holes

Out of the five beam ends with W5 corrosion pattern, three of them were reported with the H1 + H2 holes combination. The metrics of both holes are presented in Figs. 12.11 and 12.12.

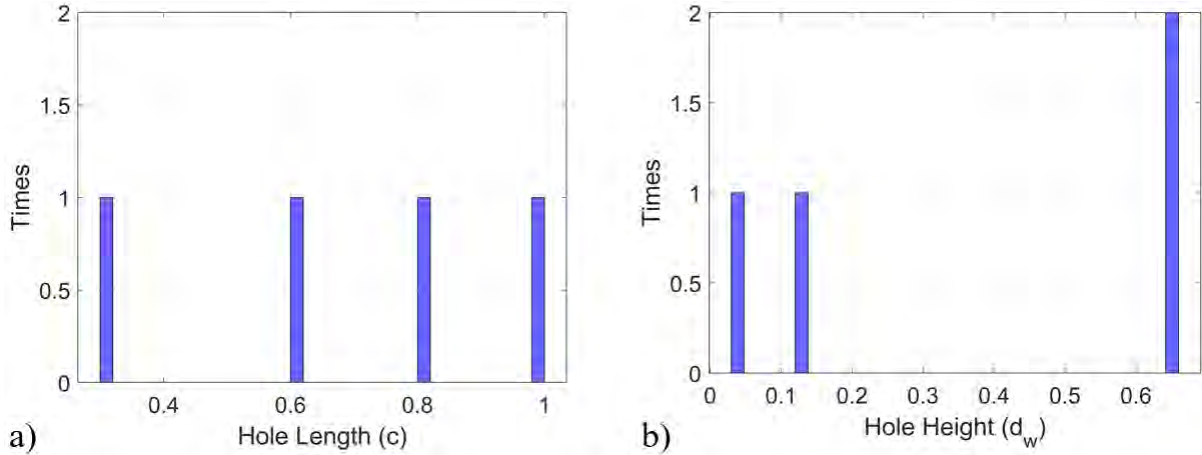


Figure 12.11: a) Hole length and b) height of H1 holes reported with W4 corrosion pattern, for beams with one bearing stiffener

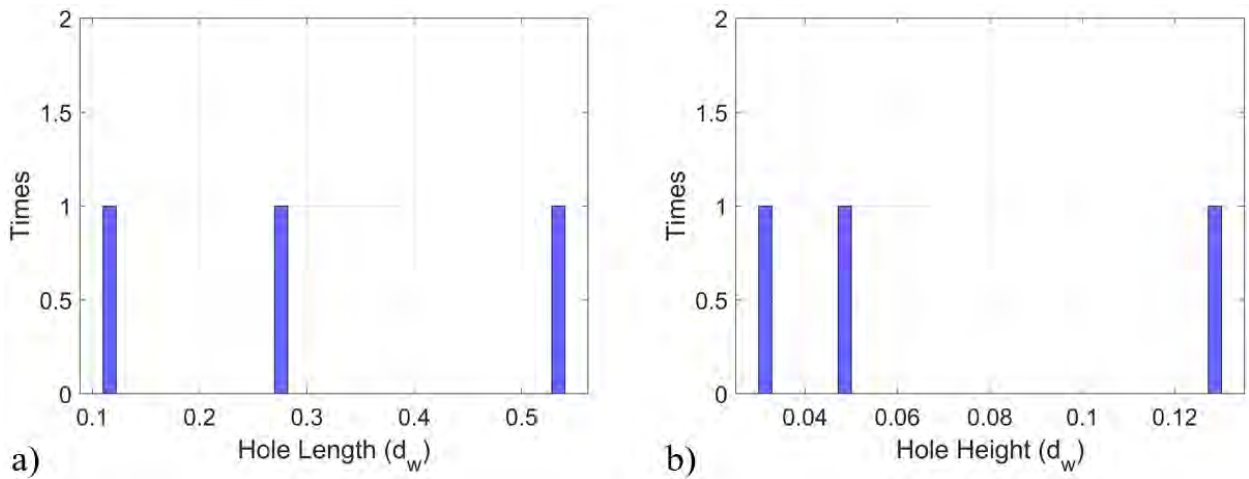
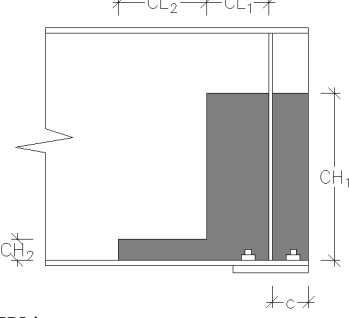

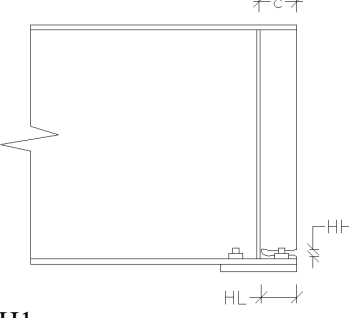
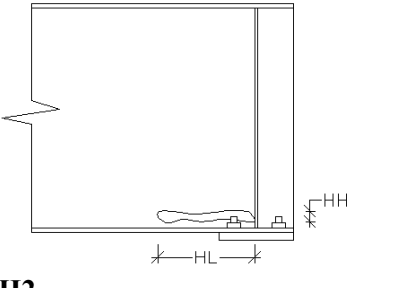
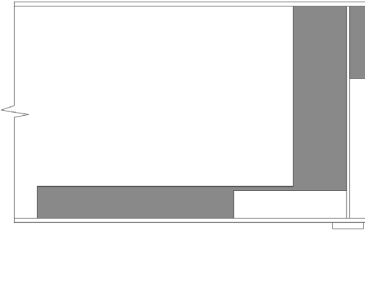


Figure 12.12: a) Hole length and b) height of H2 holes reported with tW4 corrosion pattern, for beams with one bearing stiffener

Table 12.4: Dimension of most common deterioration scenarios for W4 web corrosion pattern and associated holes

 <p>W4</p>		
CH ₁ (d _w)	70–100%	
CH ₂ (d _w)	5–15%	
CL ₁ (d _w)	0–25%	
CL ₂ (d _w)	20–120%	
tW _{loss} (t _{web})	40–90%	
 <p>H1</p>	 <p>H2</p>	
HL (c)		0–100%
HH (d _w)		0–66%
	HL (d _w)	0–54%
	HH (d _w)	0–13%

W5 Corrosion Pattern

W5 is the most commonly reported corrosion scenario (36%) and describes a damage area with varying height before and after the bearing stiffener. The distribution of the recorded metrics related to the W5 pattern are displayed in Fig. 12.13.

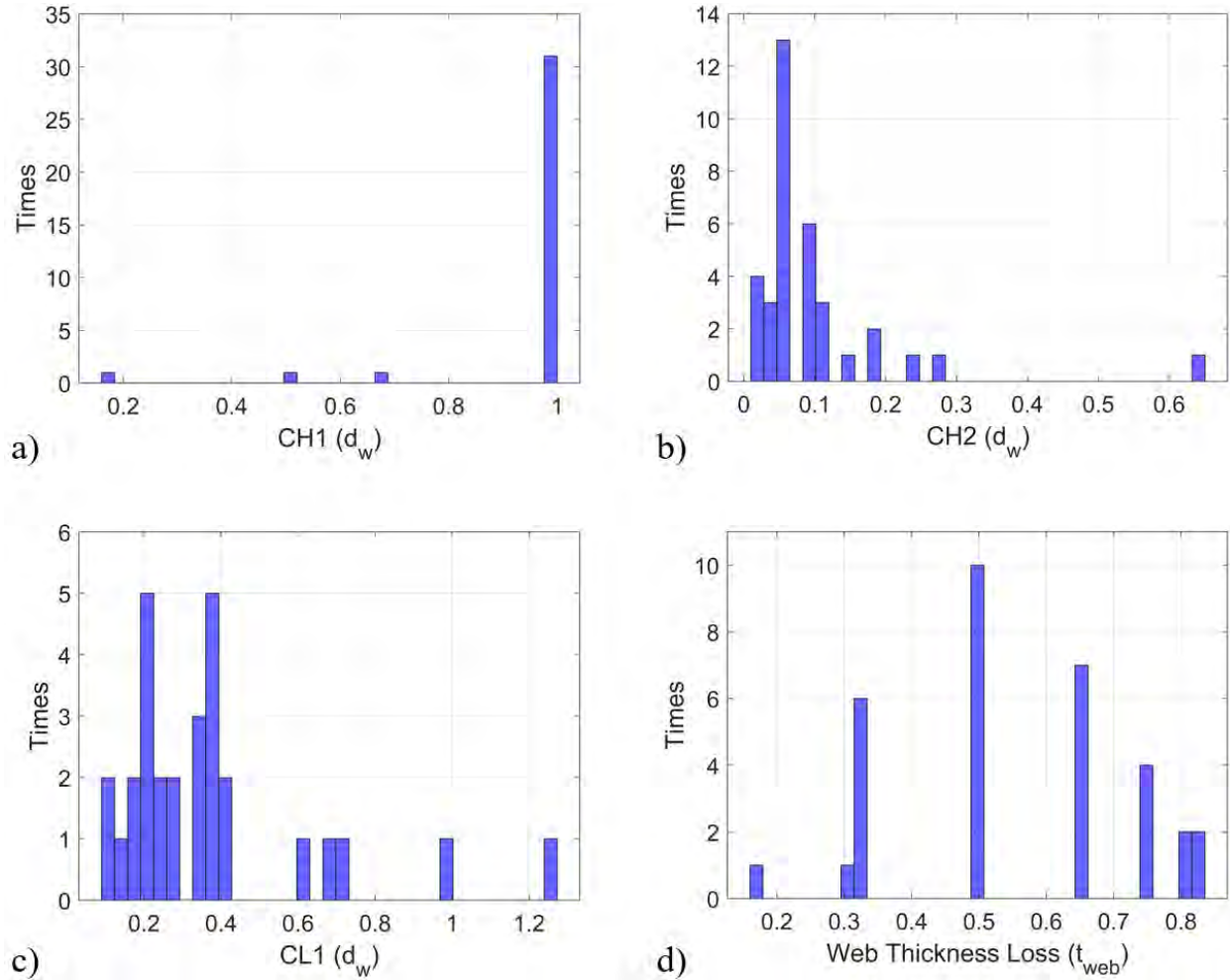


Figure 12.13: Distribution of W5 deterioration characteristics for beams with unique stiffener above bearing

The W5 pattern was found in combination with a plethora of web hole cases and hole combinations. The governing cases are the H1 and the H1+H2 combination (Fig. 12.14 to 12.17). The metrics describing the most common cases for W5 corrosion scenario and the associated holes are presented in Table 12.5.

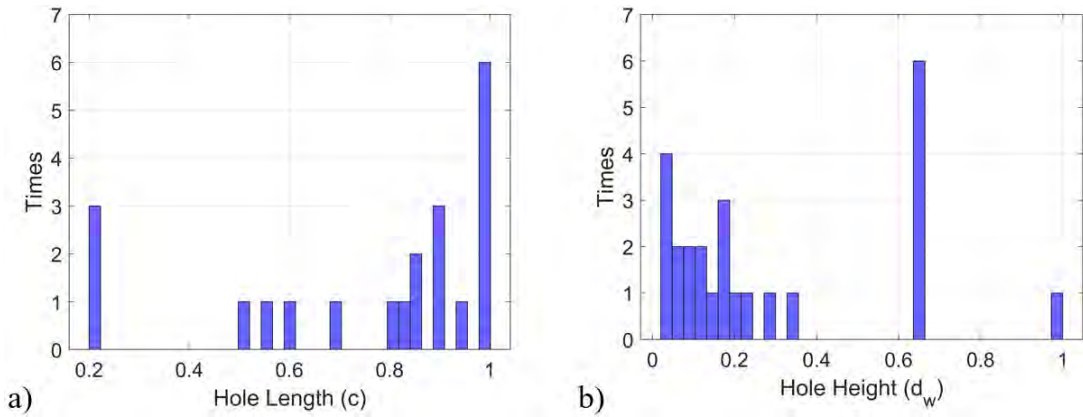


Figure 12.14: Recorded dimensions of H1 holes associated with W5 web corrosion pattern for beams with unique bearing stiffener

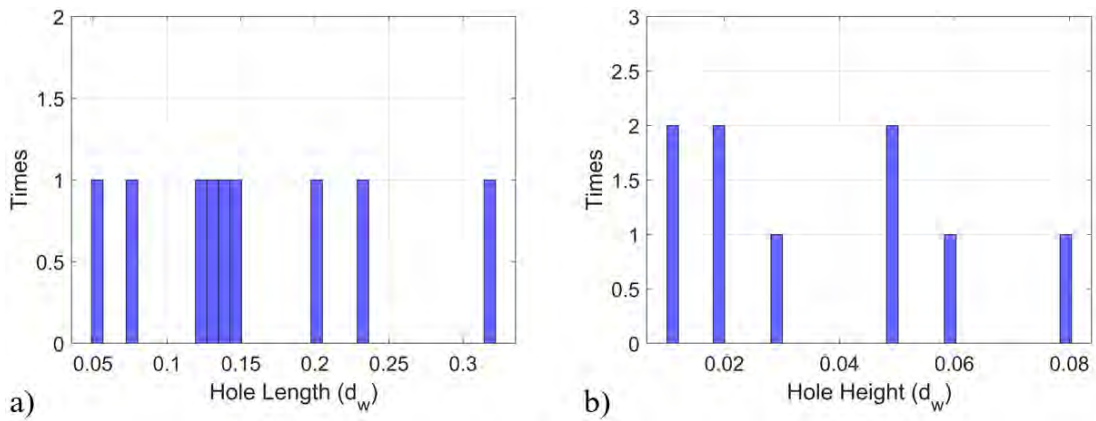


Figure 12.15: Recorded dimensions of H2 holes associated with W5 web corrosion pattern for beams with unique bearing stiffener

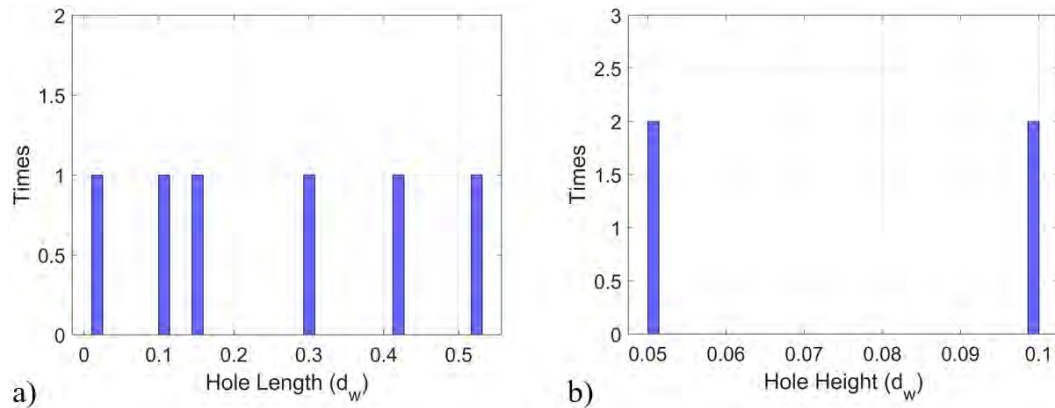


Figure 12.16: Recorded dimensions of H3 holes associated with the W5 web corrosion pattern for beams with a unique bearing stiffener.

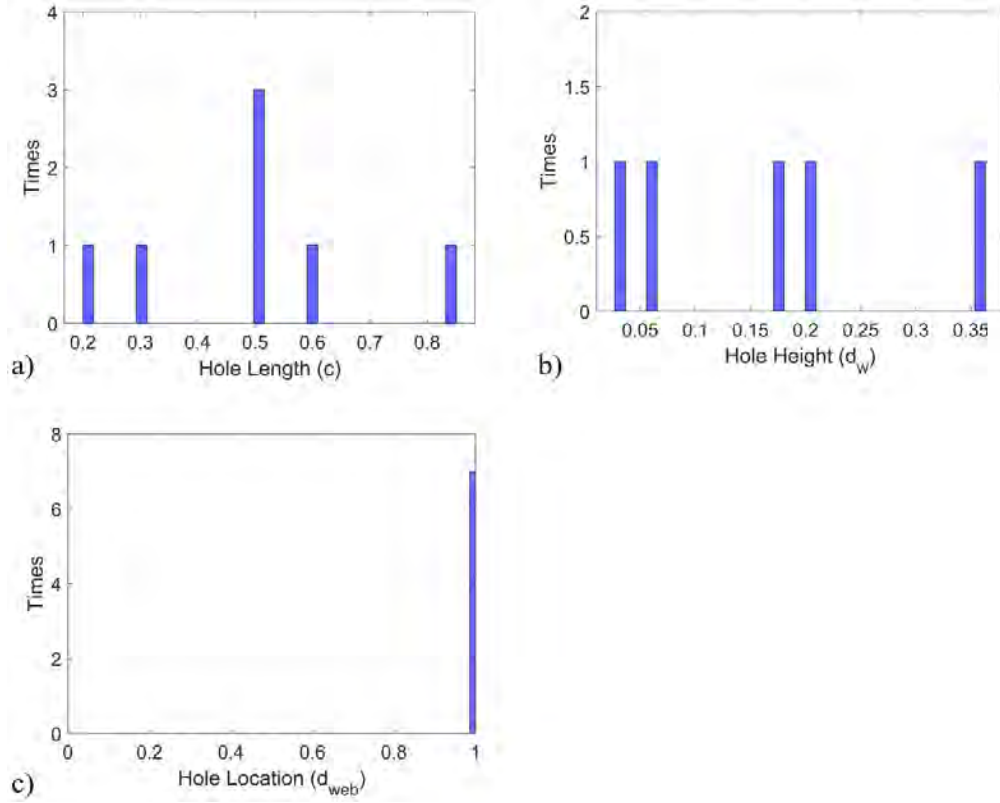
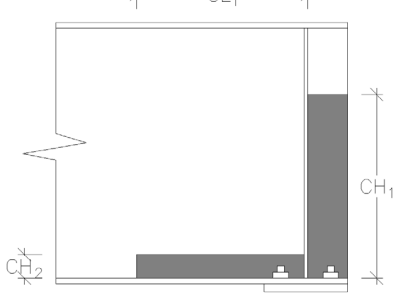
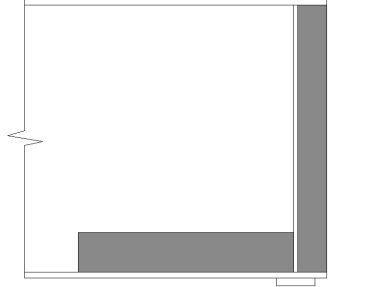
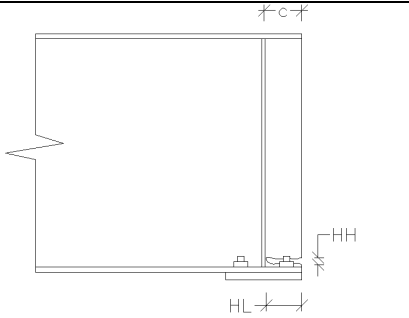
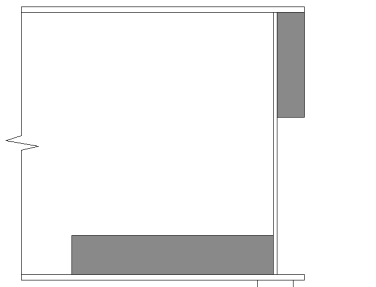
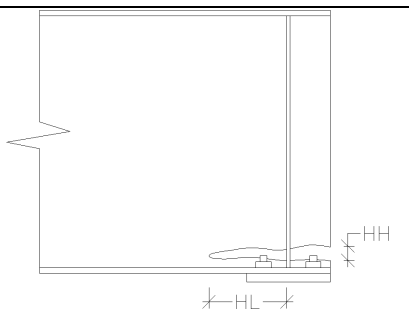
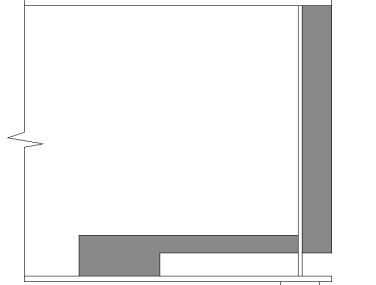


Figure 12.17: Recorded dimensions of H4 holes associated with W5 web corrosion pattern for beams with unique bearing stiffener

Table 12.5: Dimension of the most common deterioration scenarios for W5 web corrosion pattern and the associated holes.

 <p>W5</p>		
CH ₁ (d _w)	100%	
CH ₂ (d _w)	0–15%	
CL ₁ (d _w)	0–70%	
tw _{loss} (t _{web})	20–80%	
 <p>H1</p>		
HL (c)	0–100%	
HH (d _w)	0–60%	
 <p>H3</p>		
HL (d _w)	0–50%	
HH (d _w)	0–10%	

<p>W5</p>		
<p>H1</p>	<p>H2</p>	
HL (c)		0–100%
HH (d _w)		0–60%
	HL (d _w)	0–30%
	HH (d _w)	0–8%
<p>H3</p>	<p>H4</p>	
HL (d _w)		0–15%
HH (d _w)		0–5%
	HL (d _w)	0–60%
	HH (d _w)	0–20%
	b(d _w)	100%

Stiffener Corrosion

Corrosion data for 32 stiffeners was found and examined independently of the web condition. Fig. 12.18 presents the distribution of the corrosion height and the section loss that these stiffeners experienced.

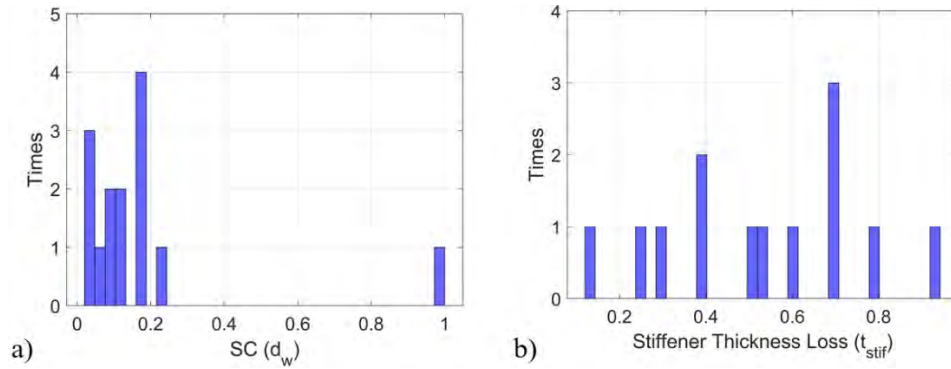


Figure 12.18: a) Corrosion height and b) section loss of stiffeners for beams with one bearing stiffener.

The dimensions of holes found at these 32 stiffeners are presented in Fig. 12.19.

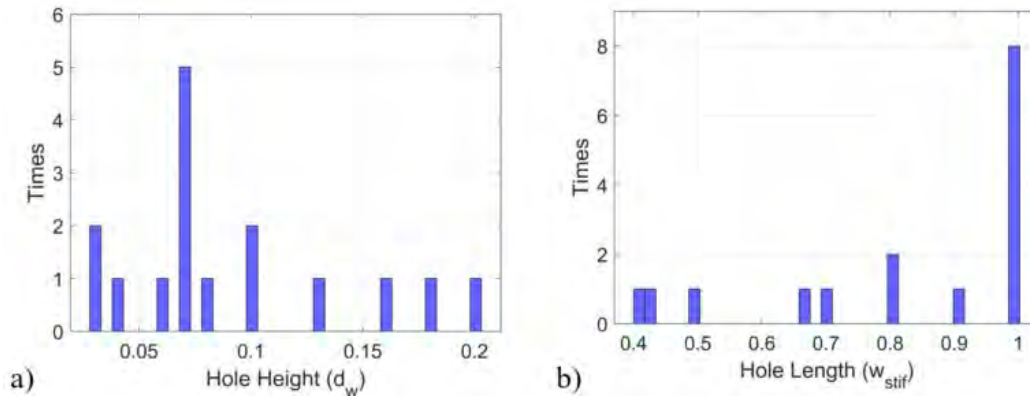
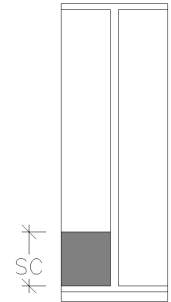
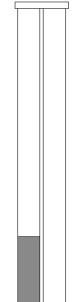
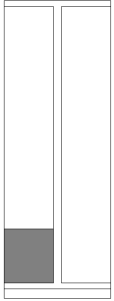

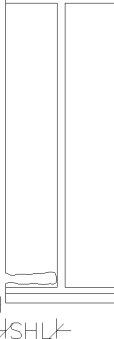



Figure 12.19: Hole height and length of corroded stiffeners for beams with one bearing.

Finally, Table 12.6 summarizes the range of variation of all the parameters involved to describe the stiffener corrosion and holes for beams with a unique bearing stiffener per web face.

Table 12.6: Dimension of the most common deterioration scenarios for stiffener corrosion and holes for beam ends with C1 configuration.

 <p>SC</p>	 <p>w_{stif}</p>
S1	
SC (d_{stif})	0–25%
t_loss (w_{stif})	10–90%

 <p>S1</p>	
 <p>HS</p>	
<p>SHH (d_w)</p>	<p>0–10%</p>
<p>SHL (w_{stif})</p>	<p>0–100%</p>

12.2 Appendix B: Detailed Data and Processing Graphs for Beam Ends with Two Bearing Stiffeners

W1 Corrosion Pattern

Corrosion height (CH_1) is the unique geometric characteristic of the W1 pattern, which describes web section loss at the domain between the bearing stiffeners. Fig. 12.20 presents the CH_1 and thickness loss distribution of the recorded cases.

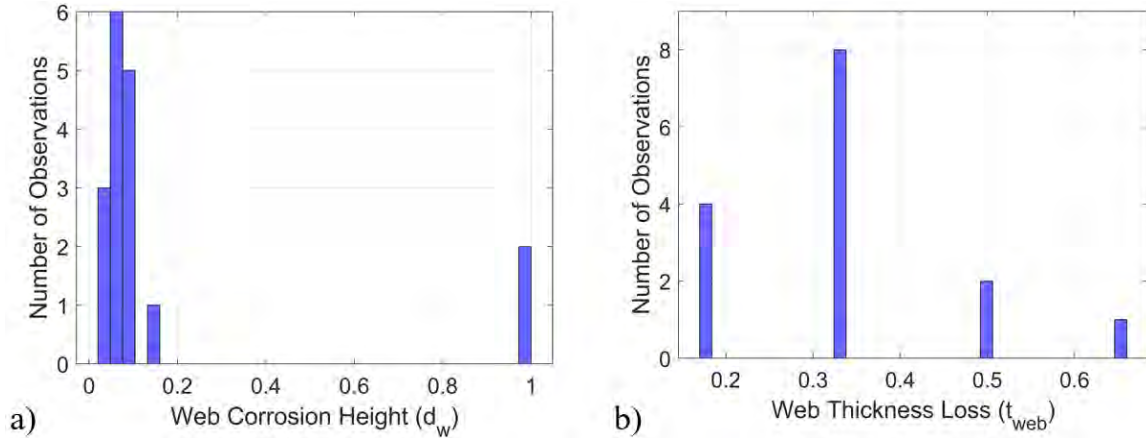
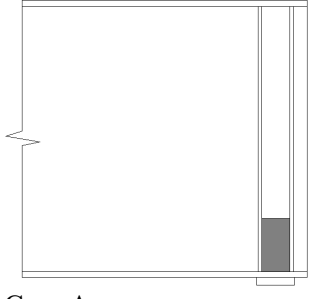
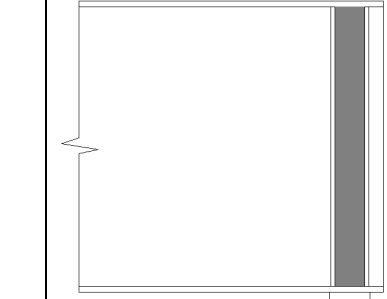


Figure 12.20: a) Corrosion height and b) section loss distribution of W1 corrosion pattern for beams with two bearing stiffeners per web face

Almost 90% (14 out of 16) of the reported cases have corrosion height less than 20% of web depth. However, the rest (10%) is taken into account by considering Case B in Table 12.7, with full height corrosion along the domain between the bearing stiffeners.

Table 12.7: Dimension of most common deterioration scenarios for W1 web corrosion

		
W1	Case A	Case B
CH_1 (d_w)	0–20%	100%
$t_{W_{loss}}$	20–70%	

W2 Corrosion Pattern

Corrosion height (CH_1) and length (CL_1) are the two geometric characteristics of the W2 pattern. The recorded deterioration characteristics of the W2 pattern are presented in Fig. 12.21. In cases where the corrosion length equals zero, which according to Fig. 12.21b is the dominant scenario, the damage area is limited to the domain between the outer web edge and the adjacent stiffener.

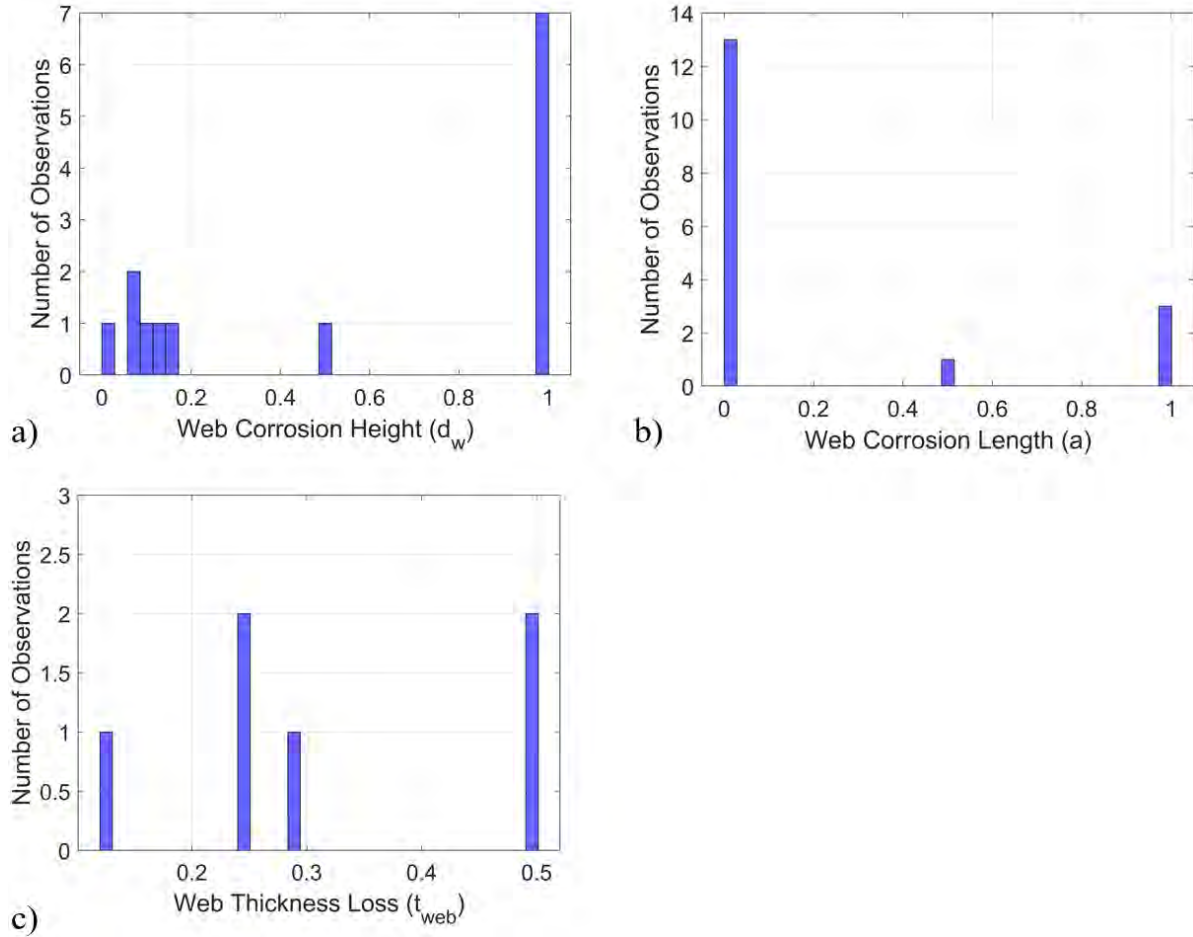


Figure 12.21: a) Corrosion height; b) length; and c) section loss of W2 corrosion pattern for beams with two bearing stiffeners

Nevertheless, a trend for $CL=1$ cannot be neglected. Based on Fig. 12.22, which displays the corrosion height of the cases that expand beyond the outer stiffener ($CL \neq 0$, in Fig. 12.21b), full height corrosion is considered for cases with $CL=0$, and up to 10% of depth for $CL=1$.

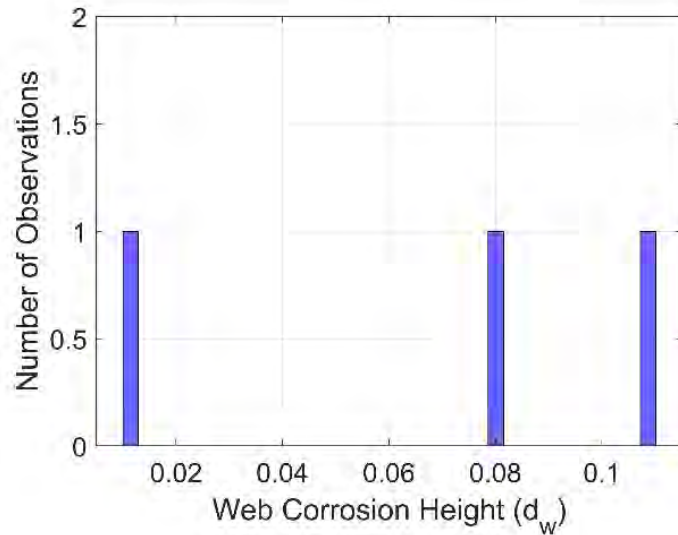


Figure 12.22: Corrosion height of W1 pattern when $CL \neq 0$, for beams with two bearing stiffeners

Table 12.8 summarizes the range of variation of all the parameters involved to describe the web corrosion for beams with W2 pattern.

Table 12.8: Dimension of most common deterioration scenarios for W2 web corrosion pattern

W2	Case A	Case B
CH_1 (d_w)	0–50%	100%
CL_1 (a)	0–100%	0%
tw_{loss}	0–50%	

W3 Corrosion Pattern

Corrosion height (CH_1) and length (CL_1) are the two geometric characteristics employed to describe the W3 pattern. Fig. 12.23 presents the distribution of the recorded deterioration parameters.

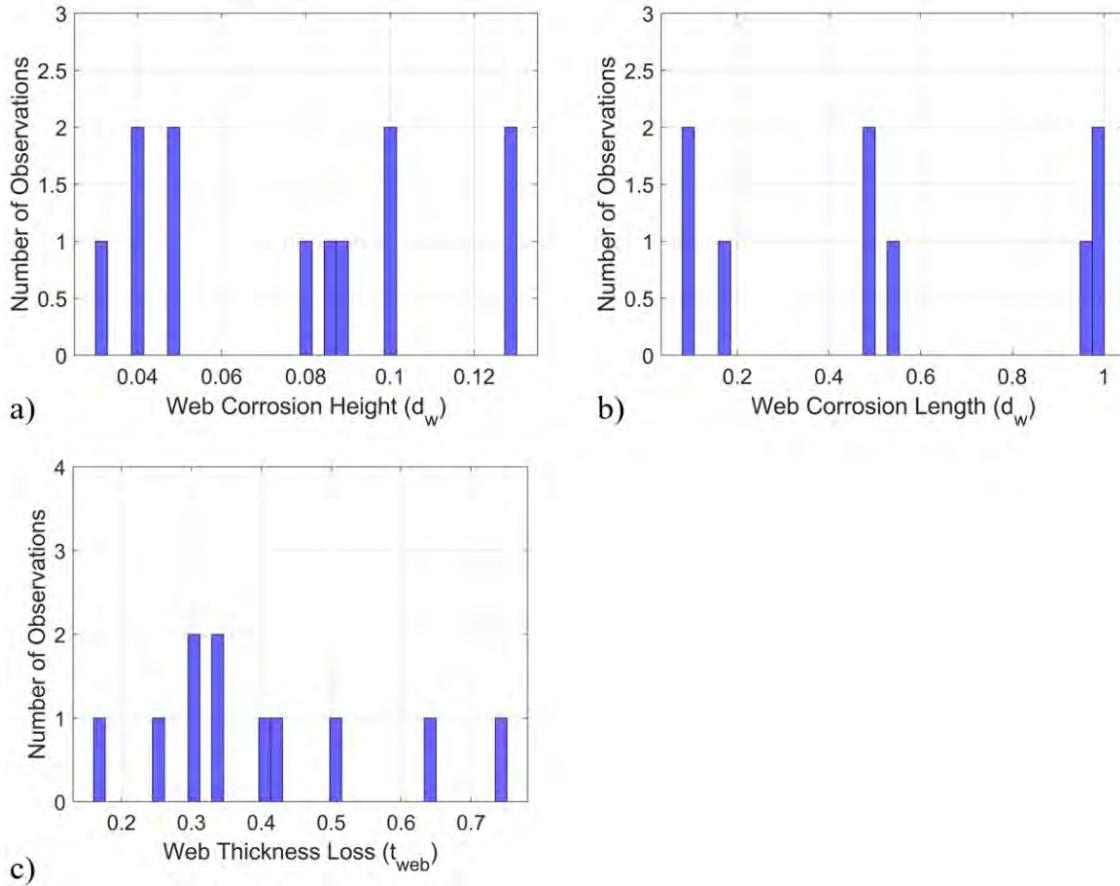
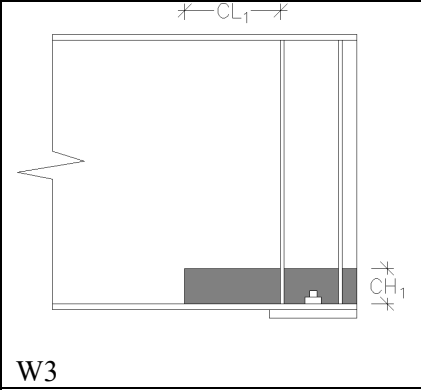
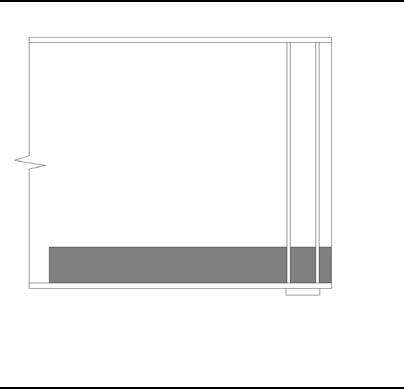


Figure 12.23: a) Corrosion height; b) length; and c) section loss of W3 corrosion pattern for beams with two bearing stiffeners

Based on the data presented in Fig. 12.23, Table 12.9 summarizes the most common deterioration metrics for W3 web corrosion pattern.

Table 12.9: Dimension of most common deterioration scenarios for W3 web corrosion pattern

	
W3	
CH_1 (d_w)	0–15 %
CL_1 (d_w)	10–100%
tw_{loss}	20–80%

W4 Corrosion Pattern

Two corrosion heights (CH_1 and CH_2) and one corrosion length (CL_1) have been introduced to describe the W4 deterioration scenario. The distribution of this parameters is presented in Fig. 12.24.

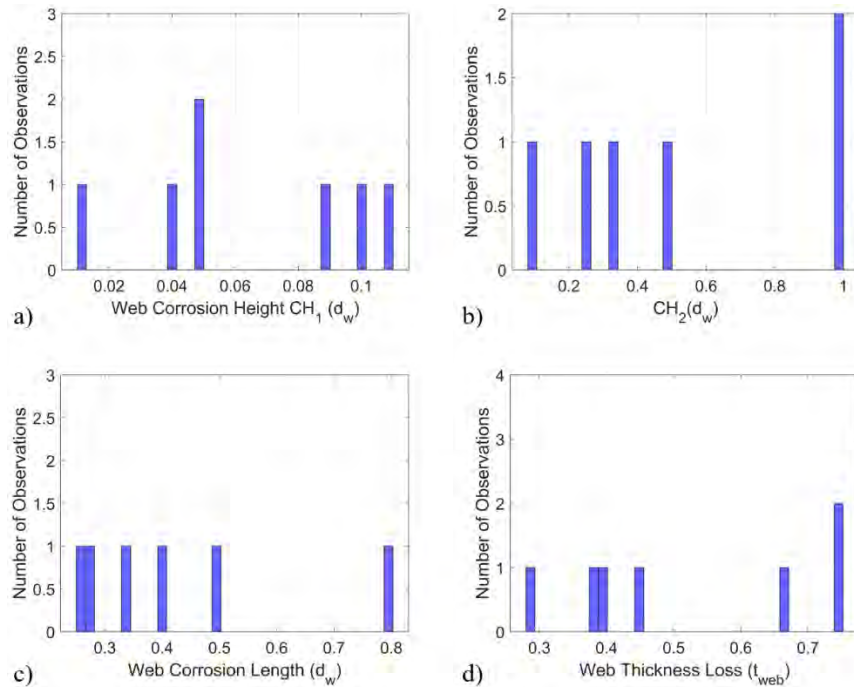
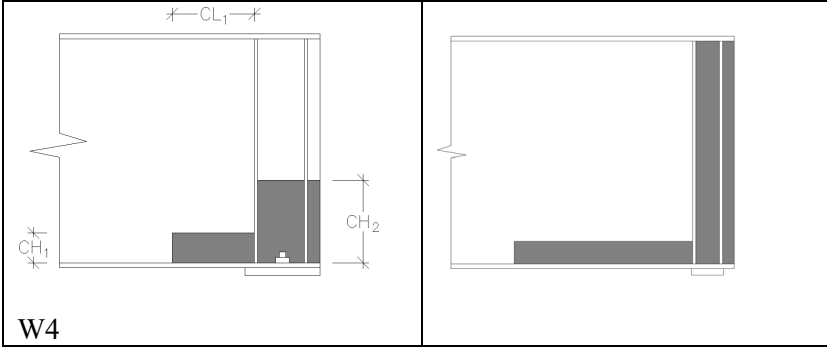


Figure 12.24: Distribution of deterioration characteristics for W4 corrosion scenario for beams with two bearing stiffeners

According to Fig. 12.24a, CH_1 is limited to the lower part of the web, CH_2 covers a wide range between 5% of depth and full height corrosion, while the deterioration length does not

expand more than 80% of depth beyond the inner bearing stiffener. Table 12.10 summarizes the most common deterioration metrics for W4 web corrosion pattern.

Table 12.10: Dimension of most common deterioration scenarios for W4 web corrosion pattern



The diagram shows a cross-section of a beam with two bearing stiffeners. The distance between the stiffeners is labeled CL_1 . The corrosion depth from the outer edge is labeled CH_1 , and the depth from the inner edge is labeled CH_2 . The diagram shows two scenarios: one with partial corrosion and one with full corrosion between the stiffeners.

W4	
CH_1 (d_w)	0–10%
CH_2 (d_w)	10–100%
CL_1 (d_w)	20–80%
tw_{loss}	20–80%

W5 Corrosion Pattern

Two corrosion heights (CH_1 and CH_2) are employed to describe a damage pattern that initiates from the outer web edge and along the whole area between the two bearing stiffeners. The distribution of the recorded deterioration characteristics is presented in Fig. 12.25.

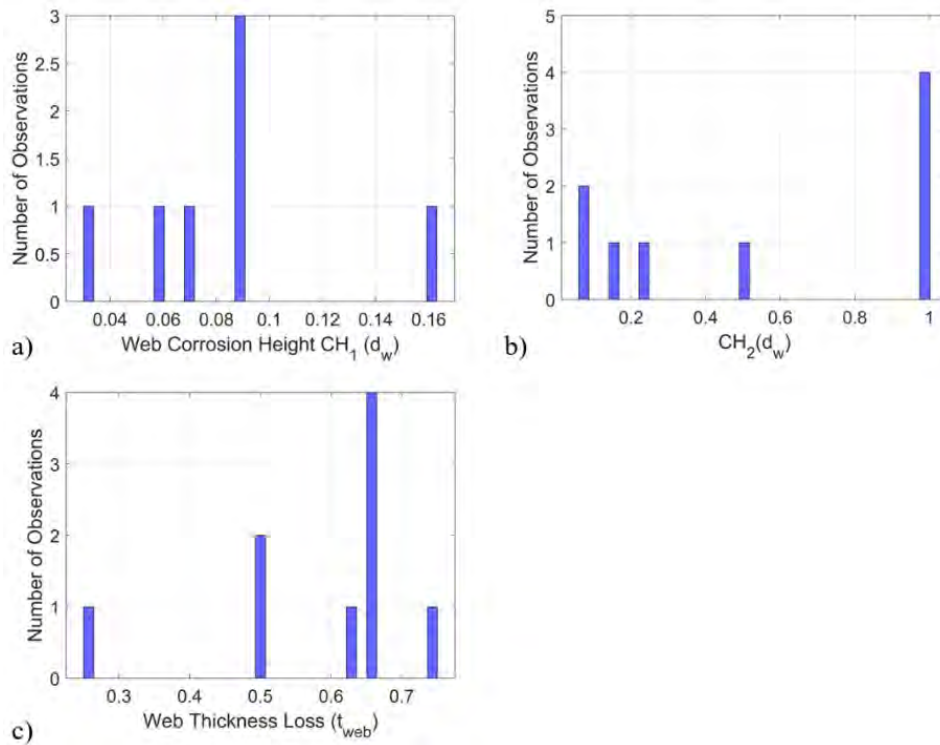


Figure 12.25: Distribution of deterioration characteristics for W5 corrosion scenario for beams with two bearing stiffeners

Table 12.11 summarizes the most common deterioration metrics for the W5 web corrosion pattern.

Table 12.11: Dimensions of most common deterioration scenarios for W5 web corrosion pattern

W5	
CH ₁ (d _w)	0–16%
CH ₂ (d _w)	10–100%
t _{wloss}	20–80%

Web Holes

As already been mentioned in Section 4, web holes were examined independently of the web corrosion patterns.

H1 Hole pattern

Figs. 12.26–12.30 present the distribution of all the parameters involved in describing the general web hole patterns.

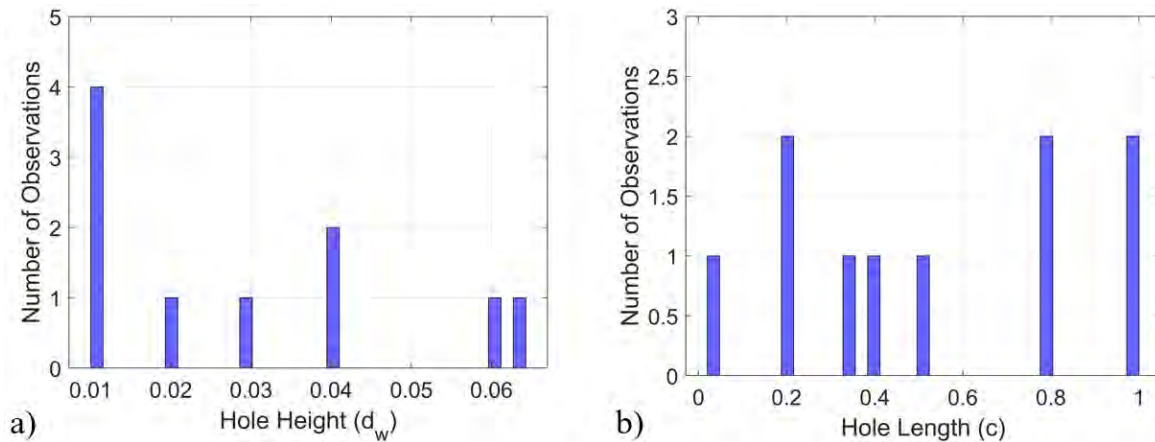


Figure 12.26: a) Hole height and b) length distribution of H1 pattern for beams with two bearing stiffeners

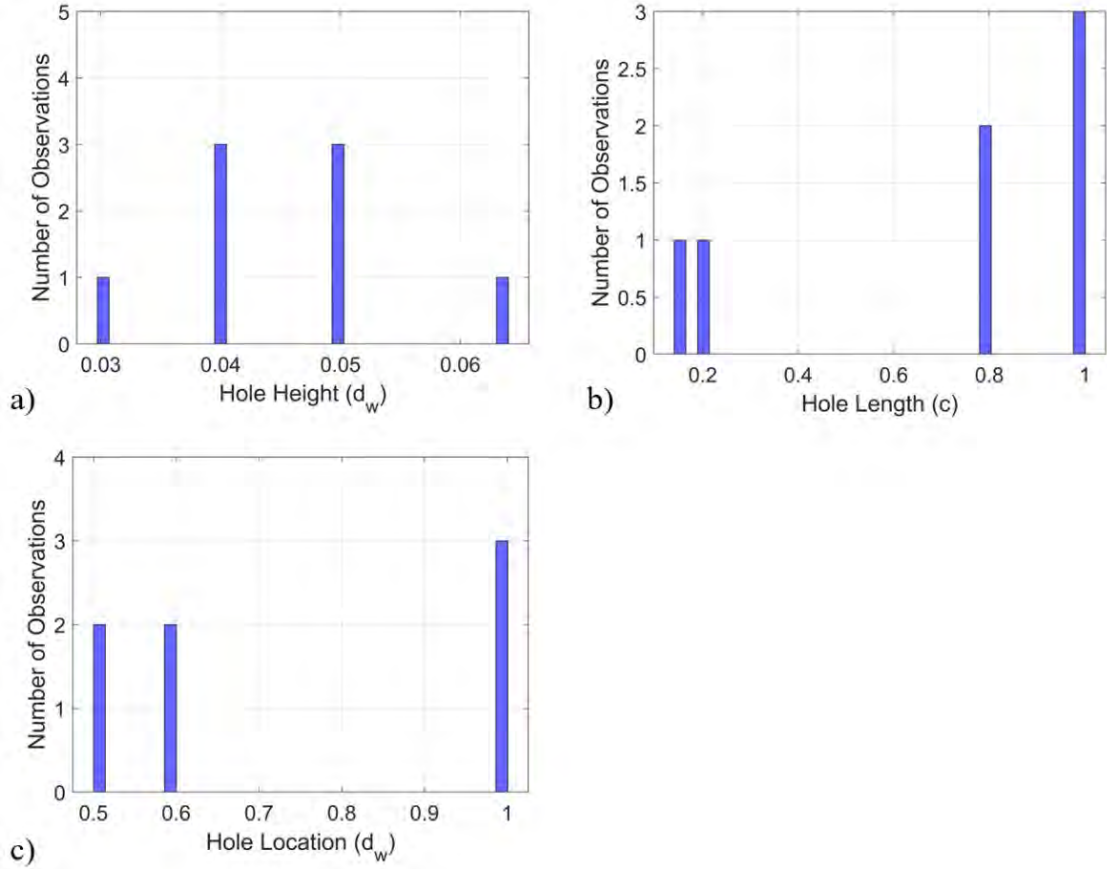


Figure 12.27: a) Hole height; b) length; and c) distance from bottom flange for H4 pattern

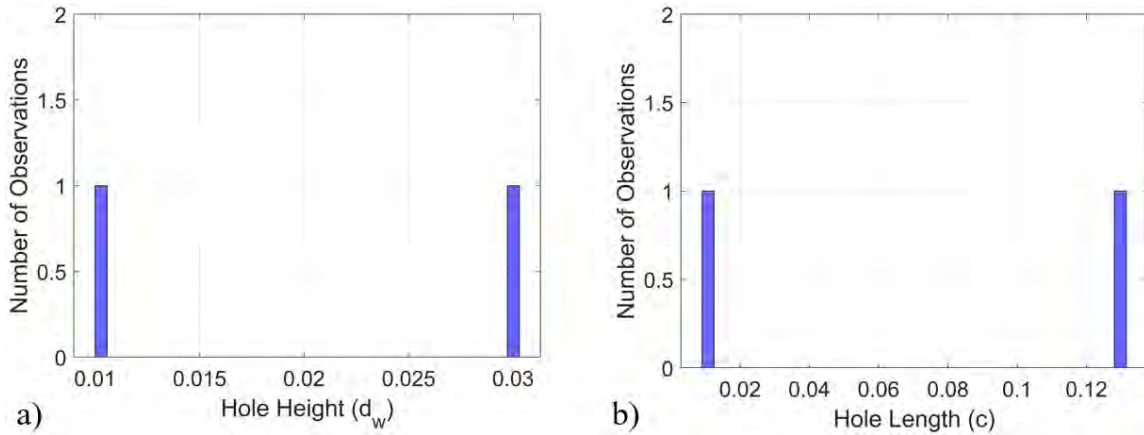


Figure 12.28: a) Hole height and b) length distribution of H3 pattern for beams with two bearing stiffeners

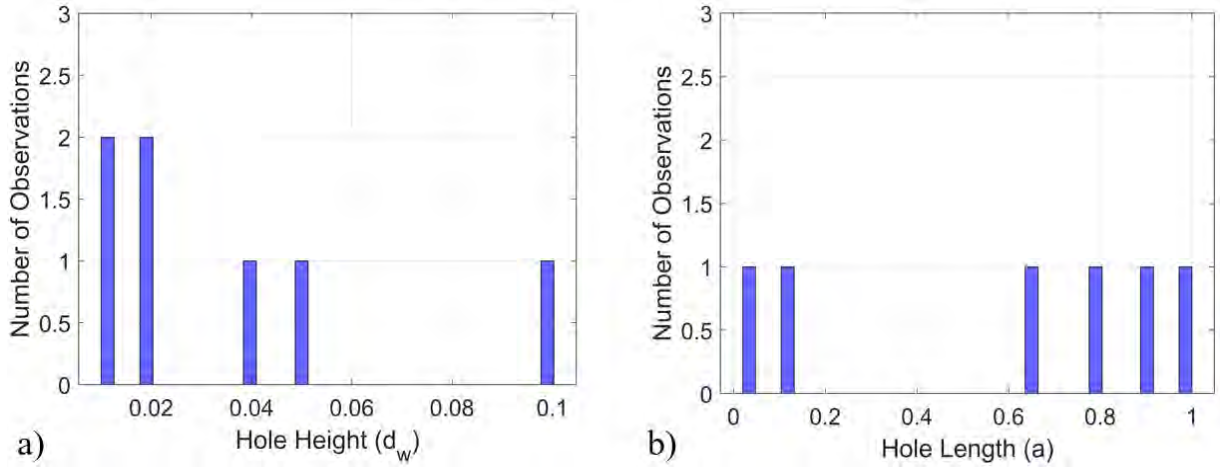


Figure 12.29: a) Hole height and b) length distribution of H4 pattern for beams with two bearing stiffeners

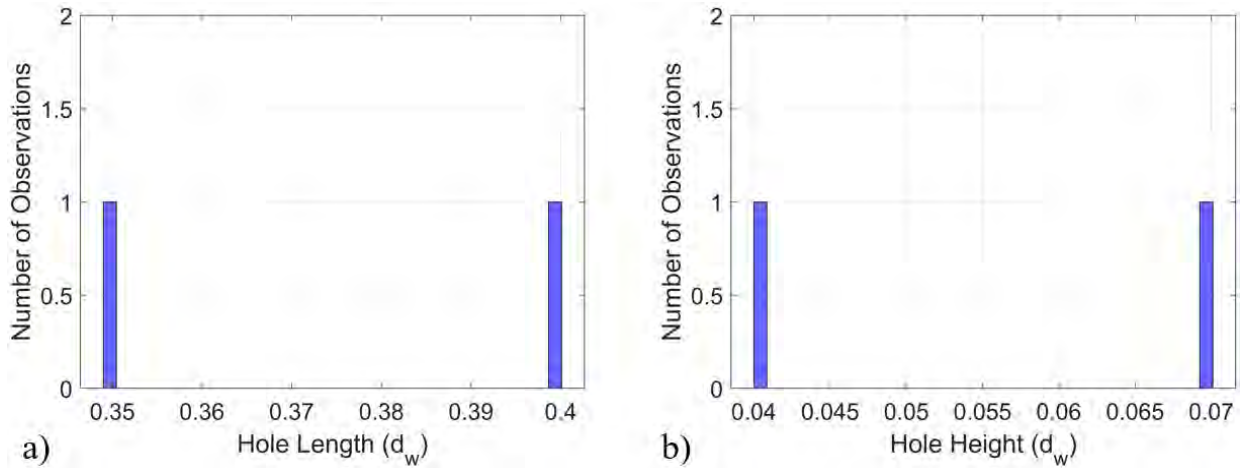
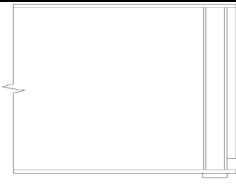
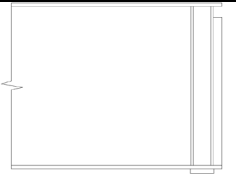
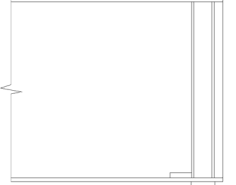
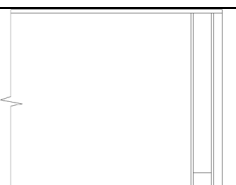
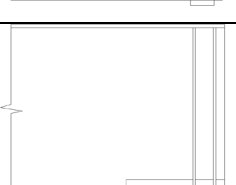


Figure 12.30: a) Hole length and b) height distribution of H4 pattern for beams with two bearing stiffeners

Table 12.12 summarizes the most common deterioration metrics for web hole patterns.

Table 12.12: Dimensions of most common web hole scenarios

Hole ID	Hole Height	Hole Length	Location (d_w)	Extreme Case
H1	0–7%	0–100% (c)		
H2	0–7%	0–100% (c)	50–100%	
H3	0–3%	0–13% (d_w)		
H4	0–10%	0–100% (a)		
H5	0–7%	0–40% (d_w)		

Stiffener Corrosion

Figs. 12.31–12.38 present the corrosion height distribution for the inner (S1) and the outer (S2) bearing stiffeners, sorted according to the corrosion scenario that describes the web condition of the corresponding beam end.

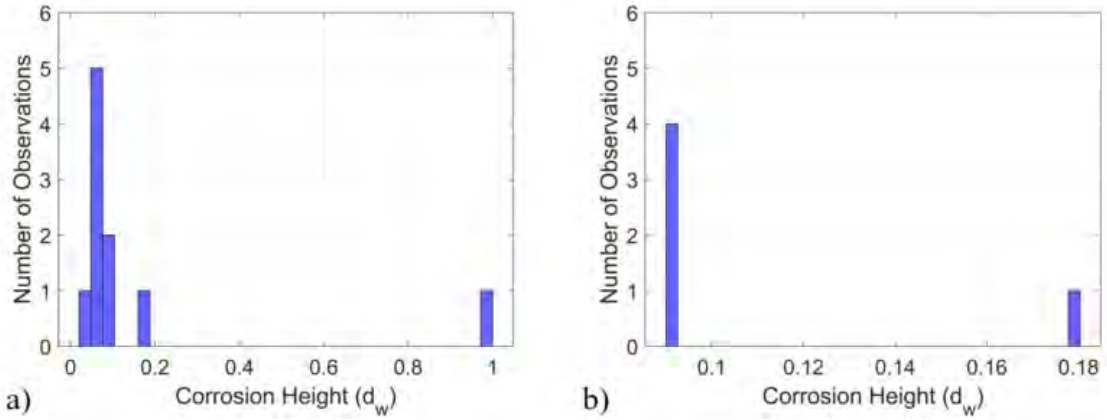


Figure 12.31: Corrosion height of a) S1 and b) S2 for beams with W1 web corrosion pattern

No information was available regarding the corrosion height of S1 for W3 web corrosion pattern.

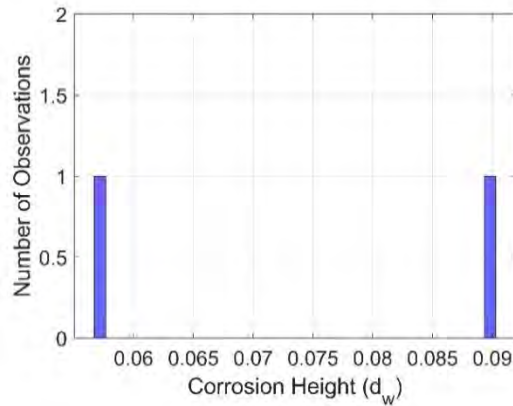


Figure 12.32: Corrosion height of S2 for beams with W3 web corrosion pattern

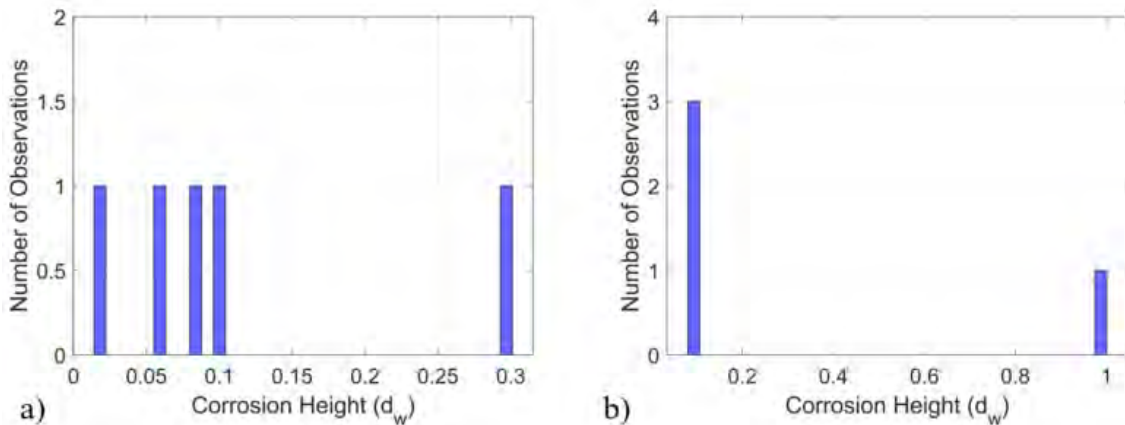


Figure 12.33: Corrosion height of a) S1 and b) S2 for beams with W3 web corrosion pattern

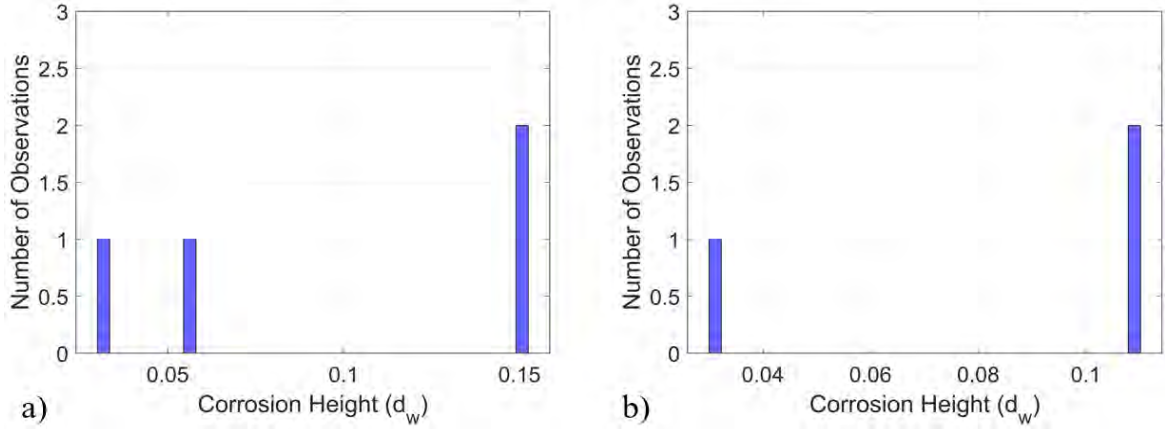


Figure 12.34: Corrosion height of a) S1 and b) S2 for beams with W4 web corrosion pattern

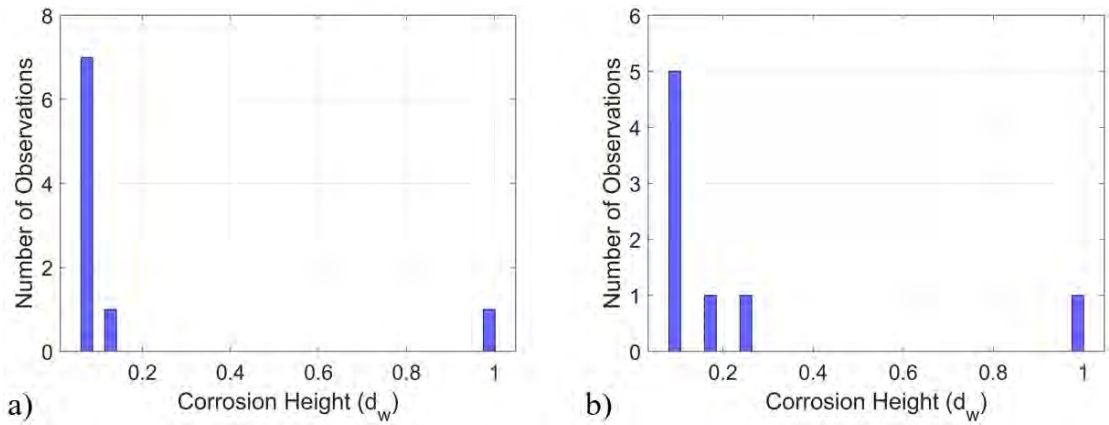


Figure 12.35: Corrosion height of a) S1 and b) S2 for beams with W5 web corrosion pattern

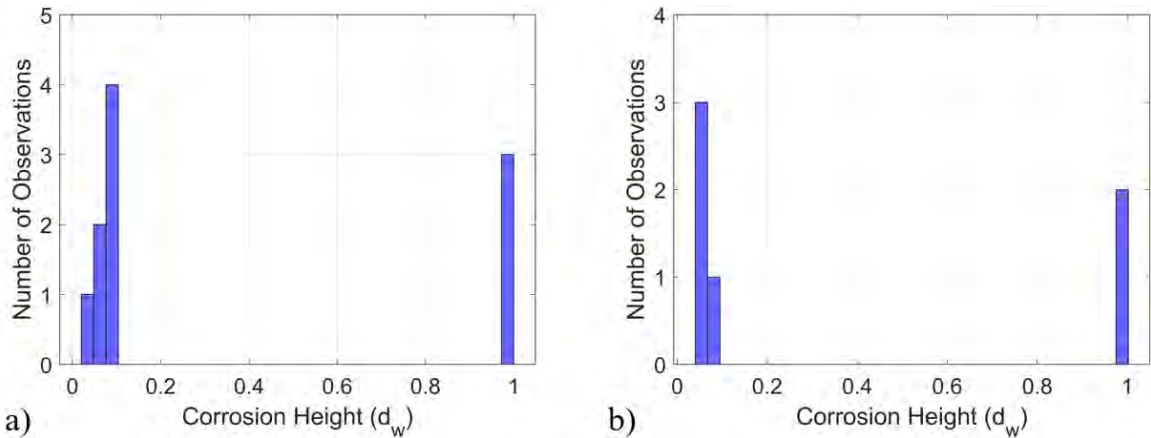


Figure 12.36: Corrosion height of a) S1 and b) S2 for beams without available web corrosion data

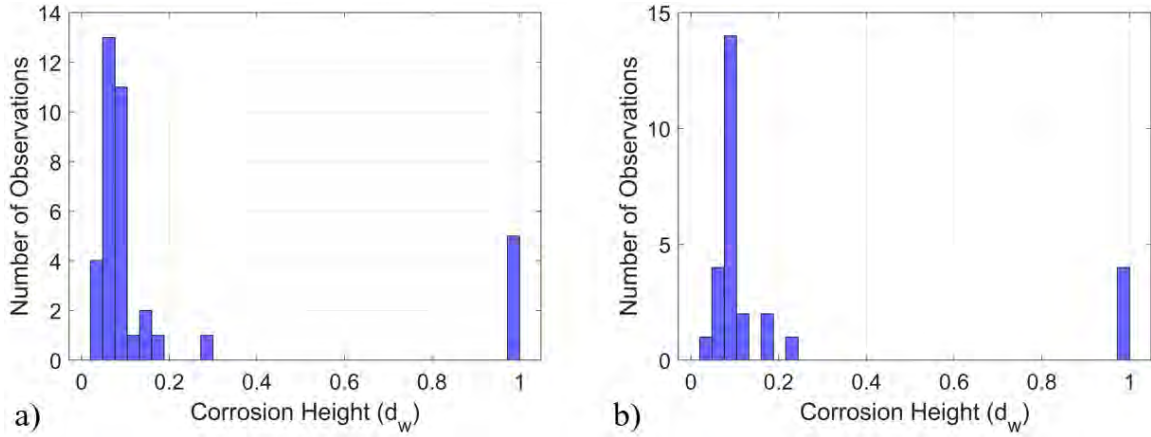


Figure 12.37: Corrosion height of a) S1 and b) S2 for all beams

It is worth noting that based on the initial assumptions, the meaning of corrosion height equal to unit is twofold. It may denote full height corrosion or deterioration at the top of the stiffener. The second case implies there may be areas along the stiffener's depth that have not experienced section loss. However, from Figs. 12.31 to 12.35, it is clear that stiffeners mainly exhibit corrosion at their lower part, and the damage height does not exceed the 20% of depth. Also, non-significant correlation between the corrosion height and web corrosion pattern is observed.

Fig. 12.38 presents the section loss of S1 and S2 for the whole sample. For both cases, the section loss covers the whole range between 10% and 90% of the intact web thickness.

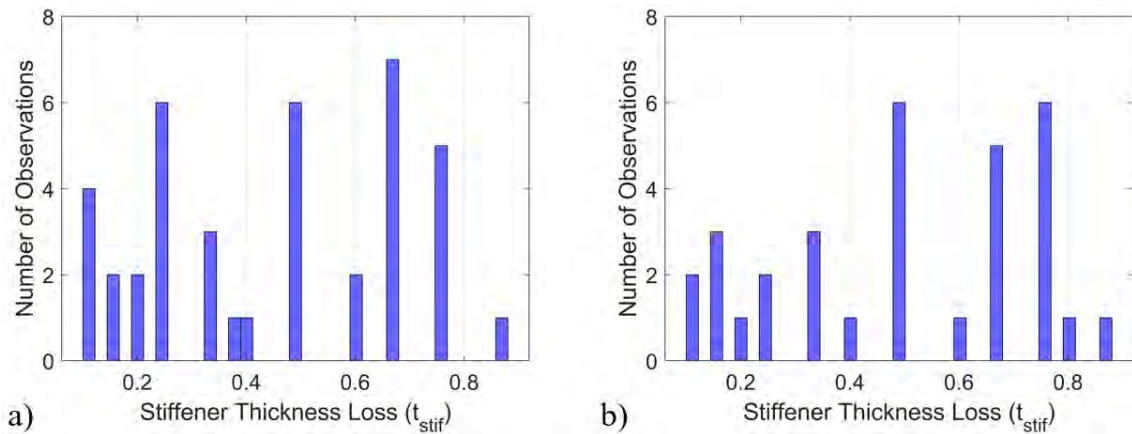


Figure 12.38: Thickness loss distribution of a) S1 and b) S2 for whole sample

Stiffener Holes

Figs. 12.39 and 12.40 present the distribution of hole dimensions located at the bottom of S1 and S2 for the total sample. For both cases (S1 and S2), the hole height does not exceed 13% of web depth, while the hole can extend along the whole width of the stiffener.

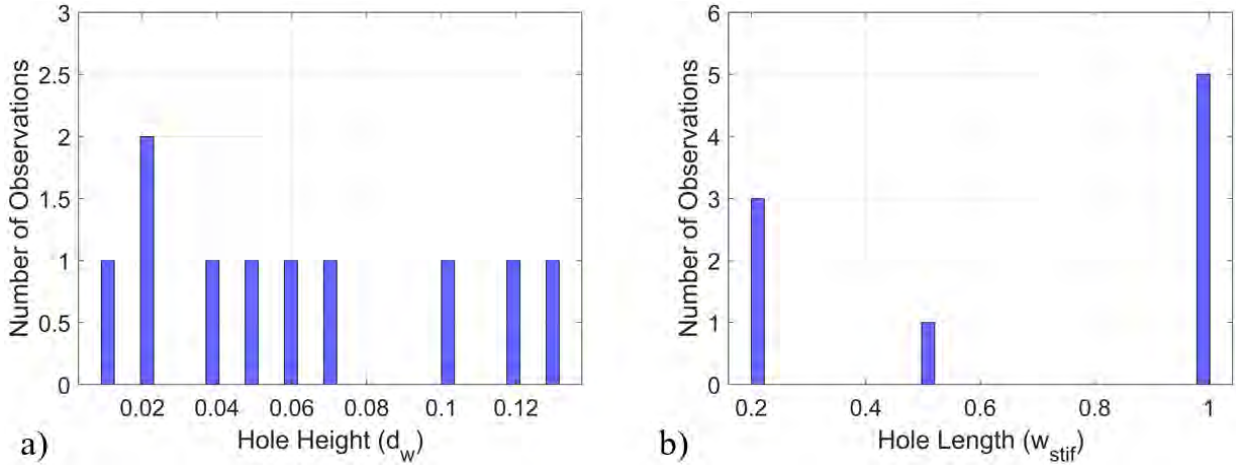


Figure 12.39: Dimensions of holes located at S1 bottom

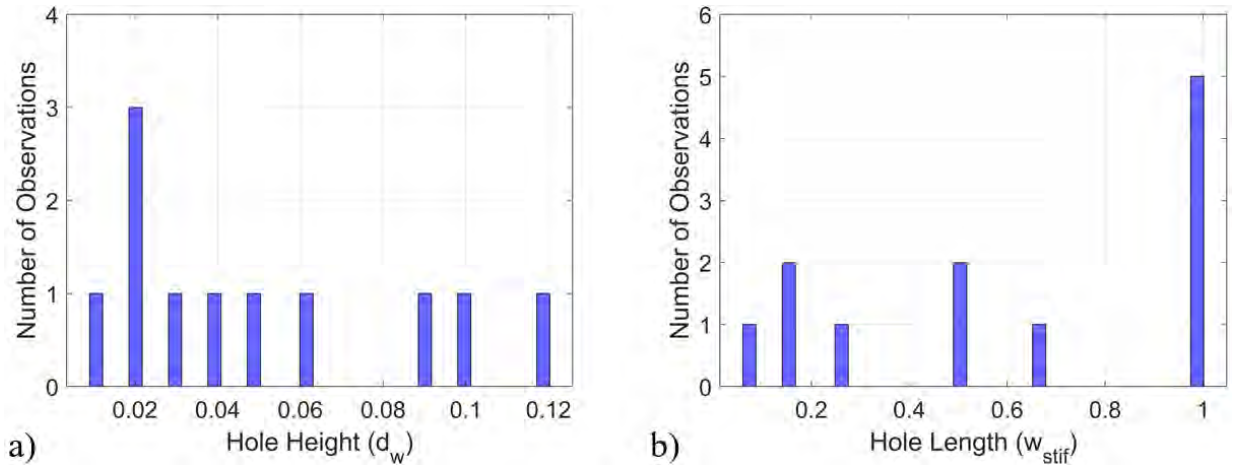


Figure 12.40: Dimensions of holes located at S2 bottom

Finally, Fig. 12.41 and Table 12.13 illustrate the corrosion characteristics of holes located at the top part of stiffeners.

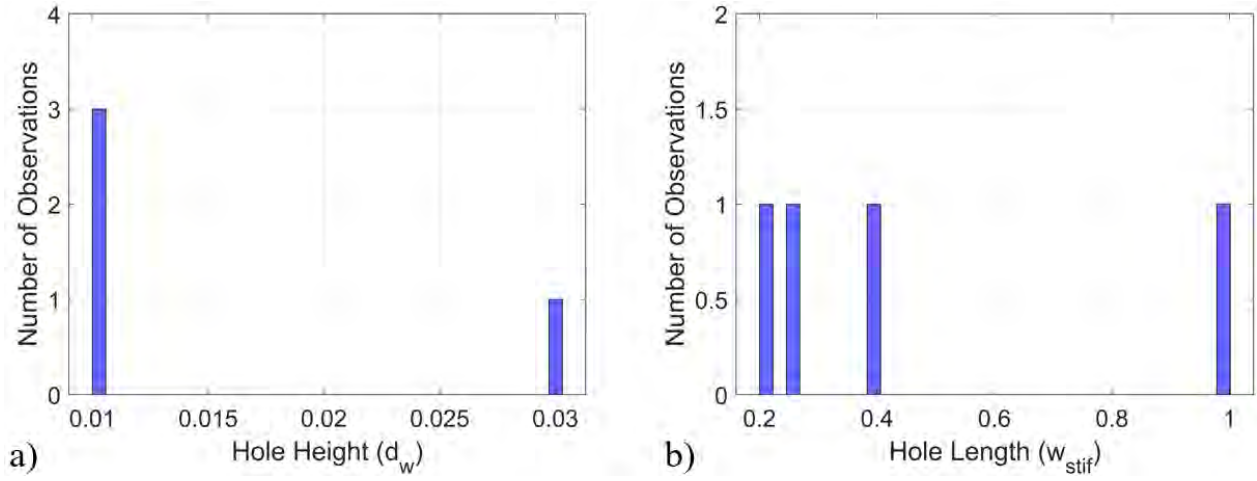
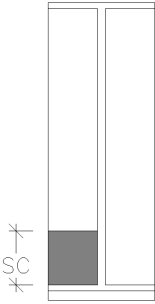

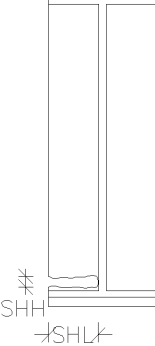
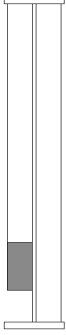
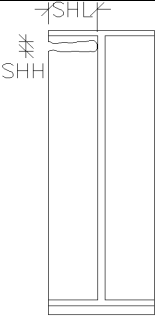
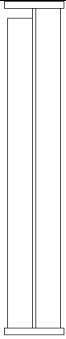


Figure 12.41: Dimensions of holes located at top part of stiffeners

Table 12.13: Dimensions of most common stiffener corrosion and hole scenarios

 <p>SC t</p> <p>S1</p>	
<p>SC (d_{stif})</p>	<p>0–20%</p>
<p>t loss (w_{stif})</p>	<p>10–90%</p>
 <p>SHH SHL</p> <p>HS1</p>	
<p>SHH (d_w)</p>	<p>0–12%</p>
<p>SHL (w_{stif})</p>	<p>0–100%</p>
 <p>SHH SHL</p> <p>HS1</p>	
<p>SHH (d_w)</p>	<p>0–3%</p>
<p>SHL (w_{stif})</p>	<p>0–100%</p>